

Weak ergodicity breaking and quantum scars in constrained quantum systems



Christopher J. Turner
School of Physics and Astronomy
University of Leeds

Submitted in accordance with the requirement for the degree of

Doctor of Philosophy

June 2019

The candidate confirms that the work submitted is his/her own, except where work which has formed part of jointly-authored publications has been included. The contribution of the candidate and the other authors to this work has been explicitly indicated below. The candidate confirms that appropriate credit has been given within the thesis where reference has been made to the work of others.

Chapter 3 includes work from the following publications:

Optimal free descriptions of many-body theories — C. J. Turner, K. Meichanetzidis, Z. Papić, J. K. Pachos Nature Communications 8, 14926 (2017) and *Free-fermion descriptions of parafermion chains and string-net models* — K. Meichanetzidis, C. J. Turner, A. Farjami, Z. Papić, J. K. Pachos Physical Review B 97, 125104 (2018).

In these papers: Basic idea to find information about interactions comes from Konstantinos Meichanetzidis. I came up with the main quantity to capture this, and worked out applications to Ising and parafermion models. Konstantinos Meichanetzidis and Ashk Farjami did applications to the 2D models. Zlatko Papić and Jiannis Pachos helped interpret results with ideas about criticality and quasiparticles.

Chapters 4 and 5 include work from the following publications:

Weak ergodicity breaking from quantum many-body scars — C. J. Turner, A. A. Michailidis, D. A. Abanin, M. Serbyn, Z. Papić Nature Physics 14, 745-749 (2018) and *Quantum scarred eigenstates in a Rydberg atom chain: entanglement, breakdown of thermalization, and stability to perturbations* — C. J. Turner, A. A. Michailidis, D. A. Abanin, M. Serbyn, Z. Papić Physical Review B 98, 155134 (2018).

In these papers: Alexios Michailidis and Maksym Serbyn did initial small scale numerics. I followed this up with large scale numerics. I

came up with the FSA method and all the different ways of evaluating it. Dmitry Abanin came up with the first solution to the zero energy degeneracy, which I then solved for other boundary conditions and symmetry constraints. Zlatko Papić and Dmitry Abanin found parallels with quantum scars in the single-particle quantum chaos literature.

Chapter 6 includes work from the following publication:

Emergent $SU(2)$ dynamics and perfect quantum many-body scars — S. Choi, C. J. Turner, H. Pichler, W. W. Ho, A. A. Michailidis, Z. Papić, M. Serbyn, M. D. Lukin, D. A. Abanin preprint (December 2018) arXiv:1812.05561 to appear in Physical Review Letters.

In this paper: I found the main results and did all the main calculations that made it into the paper. The same things were found independently by the US co-authors. The resulting paper merges the efforts of two groups (EU and US groups of authors) that independently worked out everything in this paper. Maksym Serbyn made the first argument for deriving the optimal point at range-4, in which I then fixed some issues and filled in important missing parts of the argument.

This copy has been supplied on the understanding that it is copyright material and that no quotation from the thesis may be published without proper acknowledgement

©2019 The University of Leeds and Christopher J. Turner

First, I would like to express my deepest gratitude to Zlatko Papić, my PhD supervisor, for his guidance and patience. And also for his way of taking often convoluted ideas and finding them much more manageable expression. I've also had the privilege of working closely with some great scientists: Alexios A. Michailidis, Maksym Serbyn, Dmitry A. Abanin, Konstantinos Meichanetzidis, Jiannis K. Pachos and Ashk Farjami. I extend my sincere thanks to all my collaborators for their insights and contributions. These have been instrumental in shaping what I set out here.

Equally significant, I've found are the distractions to my work. For these I must also add to my list Chris N. Self and Kristian Patrick. This includes a great many questions and discussions, on diverse topics from the gloriously open ended, chiefly from Kon, to those more focussed or even practical. From these I've learnt a great deal, and they continue to be a great source of enthusiasm.

Abstract

The success of statistical mechanics in describing complex quantum systems rests upon typicality properties such as ergodicity. Both integrable systems and the recently discovered many-body localisation show that these assumptions can be strongly violated in either finely tuned cases, or in the presence of quenched disorder. In this thesis, we uncover a qualitatively different form of ergodicity breaking, wherein a small number of atypical eigenstates are embedded throughout an otherwise thermalising spectrum. We call this a many-body quantum scar, in analogy to quantum scars in single-particle quantum chaos, where quantum scarred eigenfunctions concentrate around associated periodic classical trajectories.

We demonstrate that many-body quantum scars can be found in an unusual model recently realised in a 51 Rydberg atom quantum simulator. The observed coherent oscillations following in a certain quench experiment are a consequence of the quantum scar. At the same time, the level statistics rules out conventional explanations such as integrability and many-body localisation. We develop an approximate method to construct scarred eigenstates, in order to describe their structure and physical properties. Additionally, we find a local perturbation which makes these non-equilibrium properties much more pronounced, with near perfect quantum revivals. At the same time the other eigenstates remain thermal. Our results suggest that many-body quantum scars forms a new class of quantum dynamics with unusual properties, which are realisable in current experiments.

Abbreviations

k_B	Boltzmann's constant
\hbar	1 or perhaps $\rightarrow 0$
$O(\cdot)$	Big O; bounded above asymptotically, up to a constant factor
$\Theta(\cdot)$	Big Theta; bounded above and below asymptotically, up to constant factors
$\Omega(\cdot)$	Big Omega; bounded below asymptotically, up to a constant factor
QE	Quantum ergodic
QUE	Quantum unique ergodic
ETH	Eigenstate thermalisation hypothesis
RMT	Random matrix theory
GOE	Gaussian Orthogonal Ensemble
GUE	Gaussian Unitary Ensemble
MBL	Many-body localisation
MPS	Matrix product state
PXP	Effective model defined by Hamiltonian in Equation (4.3)
FSA	Forward-scattering approximation
S	Entropy
ρ	Density matrix
ξ_k	Entanglement energies
$D_{\mathcal{F}}$	Interaction distance
$ \mathbb{Z}_2\rangle$	\mathbb{Z}_2 Rydberg crystal state
\mathcal{P}	Constrained Hilbert space
\mathcal{K}	Forward-scattering subspace
\mathcal{C}	Spectral reflection operator, defined in Equation (4.7)
I	Spatial inversion symmetry operator
$g(t)$	Various names:— Loschmidt echo, return probability, fidelity
$\langle r \rangle$	Mean r -statistic, defined in Equation (4.16)

Contents

1	Introduction	1
2	Quantum ergodicity and thermalisation	5
2.1	Classical ergodicity	5
2.2	Quantum ergodicity and quantum scars	8
2.3	Eigenstate thermalisation hypothesis	10
2.4	Level statistics	14
2.5	Integrability and localisation: examples of strong ergodicity breaking	16
3	Entropy and entanglement in interacting quantum systems	19
3.1	Entanglement entropy	19
3.2	Entanglement spectrum	22
3.3	Detecting interactions through entanglement	24
3.4	Interaction distance in \mathbb{Z}_N -parafermion chains	27
3.5	Conclusions	29
4	Phenomenology of weak ergodicity breaking in a constrained quantum system	31
4.1	Cold-atom quantum simulators	32
4.2	Effective model, Hilbert space and symmetries	35
4.3	Quantum revival	38
4.4	Signatures of quantum chaos	42
4.5	Effect of perturbations	50
4.5.1	Physical perturbations	50
4.5.2	Integrable deformations	55

CONTENTS

4.6	Conclusions	57
5	Forward-scattering approximation and quantum scars	59
5.1	Forward-scattering approximation	60
5.2	Error analysis	67
5.3	Linear recurrence system	69
5.3.1	Loop counting for open chains	70
5.3.2	Loop counting on periodic chains	74
5.4	Asymptotics and zig-zag surfaces	76
5.4.1	Differential solution for the case of $p=1$	78
5.4.2	Numerical solution and analytic bounds in general	79
5.5	Conclusions	83
6	Enhanced quantum revival and emergent SU(2) dynamics	85
6.1	Deformation to suppress level repulsion	86
6.2	Deformation to stabilise revivals	87
6.3	Algebraic argument for revival stabilisation	88
6.4	Long-range deformation	93
6.5	Parameter optimisation	97
6.6	Toy model and eigenstate embedding	101
6.7	Conclusions	103
7	Conclusions	105
	Bibliography	111

List of Figures

2.1	Chaotic and regular trajectories of the Bunimovich stadium.	6
2.2	Atypical states in the quantum stadium billiard.	10
3.1	Illustration of spatial bipartition into subsystems.	20
3.2	Entropy growth in a many-body localised phase is logarithmic in term following a quench to a product state (14, 186).	22
3.3	Interaction distance for parafermion chains.	29
4.1	Experimental platform consisting of individual cold atoms trapped and arranged by optical tweezers.	33
4.2	Preparation method of various Rydberg crystal states (51, 129).	34
4.3	Domain wall density features coherent oscillations following a quench.	35
4.4	Oscillatory dynamics of the effective model Equation (4.3) following a quench to a Néel state.	39
4.5	Scatter plot of energy and overlap with the Néel state for eigenstates.	42
4.6	Absence of level repulsion in the PXP model.	44
4.7	Participation ratios for eigenstates over the product state basis decays exponentially with system size.	45
4.8	Diagonal matrix elements of Z in the energy eigenbasis.	45
4.9	Envelope function controlling the off-diagonal matrix elements of the Z observable.	47
4.10	Entanglement entropy for the PXP model.	48
4.11	Effect of the perturbations on dynamical properties of the PXP model.	53

LIST OF FIGURES

4.12	Local Z observable off-diagonal matrix elements under the influence of perturbations.	55
5.1	Illustration of a Lucas cube graph.	61
5.2	Comparison between the forward-scattering approximation and the numerically exact eigenvalue decomposition.	65
5.3	Time series of quantum revival probability to the Néel state and probability to be found within the forward-scattering subspace for system size $N = 32$. The latter is measured by the expectation value of the projector into the subspace \mathcal{K}	66
5.4	Error quantities in the forward-scattering analysis.	67
5.5	Computation time T in seconds for calculating the full set of β coefficients as a function of system size N	75
5.6	Numerical solution for the dominant eigenvalue λ of the transfer operator, Equation (5.63).	82
6.1	Minimum in the r -statistic	87
6.2	Enhanced oscillatory dynamics of the PXP model with range-4 perturbation.	88
6.3	Eigenstate properties of the PXP model with range-4 perturbation.	92
6.4	Coupling constants h_d in Equation (6.18) when chosen to maximise the fidelity at first revival.	94
6.5	Enhanced oscillatory dynamics of the PXP model with long-ranged perturbation.	95
6.6	Level statistics in the PXP model with long-ranged perturbation.	96
6.7	Algebraic structure in forward-scattering subspace.	97
6.8	Cross-comparison of the different cost functions.	100

Chapter 1

Introduction

A great deal of effort in both academia and industry is focussed on the development of quantum computing and other quantum technologies, in order to realise its promise of a step-change in our computational capabilities. There are computational tasks that, as far as we are aware, are hard for any classical computer but for which we know algorithms which can solve them easily on a quantum computer (43). The most famous example is the integer factorisation problem (155), which has far reaching consequences for cryptography. The current generation of quantum devices have been termed *noisy intermediate scale quantum* (NISQ) devices (130). The noise in their quantum gates and other imperfections will limit their capabilities to low-depth circuits. Fault-tolerant quantum computing using quantum error correction (64, 123) would require both lower noise and more physical qubits to perform a computational task beyond those achievable by classical means.

The problem of simulating many-body quantum problems is hard for classical computers. As the number of particles in a many-particle quantum system grows the memory required to describe a state of the system increases exponentially. However, for a quantum device this is a particularly natural problem (101). In highly controllable quantum systems a target Hamiltonian could be programmed through control parameters to the system, thereby emulating it within the quantum simulator. With near-term quantum devices we may be able to simulate quantum systems beyond the reach of classical computers. By unveiling hitherto unexpected phenomena, quantum simulation will challenge our current under-

1. INTRODUCTION

standing of quantum dynamics. We are already seeing progress in the creation of highly controllable quantum systems based upon a number of different technologies, such as: cold-atoms (19, 82, 175), superconducting qubits (137, 157) and optical systems (107). These are being used to simulate model quantum systems such as Ising spin models (81, 107, 113, 137, 185) and the fermionic Hubbard model (106). Similar designs have been used to experimentally realise many-body localised physics (25, 34, 146). In this section we will review Ref. (19), which reports a quantum dynamics experiment in a programmable cold-atom lattice featuring 51 qubits. The work of this thesis grew out of the effort to explain the curious findings of this experiment.

In this thesis, we argue that this phenomena is a novel form of ergodicity breaking, which we term a quantum many-body scar. This is in analogy to the earlier notion of a quantum scar in single-particle quantum chaos (71). The picture of a quantum many-body scar is one of a small number of non-ergodic or scarred eigenstates, which coexist with an otherwise thermalising spectrum. These special eigenstates can even be found at energy densities where the density of states diverges. The quantum scar is a weak form of ergodicity breaking, where only a minority of the eigenstates are affected. This stands in contrast to the well established notions of integrability (164) and many-body localisation (2) which break ergodicity and disrupt thermalisation across the entire spectrum.

In Chapter 2, we will review ergodicity and thermalisation in both classical and quantum systems. We will first discuss the distinction between quantum ergodicity (QE) and quantum unique ergodicity (QUE) (71) in single-particle systems. A system is QE but non-QUE when it has a small number of exceptional eigenstates. These exceptional eigenstates are referred to as a *quantum scar*. We will then review the eigenstate thermalisation hypothesis (ETH), which provides our current best understanding of how quantum systems thermalise (41).

In Chapter 3, we will introduce entropy and entanglement and its role in the thermalisation in quantum systems. Then, we will identify information in the entanglement spectrum that distinguishes interacting systems from non-interacting systems. This is based on our work in Ref. (109, 166). As non-interacting systems are non-chaotic, this provides another witness to quantum chaos in the entanglement.

Starting in Chapter 4, we will focus on the behaviour of the Rydberg atom chain in the limit of strong van der Waals forces, which has been the subject of recent experiment (19). This system shows strong non-equilibrium properties in the dynamics of local observables, entanglement entropy and many-body fidelity. Surprisingly, the level statistics indicates that this system is non-integrable. We will then relate the dynamical behaviour observed to the presence of a number of scarred eigenstates embedded among many typical eigenstates throughout the spectrum, as we proposed in Ref. (167). These findings will show this model to be a very interesting system in which to explore quantum dynamics.

In Chapter 5, we will seek to explain the phenomenology of the Rydberg atom chain using a technique we call a forward-scattering approximation, which we introduced in Ref. (167, 168). Within this approximation we efficiently find approximations to scarred subspace, producing explanations for the other anomalous properties of these special states.

In Chapter 6, based on our work in Ref. (35), we will show the non-ergodic subspace can be enhanced by addition of exponentially local additional terms, while the remainder of the eigenstates remains thermal. With this carefully chosen deformation, the forward-scattering subspace becomes almost exactly closed under the dynamics. At the end we discuss some recent results on other anomalously non-thermal quantum systems that we think are related.

1. INTRODUCTION

Chapter 2

Quantum ergodicity and thermalisation

In this chapter, we will review ergodicity and thermalisation in quantum systems. We will first discuss the distinction between ergodicity and unique ergodicity (71) in classical and single-particle quantum systems. A quantum system is QE but non-QUE when it has a small number of exceptional eigenstates. These exceptional eigenstates are referred to as a *quantum scar*. This allows for some initial conditions to rapidly equilibrate, whilst others show persistent non-equilibrium properties. We will then review the leading theory of thermalisation in quantum systems, the eigenstate thermalisation hypothesis (ETH), which builds upon ideas from random matrix theory (RMT) (41). Finally, we will discuss strong forms of ergodicity breaking: integrable systems and many-body localisation. Unlike with the quantum scar these strongly affect all the eigenstates and break quantum ergodicity.

2.1 Classical ergodicity

Before moving on to quantum ergodicity, we will first discuss the classical notion of ergodicity. In classical physics, the ergodic hypothesis is a property or assumed property of a system where the proportion of time a system spends in a region of its phase space is proportional to the volume or measure of that region.

2. QUANTUM ERGODICITY AND THERMALISATION

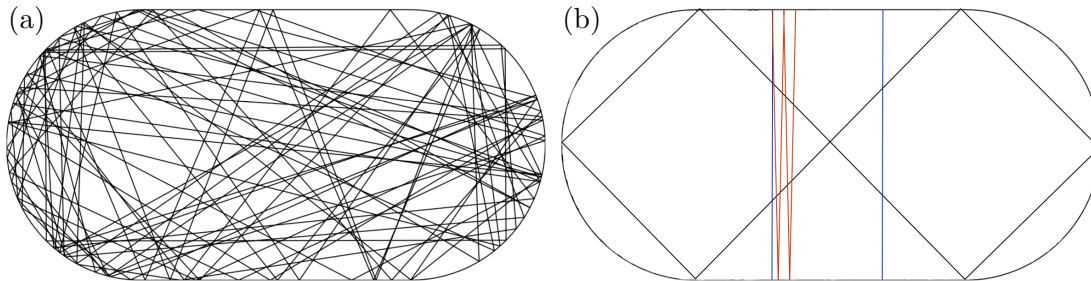


Figure 2.1: Chaotic and regular trajectories of the Bunimovich stadium. (a) Typical chaotic trajectories which diverge exponentially. (b) Regular trajectories of the stadium. Bouncing ball trajectories shown in blue, which diverge linearly when perturbed, shown in red. Also illustrated in black is a more intricate periodic orbit, which is exponentially unstable to perturbation. This is adapted from a diagram in Ref. (71).

This property underlies the use of statistical ensembles, such as the canonical ensemble, to describe the behaviour of classical systems. Ergodic theory is the study of dynamical systems seeking ergodic theorems and other results on mixing or thermalisation. In this section we will describe ergodicity in more detail and review a more refined notion of *unique* ergodicity.

As is customary, we will use billiard systems as examples to illustrate these ideas. Take a plane domain X , namely compact subset of \mathbb{R}^2 with a C^1 boundary. A billiard system is the dynamical system of a billiard, point-like single particle, propagating freely in a straight line across the interior of Ω and bouncing according to the familiar law of reflection upon hitting the boundary, here making use of the C^1 smoothness. Because of energy conservation, the phase space Ω can be taken as $X \times S^1$, away from the boundary, where the second factor describes the direction of the billiard's motion. A simple example is the interior of a circular disc. This system has rotation symmetry and hence angular momentum as a Noether charge. This example, far from being ergodic, is actually completely integrable, see Section 2.5. More elaborate examples include the Bunimovich stadium (28), Sinai billiard (156) and Barnett stadium (15). The Bunimovich stadium, see Figure 2.1, is the example best studied in physics, and is the one we will focus on.

We will now define ergodicity more formally. Let ϕ^t be the evolution map

for some time t . This map is measure preserving and is said to be ergodic if it satisfies any of a number of equivalent conditions (128):—

- For almost every orbit, the ergodic hypothesis holds, that is long-time averages converge to the phase-space or ensemble average, with a unique measure. For billiards, this is always the standard measure induced from the metric. This is like defining a point process from iterates of the evolution map and being able to estimate the relative volume of any measurable subset $A \subset \Omega$, just as one might do with Monte-Carlo integration using a random point process.
- There are no additional integrals of motion. All ϕ -invariant functions from Ω differ from constant functions only on measure zero sets. Equivalently, the phase space Ω is ϕ -irreducible, i.e. cannot be decomposed as the disjoint union of finite measure ϕ -invariant subdomains. If we have a non-constant ϕ -invariant function f , then the preimages of the different values in the range of f are ϕ -invariant subdomains.

The stadium billiard was proven by Bunimovich to be ergodic (28). A typical trajectory for this stadium is illustrated in Figure 2.1 (a). Two initially nearby trajectories will almost always diverge exponentially, indicating the presence of chaos. This stadium also features the so-called bouncing ball trajectories, see Figure 2.1 (b), that travel vertically up and down between the parallel straight edges in the rectangular subdomain. These trajectories are measure zero in phase space, however nearby trajectories to these bouncing balls with a perturbed angle initially diverge only linearly until exiting the rectangular subdomain. Beside these, there are also more complicated periodic trajectories which leave the rectangular subdomain. One is shown in Figure 2.1 (b). These trajectories are unstable, with nearby trajectories diverging exponentially. These non-ergodic trajectories are however measure zero and there is no contradiction with the Bunimovich stadium being ergodic. Similarly, the Barnett stadium is ergodic (156). It is also strongly chaotic with almost all trajectories diverging exponentially.

A dynamical system is *uniquely* ergodic if there is only one locally compact Borel measure on X invariant under ϕ^t . For ergodic billiard systems this unique measure is the standard measure induced from the metric. If the evolution has

2. QUANTUM ERGODICITY AND THERMALISATION

a periodic orbit then it is not uniquely ergodic. For this reason, both Barnett stadium and Bunimovich stadium are not uniquely ergodic, despite both being ergodic, since they both feature periodic orbits.

2.2 Quantum ergodicity and quantum scars

It's not always obvious how to translate concepts from classical physics to quantum physics. The key hallmark of classical chaos, locally diverging trajectories, has no analogue in quantum systems – distances between quantum states are invariant under unitary time evolution. In our discussion of quantum analogues to ergodicity and unique ergodicity, see review Ref.(71), we will focus once again on billiard systems as a source of examples. Quantum billiard systems are a quantisation of the classical billiard systems. Their evolution is governed by the Schrödinger equation, with the Laplacian on X for the Hamiltonian, and Dirichlet boundary conditions are imposed on the wavefunction at the boundary ∂X . Due to the uncertainty principle, it is much simpler to consider probability measures on X given by quantum wave functions rather than working over the full phase-space with the conjugate momentum degrees of freedom included. The weaker property of real-space ergodicity is enough to illustrate the concepts. Handling the full phase-space is much more technical, see for example Ref. (187).

First we will define quantum unique ergodicity. Let ψ_1, ψ_2, \dots be the sequence of eigenfunctions ordered by increasing energy. If the sequence of the associated real-space probability measures $\nu_j = |\psi_j|^2$ converges in the weak-* sense to the uniform measure ν , then the system is said to be quantum unique ergodic. This occurs if for all continuous functions f ,

$$\lim_{j \rightarrow \infty} \int d\nu_j f = \int d\nu f. \quad (2.1)$$

This is the appropriate notion of convergence as high energy wavefunctions typically vary rapidly, but this limit can remain smooth. The weaker property of quantum ergodicity requires only there to exist a subsequence that contains almost all of the eigenfunctions which converges. It's worth pointing out that Berry's conjecture (20) for the form of high-energy eigenfunctions as being a

2.2 Quantum ergodicity and quantum scars

Gaussian random field, made from the random superposition of a great number of waves, is suggestive of quantum ergodicity.

A major result of the work on quantum ergodicity is the so-called quantum ergodicity theorem. This states that classic ergodicity implies quantum ergodicity, for the cases of billiard systems and single-particle quantum mechanics on compact Riemannian manifolds (59, 184). This followed earlier work on the case without boundary (42, 154, 182). A definition is of little importance without examples that realise it. Are there any systems which are quantum ergodic but not quantum unique ergodic? We expect non-unique ergodicity to be more delicate in quantum mechanics than in dynamical systems, because quantum particles are smeared out in quantum mechanics by the uncertainty principle. In particular the quantum wavefunction cannot be localised onto a classical periodic orbit because these are measure zero. They might depend also on properties of the neighbourhood around the periodic orbits. For this reason, it is conjectured that any hyperbolic manifold, which are all strongly chaotic and include the Barnett stadium, are quantum unique ergodic, despite in some cases featuring periodic orbits (138).

In the Bunimovich stadium, sequences of special eigenstates were found (73) which anomalously concentrate around the periodic orbits of the classical system. This has been seen to occur numerically for both the bouncing ball trajectories and the more elaborate unstable periodic trajectories. For these, the name *quantum scar* was coined. The classical periodic orbit is said to have left an imprint or scar upon the eigenfunctions. Many years later, the existence of the bouncing ball mode sequences was rigorously proven, showing the system to be non-QUE (70). More generally, we could say that a quantum scar is merely a sequence of eigenstates which form a counterexample to quantum unique ergodicity (167), without a reference classical system to hand. In Chapter 4, we will numerically identify atypical eigenstates in a quantum many-body system, suggesting that this system is ergodic but not uniquely ergodic.

The existence of these scarred eigenfunctions was eventually rigorously established, building upon a older heuristic argument by O'Connor and Heller (119, 183). First, a collection of bouncing-ball quasimodes were established, these are approximate eigenstates are highly concentrated around the bouncing ball trajec-

2. QUANTUM ERGODICITY AND THERMALISATION

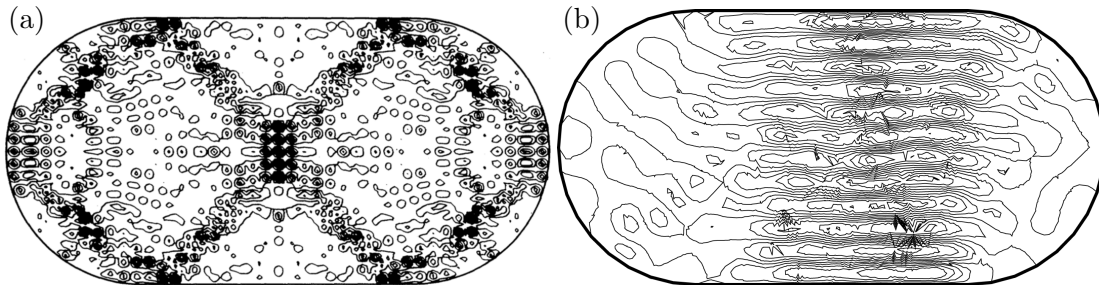


Figure 2.2: Atypical states in the quantum stadium billiard. (a) Eigenfunction scarred by an unstable periodic orbit. Reproduced from Ref. (73). (b) Eigenfunction with a strong bouncing ball character. Credit to Maksym Serbyn.

tories. These take the form $\chi(x) \sin(ny)$ where $y \in [0, \pi]$ is the vertical coordinate for suitable $\chi(x)$. These quasimodes have energies concentrated around $2n^2$, with an energy variance at most K^2 . If there are at most M eigenfunctions, uniformly in n , in an interval around $2n^2$ with width $4K$, then within the interval there is an eigenfunction with overlap at least $\sqrt{3/4M}$ with the quasimode (183). This is the scarred eigenfunction.

The remaining difficulty was to show that the eigenstates did not concentrate in these intervals such that the M could not be chosen uniformly in n . In fact, the expected behaviour in two-dimensions is for this propositions to hold, because the density of states is expected to be largely energy independent, making the conjecture highly plausible. The required absence of eigenvalue accumulation was eventually shown in Ref. (70), for almost all widths of the rectangular region. This was even generalising to any partially rectangular domain, which are planar domains with a flat rectangle region like the Bunimovich stadium, giving the effect a remarkable robustness. This story will motivate the construction of quasimodes for the scarred eigenstates of a quantum many-body system in Chapter 5. Of course, the exponential many-body density of states will foil a naïve attempt to use the same argument to establish the existence of these scarred eigenstates.

2.3 Eigenstate thermalisation hypothesis

If we take a system highly out of equilibrium, such as a container of gas where all the particles happen to be located in one half of the container, we expect it to

2.3 Eigenstate thermalisation hypothesis

reach thermal equilibrium rapidly. We might try an ergodic hypothesis to justify the use of statistical mechanics in describing such a situation. The ergodic hypothesis, however, concerns long-time averages of observables and is in principle unrelated to the typicality of observations in a short time window as in this thought experiment. A stronger mixing property is required to make sense of the dynamics of thermalisation. Thermalisation is a process of reaching typical configurations after starting from an initial atypical configuration. This is often much faster than exploring the full phase-space as in ergodicity. The typical configurations in this example have the particles close to equally divided between the two halves of the container. There are exponentially more configurations like these compared to those that look like the initial state. For large number of degrees of freedom, the system will spend almost all of its time in typical configurations that look like the thermal equilibrium and small fluctuations about it. Thermalisation is a stronger mixing property than ergodicity. It requires that instantaneous observables expectation values approach their equilibrium values and then remain close for most times. At late time sojourns occur due to the Poincaré recurrence theorem (23), occurring at time exponentially long in the number of degrees of freedom. This can be related to fluctuation theorems (40, 83), and how violations of second law can occur with a probability exponentially small in the number of degrees of freedom (38). Thermalisation is usually much faster than the time it would take to explore all of phase space, although thermalisation can be extremely slow e.g. in glassy systems (135).

We will now discuss thermalisation specifically in quantum dynamics for states in a microcanonical distribution energy window. An initial state from this window can be expanded as

$$|\psi(t)\rangle = \sum_{\alpha} c_{\alpha} |\alpha\rangle, \quad (2.2)$$

in terms of the energy eigenstates $|\alpha\rangle$ with energy E_{α} within the window, and c_{α} are complex numbers specifying the initial state. The time evolution for the expectation value of an operator A from this initial state is,

$$A_{\psi}(t) = \sum_{\alpha} |c_{\alpha}|^2 A_{\alpha} + \sum_{\alpha \neq \beta} c_{\alpha}^* c_{\beta} e^{i(E_{\alpha} - E_{\beta})t} A_{\alpha\beta}, \quad (2.3)$$

2. QUANTUM ERGODICITY AND THERMALISATION

where the observable matrix elements $A_{\alpha\beta} = \langle \alpha | A | \beta \rangle$. The long-time average of $A(t)$ is found to be the diagonal matrix elements of A weighted by the initial state coefficients, since the second term average to zero in the absence of finely tuned energies or initial states. To satisfy the ergodic hypothesis, we want to get the same result independent of the chosen initial state, so these diagonal matrix elements need to be constant. The many-body level spacing is exponentially small in the number of degrees of freedom, thus it may take an exponential time to ensure that the off-diagonal contribution averages to zero. To obtain a much more rapid thermalisation we could suppose that the off-diagonal matrix elements are suitably small. Sufficient conditions can be found in von Neumann's ergodicity theorem (173), and in more recent extensions (62, 63, 134).

Many ideas in quantum chaos were inspired by the theory of complex atomic spectra developed by Wigner (176) and Dyson (45). Rather than trying to directly solve the complicated interacting problem, they supposed that the properties of interest did not depend in any detailed way on the Hamiltonian, thus they could well replace it with a random matrix. This work lead to the field of random matrix theory (RMT) (108) where the properties of typical random matrices drawn from a variety of ensembles are studied. Statistical properties of eigenvalues and eigenvectors can exhibit concentration of measure and inform us of the properties of matrices that are supposed to be typical, such as chaotic Hamiltonians. For Hamiltonians that can be modelled as real symmetric matrices, the appropriate random matrix ensemble is the Gaussian orthogonal ensemble (GOE) which is invariant under orthogonal transformations.

To see what this random matrix theory hypothesis means for thermalisation, we can calculate observable matrix elements. Let D be the microcanonical window dimension, and assume that the Hamiltonian is typical of the GOE matrix ensemble. For large D , from the unitary invariance of the matrix ensemble each component of each eigenstate can be treated as an independent Gaussian random variable. Hence the matrix of overlaps with the eigenvectors of an observable A has uncorrelated Gaussian variates for elements. To leading order in $1/D$, the observable matrix elements averaged over the matrix ensemble can be calculated using Gaussian integrals. This average will be denoted with an overline. The average diagonal element $A_{\alpha\alpha}$ is a constant \overline{A} , independent of α . The off-

2.3 Eigenstate thermalisation hypothesis

diagonal elements vanish on average, because it is odd in the random variables. The fluctuations in the diagonal matrix elements are,

$$\overline{A_{\alpha\alpha}^2} - \overline{A_{\alpha\alpha}}^2 = \frac{2}{D^2} \sum_{\mu} A_{\mu}^2 = \frac{2}{D} \overline{A^2} \quad (2.4)$$

and the fluctuations in the off-diagonal matrix elements are

$$\overline{|A_{\alpha\beta}|^2} - \overline{A_{\alpha\beta}}^2 = \frac{1}{D^2} \sum_{\mu} A_{\mu}^2 = \frac{1}{D} \overline{A^2}, \quad (2.5)$$

where A_{μ} are the eigenvalues of A restricted to the microcanonical window and all to leading order in $1/D$. Altogether, the random matrix theory predictions may be summarised as

$$A_{\alpha\beta} \approx \overline{A} \delta_{\alpha\beta} + \left(\frac{\overline{A^2}}{D} \right)^{\frac{1}{2}} R_{\alpha\beta} \quad (2.6)$$

where R is a matrix of standard Gaussian random variates that satisfies an appropriate symmetry property, i.e. real symmetric or Hermitian. This satisfies the conditions of von Neumann's theorem and leads to rapid thermalisation.

In order to describe real systems there are a number of deficiencies of the random matrix hypothesis that need to be remedied: the microcanonical average \overline{A} can depend upon the energy density (44) and correlation functions can violate RMT predictions (85, 160). A generalisation of the RMT hypothesis was provided by Srednicki (158, 159, 160), that adds additional structure to the observable matrix elements sufficient to describe the thermalisation of realistic systems. This Ansatz is known as the eigenstate thermalisation hypothesis (ETH) (41). This is a statement about the energy basis matrix elements of physical observables,

$$A_{\alpha\beta} \approx \overline{A}(E) \delta_{\alpha\beta} + e^{-S(E)/2} f_A(E, \omega) R_{\alpha\beta}, \quad (2.7)$$

where $E = (E_{\alpha} + E_{\beta})/2$ is the mean energy and $\omega = E_{\alpha} - E_{\beta}$ is the transition energy. The first term describes the behaviour of the microcanonical ensemble $A(E)$ as a smooth function of energy. The second term describes the deviations

2. QUANTUM ERGODICITY AND THERMALISATION

and fluctuations about the microcanonical prediction. The overall scale of this term is controlled by an exponential in $S(E)$, the thermodynamic entropy, equivalently the fluctuations decay as the square root of the density of states, c.f. the D dependence in Equation (2.6). The hypothesis is clearly then a statement about excited eigenstates where the density of states diverges in the thermodynamic limit as opposed to the low energy physics of ground states. Finally there is an envelope function $f_A(E, \omega)$ which is smooth in both parameters. This function describes the quantum fluctuations in the microcanonical ensemble, behaviour of non-equal time correlation functions and linear response to perturbation (85).

The ETH predictions have been observed numerically in many systems, first with hard-core bosons and fermions in 1D (131, 132). Predictions are known to fail for integrable systems, where the integrals of motion impede thermalisation, and in the presence of many-body localisation — see Section 2.5. A comment is in order about the caveat around physical observables. Necessarily, only some Hermitian operators will satisfy ETH and others will not, such as projectors onto individual eigenstates. It is generally believed, however, that few body observables, even those with support of up to half of the total system (56), are appropriate operators for the ETH ansatz.

Another phenomena found in chaotic systems is that $f(E, \omega)$ at small ω should saturate to a value constant with respect to ω , a feature known as a Thouless plateau (93). The extent of the plateau sets an energy scale referred to as the Thouless energy, below this energy scale the system can essentially be modelled by standard ensembles from random matrix theory (46). This sets a longest time scale after which we expect observables to cease evolution. This typically diverges polynomially in number of degrees of freedom, much slower than the exponential increase in the density of states. Consequently, although the RMT hypothesis has validity only for a narrow range of energy widths ω , in the RMT energy windows there is an exponential number of states consistent with the use of RMT.

2.4 Level statistics

A commonly used diagnostic of quantum chaos is the level statistics (21, 125) which looks as the distribution of energy level gaps in a system. In an ergodic and non-integrable phase we expect energy levels to exhibit spectral repulsion.

This can be understood from perturbation theory as any unusually small energy gap would be unstable to a perturbation like the appearance of an avoided crossing. There is no level repulsion between distinct symmetry sectors, as the perturbation theory analogy suggests because no symmetric perturbation can create off-diagonal matrix elements between them. For this reason the level statistics must always be considered in an irreducible symmetry sector.

The basic idea can be illustrated with a 2x2 matrix (176),

$$H = \begin{pmatrix} +\frac{\Delta}{2} & \frac{V}{2} \\ \frac{V^*}{2} & -\frac{\Delta}{2} \end{pmatrix}, \quad (2.8)$$

where Δ and V are (real) Gaussian random variates around zero with variance σ^2 . This is a GOE random matrix with the irrelevant identity component removed, i.e. the matrix is shifted so that its spectrum is centred about zero. The distribution of energy level spacings has for a probability density functions

$$P(\omega) = \frac{1}{2\pi\sigma^2} \int d\Delta dV \delta\left(\sqrt{\Delta^2 + V^2} - \omega\right) \exp\left(-\frac{\Delta^2 + V^2}{2\sigma^2}\right), \quad (2.9)$$

which is an integral over a circle. This results in

$$P(\omega) = \frac{\omega}{\sigma^2} e^{-\frac{\omega^2}{2\sigma^2}}. \quad (2.10)$$

In systems without time-reversal symmetry the real and imaginary parts of V are independent variables, thus corresponding is an integral over a spherical surface. Together, these may be summarised as

$$P(\omega) = A_\beta \omega^\beta e^{-B_\beta \omega^2}, \quad (2.11)$$

where $\beta = 1$ in the GOE case and $\beta = 2$ in the GUE case. The constants A_β and B_β are fixed by normalisation and the mean level spacing. In this distribution we can see level repulsion, i.e. $P(\omega) \rightarrow 0$ as $\omega \rightarrow 0$. The adjacent level spacing distributions for large matrices does not have a closed form. They are, however, very well approximated by the result for 2x2 matrices (177) in what is known as the Wigner surmise.

2. QUANTUM ERGODICITY AND THERMALISATION

For many different systems with a chaotic classical limit, it has been found that the level spacings follow the Wigner surmise for narrow windows and at high energies (9, 24, 163). Based on this original observation, Bohigas, Giannoni and Schmit (BGS) conjectured that this is true for generic quantised chaos (24). In more generic non-integrable many-body quantum systems similar observations are made, for example in lattice systems (142, 143). In an integrable system (and also many-body localised systems (125)), however, see Section 2.5, eigenstates adjacent in energy will differ in an extensive number of local integrals of motion. This causes the matrix elements of local perturbations between them to be suppressed, leading to an absence of level repulsion. This is easily distinguishable from the Wigner surmise, and for this reason the level statistics is a useful diagnostic for the presence, or absence, of quantum chaos.

2.5 Integrability and localisation: examples of strong ergodicity breaking

Classical integrable systems (13) are systems of differential equations that can be exactly integrated. In the case Hamiltonian systems, as per the Liouville–Arnold theorem, there exists a canonical transformation to action-angle coordinates and consequently the phase space is foliated by invariant tori (12). The action variables are integrals of motion, and each configuration of action variables produces invariant surface which are toroidal, assuming they are compact. Some examples of integrable systems include harmonic potentials, the Korteweg–de Vries equation and the classical Heisenberg ferromagnet.

One case in quantum mechanics where exact solutions can be easily obtained are non-interacting systems. These are said to be one-body reducible. This means that for each solution of the corresponding single-particle problem there is an integral of motion which counts the number of particles which take that solution. All scattering matrices are trivial and follow from the symmetry properties of the particles concerned. Examples include electronic band theory, integer quantum Hall effect (97) and models for topological insulators and superconductors (69). The single-particle problem may be chaotic, but even in this case the chaotic

eigenfunctions still produce integrals of motion for the many-body system. These are much less complex to calculate compared to finding solutions of a generic many-body system.

A more demanding family of exactly solvable quantum models are the one-dimensional quantum integrable systems (164), these are typically related to exactly solvable two-dimensional statistical mechanical models (18). These models are solved through use of the Bethe Ansatz or quantum inverse scattering method. This has been successfully applied, for example, to the antiferromagnetic Heisenberg model and the Fermi-Hubbard model (77). Quantum integrable systems are said to be two-body reducible. This means that from a two-particle scattering matrix which satisfies the Yang-Baxter equation, all many-particle scattering matrices are generated.

A recently discovered non-equilibrium phase of matter is many-body localisation. This is found in some interacting models with strong quenched disorder (2). They are a generalisation of Anderson localisation (10) by the addition of interactions. They are characterised by an emergent set of localised integrals of motion (78, 151). In the fully localised phase, the highly excited eigenstates satisfy an entanglement area law (17, 151) and following a product state quench the entanglement follows a characteristic logarithmic growth (14, 186). More detail will be given in Chapter 3. Both results are in contrast to what is found in the Bethe Ansatz integrable model, hence localised models are a distinct class of models by themselves.

As mentioned previously, when a system has a complete set of local integrals of motion we do not expect level repulsion. Poisson level statistics are commonly observed in integrable systems. This occurs because the energy levels are effectively uncorrelated random variables. The analogue to the BGS conjecture for integrable systems is by Berry and Tabor (21), they propose that quantised integrable systems have Poisson level statistics. This also commonly occurs in integrable systems without classical counterparts, and the context of many-body localisation (125). However, there are examples where this fails. This typically occurs in cases of additional structure, such as for harmonic potentials (126), or large separation of energy scales (181).

The presence of integrals of motion in integrable and localised systems makes

2. QUANTUM ERGODICITY AND THERMALISATION

dynamics predictable. They foliate the phase space of classical systems preventing it from being fully explored, and decompose the Hilbert space of quantum systems so eigenstates nearby in energy can take very different expectation values. In the end, ergodicity and eigenstate thermalisation are violated in these systems. Quantum integrable systems thermalise to generalised Gibbs ensembles (172) rather than the standard ensembles of statistical physics. We could refer to integrability and many-body localisation collectively as forms of strong ergodicity breaking, analogous to violating the quantum ergodicity property from Section 2.2, as all their eigenstates are non-thermal. This is in contrast to the weak ergodicity breaking of a many-body quantum scar, which would be analogous to systems that are not quantum *unique* ergodic. In the remainder of this thesis, Chapters 4–6, we will study an example which bears the hallmarks of hosting a many-body quantum scar.

Chapter 3

Entropy and entanglement in interacting quantum systems

In this chapter, we will look at the ergodicity and thermalisation from the perspective of quantum entanglement. Quantum entanglement is often studied through the use of entanglement monotones, the prototypical example of which is the entanglement entropy (118). Given the central role of entropy in thermodynamics it is natural to look for measures of ergodicity and thermalisation in entropic quantities. First we will review the use of entanglement entropy, either regarding eigenstates or dynamically following a quench, for understanding the processes of thermalisation in quantum systems. Then we will review the entanglement spectrum introduced by Li and Haldane (99), which provides greater detail into the patterns of entanglement in quantum systems. Finally, we will identify information in the entanglement spectrum that distinguishes interacting systems from non-interacting systems. This is based on our work in Ref. (109, 166). As non-interacting systems are regular, or non-chaotic, when viewed as many-body systems this provides another witness to quantum chaos in the entanglement.

3.1 Entanglement entropy

Entropy is a key concept in statistical physics, and provides another witness to thermalisation and its breakdown. In classical systems entropy is used to char-

3. ENTROPY AND ENTANGLEMENT IN INTERACTING QUANTUM SYSTEMS

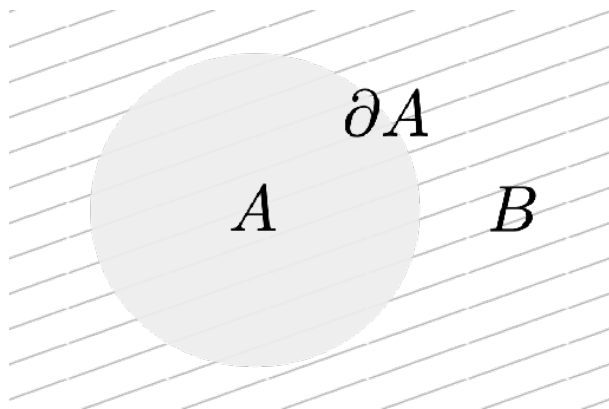


Figure 3.1: Illustration of spatial bipartition into subsystems. Tracing over the degrees of freedom in B leaves a density matrix ρ on the reduced system A . The von Neumann entropy of this density matrix is called the entanglement entropy. For gapped ground states this follows an area law $S = O(|\partial A|)$, where $|\partial A|$ is the size of the boundary between the subsystems. Thermal states and highly-excited eigenstates typically follow a volume law $S = \Theta(|A|)$.

acterise the delocalisation of a phase space distribution. For an isolated system, however, Liouville's theorem implies that phase space volumes are conserved, leaving simple entropy measures invariant. This issue is circumvented by integrating out some number of degrees of freedom effectively producing an open subsystem within the isolated one. Analogously the quantum evolution is unitary, rendering the purity and distinguishability of quantum states invariant. The same trick in the quantum case leads to the consideration of entanglement entropies. The Von Neumann entropy

$$S(\rho) = -\text{tr}(\rho \ln \rho) \tag{3.1}$$

of a mixed state ρ is the most often used quantum entropy in quantum information (118), and is a straightforward generalisation of the Gibbs or Shannon entropy from classical information theory. The von Neumann entanglement entropy for a state ψ and a subsystem A is the entropy of a reduced density matrix ρ , formed by the partial trace of ψ over B , the complementary subsystem to A , see Figure 3.1.

Thermalisation of all observables within a small subsystem \mathcal{A} , as expected in

the ETH scenario, implies the entanglement entropy is equal to the thermodynamic entropy of \mathcal{A} at a temperature T (56, 141). The thermodynamic entropy is an extensive quantity, scaling proportional to the volume of \mathcal{A} and is greatest in the middle of the spectrum where the many-body density of states is greatest. In finite-size lattice systems, the eigenstate entanglement entropies are expected to cluster strongly around the curve describing the relationship between mean energy and thermodynamic entropy and consequently follow a volume law $S = \Theta(L)$, assuming we are in one dimension and where L is the system size.

In integrable systems the entanglement entropy of highly excited state is typically volume law, but concentrates around the statistical mechanical prediction much more slowly and rare states with greatly reduced entanglement entropy can be found down to scaling that is logarithmic in system size (5, 144). In Anderson and MBL fully localised phases, in one-dimension, the eigenstate entanglement entropy is typically area law $S = O(1)$ throughout the spectrum (17, 151), reminiscent of gapped ground states (72). In the related notion of quantum critical glasses the eigenstate entropies are logarithmic $S = O(\log L)$ in system size (169), similar to the ground states of quantum critical points (29, 171). Logarithmic corrections to the area law also appear in Fermi liquids with Fermi surfaces at least dimension one (179). In summary, eigenstate entropy is a powerful way of identifying ergodic systems and different forms of ergodicity breaking but at the same time it is much more computationally demanding than diagnostics such as the level spacing distribution. For a many-body system featuring weak ergodicity breaking with rare non-thermal states we would expect these to appear as outliers in the eigenstate entanglement entropy (167).

A more direct way to view thermalisation through entanglement is in a quench experiment. An initial state with low entanglement is chosen and then the entanglement entropy is tracked over the course of the time evolution. In chaotic systems the initial growth of entanglement in such a quench experiment is linear in time (87), before eventual saturation (124). This, however, is not a reliable sign of chaotic dynamics. In integrable systems linear growth in entanglement is also observed, although with great variability in the slope depending on the initial state (6, 30). Surprisingly, even in systems considered chaotic there can be considerable variation in the slope of the initial entanglement growth (111).

3. ENTROPY AND ENTANGLEMENT IN INTERACTING QUANTUM SYSTEMS

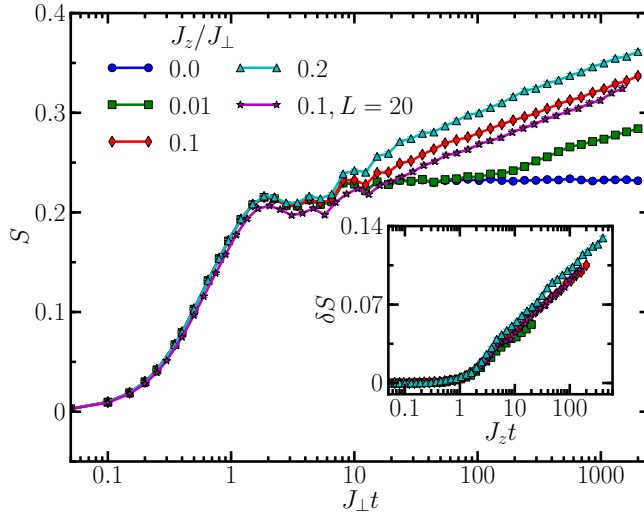


Figure 3.2: Entropy growth in a many-body localised phase is logarithmic in term following a quench to a product state (14, 186). The precise model here is the disordered field Heisenberg XXZ chain. Here, the ratio J_z/J_\perp sets the interaction strength. For $J_z = 0$, the system is an Anderson insulator and following local relaxation quickly saturates to a system size independent value. When $J_z \neq 0$, the system is many-body localised and following local relaxation there is an extended growth logarithmic in time. Reproduced from (14).

Indeed, integrable systems can show this same phenomenon despite forming the prototypical non-chaotic systems. The converse implicate works better; in Anderson localised systems where the entanglement growth saturates quickly to a non-extensive value and in many-body localised systems where the growth is logarithmic (14, 186). This was a key early result in many-body localisation which showed that many-body localised systems were genuinely different to Anderson localised ones, see Figure 3.2.

3.2 Entanglement spectrum

The entanglement spectrum is another way to characterise the bipartite entanglement in a quantum state, introduced by Li and Haldane (99). This is the collection of eigenvalues p_k of the reduced density matrix $\rho = \text{tr}_B |\psi\rangle \langle \psi|$. These are commonly viewed as entanglement energies $\xi_k = -\ln p_k$, so that the probabilities

3.2 Entanglement spectrum

$p_k = \exp(-\xi_k)$ are Boltzmann factors with a unit “entanglement temperature”. From this, we refer to the largest eigenvalues of ρ as being low-lying because they correspond to the smallest entanglement energies. The entanglement spectrum packages up the information of the von Neumann entanglement entropy together with all the Rényi entropies. For quantum Hall states, the entanglement energies exhibits a universal gapless structure, related to the real energy spectrum of a low-energy conformal field theory description of the boundary (99). Beyond these low-lying entanglement energies there may be additional levels describing non-universal properties further interior into the system, separated from the universal portion by an entanglement gap.

Motivated by this bulk boundary correspondence (52) the entanglement spectrum quickly became a popular tool in the study of topological insulators and superconductors (69). The entanglement spectrum is also central to the classification of interacting symmetry-protected topological phases in one dimension (53, 165). In gapped integrable systems (7) it decays faster than a power-law, and it was found to take a particular universal form around quantum critical points (31). Much less is known about the entanglement spectrum of highly-excited eigenstates. The reduced density matrices of highly-excited states of chaotic systems are similar to Wishart random matrices, and their spectrum follows the Marchenko-Pastur distribution (103, 180). In contrast, for many-body localised systems the entanglement spectrum decays as a power law (150).

We now give an intuitive argument why low-energy entanglement levels should be thought of as being close to the cut and high-energy as being far away, a detail that appears related to a bulk-boundary correspondence. This argument is strongly related to one made in Ref. (165). We will assume that we are looking at a weakly entangled state with area law entanglement entropy. We can take a Schmidt decomposition or singular value decomposition of a state between the two subsystems separated by the cut. Using the unitary isometries provided by the decomposition, we can take an operator acting on the entanglement Hilbert space, where the singular values or entanglement spectrum lives, and represent it as an operator on either of the two subsystems. Equally, chopping off one of the isometries produces a purification of the reduced density matrix, which is a joint pure state between the reduced system and the entanglement Hilbert space. If

3. ENTROPY AND ENTANGLEMENT IN INTERACTING QUANTUM SYSTEMS

we consider a connected correlation function between an operator acting on the entanglement Hilbert space and one that is separated from the entanglement cut by a distance l , this can be represented as a correlation function of the full system by representing the entanglement operator on the other subsystem. Hence, this vanishes up to corrections $O(e^{-l/\xi})$, where ξ is the correlation length. This suggests that a perturbation to our system at a distance l from the cut would disturb the entanglement Hilbert space only to $O(e^{-l/\xi})$. A small influence on the entanglement spectrum may however significantly alter highly-excited entanglement energies. The eigenvalues of ρ that are referred to as being high-energy are actually nearly degenerate, and thus can be strongly disturbed by some change far from the boundary. From this argument, it is reasonable to suggest that as we look at increasingly excited entanglement energies we are in turn looking further into the bulk of the subsystem.

3.3 Detecting interactions through entanglement

We have briefly explained how the entanglement spectrum can be used to identify topological phases and edge theories of quantum Hall states. What information about quantum chaos is contained within the entanglement spectrum? If the ground state reproduces information about the excitation spectrum through the bulk-boundary correspondence, then the ground state entanglement spectrum might inform us of the relaxation of low-lying excitations. We will look for signatures of interactions in the spectrum, as interactions are necessary for many-body quantum chaos by comparing them against non-interacting, or free, fermion systems.

For this purpose, we introduce the interaction distance (166) for a mixed quantum state, or density matrix, ρ ,

$$D_{\mathcal{F}}(\rho) = \min_{\sigma \in \mathcal{F}} D(\rho, \sigma) \quad (3.2)$$

where

$$D(\rho, \sigma) = \frac{1}{2} \text{tr} \sqrt{(\rho - \sigma)^2} \quad (3.3)$$

is the trace distance (118) between ρ and σ . The states σ are chosen out of \mathcal{F} ,

3.3 Detecting interactions through entanglement

the manifold of all free fermion states. This contains Gaussian states for any set of fermionic quasiparticles rather than depending on an imposed canonical choice, unlike in some previous works (57, 58, 60, 104). This makes $D_{\mathcal{F}}$ suitable for systems which might be free in terms of emergent quasiparticles. $D_{\mathcal{F}}$ has a geometric interpretation as the distance from ρ to \mathcal{F} . As the trace distance is bounded between 0 and 1, so is the interaction distance. Furthermore, the trace distance has a physical interpretation as measuring the maximum distinguishability of ρ and σ when measuring a single observable (55, 118); this is inherited by the interaction distance.

This definition is not immediately helpful for calculations, featuring a minimisation over a large class of operators, and requires simplification. For any $\sigma \in \mathcal{F}$, the algebra of fermion operators in which σ is a Gaussian state respects the canonical anticommutation relations. These relations are invariant under unitary conjugation, hence \mathcal{F} can be partitioned into unitary orbits or equivalence classes each identified only by the eigenvalue spectrum. The optimisation problem may be broken into two steps. First, fix a spectrum for σ and find the minimum element within that equivalence class to take as the representative of the orbit. This occurs when σ and ρ are simultaneously diagonal, and the eigenvalues are matched in rank order (75, 105). Then, $D_{\mathcal{F}}$ is obtained by minimising over the representative minimum elements from each orbit by taking variations in the eigenvalue spectrum only (166). In general, the unitarily transformed modes form non-linear combinations of the original modes and so there is no canonical transformation between them.

So far, we have not specified where the mixed state ρ has come from. We will concern ourselves with states which are reduced density matrices of quantum ground states after taking a spatial bipartition. In this case the eigenvalue spectra of ρ and σ are entanglement spectra for correlations between the two parts of the system. The partial trace serves as a quantum channel through which we view the ground state. A channel is said to be Gaussian if it maps any Gaussian state, in a fixed set of canonical operators, to another Gaussian state in those same operators (174). If a partial trace is taken over a set of fermion modes from the set of canonical operators, or over a subset of the modes following a canonical transformation, then it is a Gaussian channel (127). We can say that

3. ENTROPY AND ENTANGLEMENT IN INTERACTING QUANTUM SYSTEMS

the interaction distance measures the tension between picking a set of operators such that the ground state is a Gaussian state and such that the partial trace is a Gaussian channel.

Given that σ is a Gaussian state, over a set of M fermion operators, its eigenvalues σ_k are highly constrained. The corresponding entanglement energies must satisfy,

$$-\ln \sigma_k(\epsilon) = \epsilon_0 + \sum_{i=1}^M n_i(k) \epsilon_i \quad (3.4)$$

where each $n(k) = (n_1(k), n_2(k), \dots, n_M(k))$ is an assignment of occupation numbers patterns to each level in the spectrum and $\epsilon_1 \leq \epsilon_2 \leq \dots \leq \epsilon_M$ is a set of single-particle entanglement energies (127). The constant ϵ_0 is fixed by normalisation. The assignment of occupation numbers is such that resulting spectrum is sorted by k . This is the same structure as the many-body energy spectrum of a free-fermion Hamiltonian. Hence, the interaction distance can be recast as a minimisation over these single-particle energies

$$D_{\mathcal{F}}(\rho) = \min_{\epsilon} \frac{1}{2} \sum_k |\rho_k - \sigma_k(\epsilon)|, \quad (3.5)$$

where ρ_k are the rank ordered eigenvalues of ρ .

Intriguingly, for most fermion system even when interactions are strong $D_{\mathcal{F}}$ is relatively small. For an example take the 1D Ising model, which can be mapped to the Majorana chain by means of a Jordan-Wigner transformation (90, 148). With only a transverse field this is a free fermion system, but the addition of the longitudinal field introduces long-range interactions to the Majorana picture. The interaction distances found in this model is small, at most around 10^{-3} close to the quantum critical point (166). Close to criticality, we find $D_{\mathcal{F}}$ to scale as a power-law, similar to the Widom scaling. The small values for $D_{\mathcal{F}}$ could be related to emergent quasiparticles which are to a large extent independent excitations but with a finite lifetime. We should emphasise that these need not be particles of a similar type to those the model is presented in, nor need this description extend beyond low-energy. We can find systems for which the interaction distance is much greater than these value, these are usually those that do not look at all like

a system of bosons or fermions.

3.4 Interaction distance in \mathbb{Z}_N -parafermion chains

We present an example where the interaction can have values both zero or very small, and much larger than what was found in the Ising model. These are generalisations of the Ising model known as the clock or Potts model which has a long history in statistical physics (18). Numerical evidence suggests that the largest $D_{\mathcal{F}}$ obtained here is in fact the maximum value obtainable for any system (109), something we could refer to as being maximally interacting. We will refer to these in an alternative picture, being made out of parafermionic degrees of freedom which are \mathbb{Z}_N generalisations of the Majorana fermion (54), where they are known as parafermion chains (8). This is to highlight how the low-energy physics could be thought of as producing parafermionic quasiparticles, and this underlies the differences seen in $D_{\mathcal{F}}$. Parafermions may be realised as fractionalised degrees of freedom at interfaces between different 2D topological phases (36, 112). The underlying physics of this model was recently realised in a Rydberg atom system (84) similar to the experiment motivating our work in the following chapters. Recent work shows that these systems may also host scarred dynamics (27).

In the parafermion language a simplified clock model is described by the Hamiltonian,

$$H_{\mathbb{Z}_N} = - \sum_j \alpha_{2j}^\dagger \alpha_{2j+1} - f \sum_j \alpha_{2j-1}^\dagger \alpha_{2j} + \text{h.c.}, \quad (3.6)$$

where α_j are the parafermion operators, satisfying generalised commutation relations $\alpha_j \alpha_k = \omega \alpha_k \alpha_j$ for $k > j$ with ω the N -th root of unity and $(\alpha_j)^N = 1$. This reduces to the transverse Ising model and Majorana fermions when $N = 2$. Typically clock models are studied with a variety of additional terms beyond those shown here (114).

For the most part we will discuss the fixed point $f = 0$ of the topologically non-trivial phase. Here, the ground state of a periodic chain has an entanglement spectrum that is N -fold degenerate, and has no other levels in its entanglement spectrum (50). This is related by the bulk-boundary correspon-

3. ENTROPY AND ENTANGLEMENT IN INTERACTING QUANTUM SYSTEMS

dence to the ground-state degeneracy of the open chain. This is a flat spectrum $\bar{\rho}(N) = \{\frac{1}{N}, \dots, \frac{1}{N}, 0, \dots\}$ with the $1/N$ eigenvalue repeated N times. We would like to determine the free spectrum σ most similar to $\bar{\rho}(N)$ and the interaction distance between them. Let n be the greatest integer such that $2^n \leq N$. We surmise that the solution is

$$\left\{ \frac{1}{N}, \dots, \frac{1}{N}, p, \dots, p \right\}, \quad (3.7)$$

where there are 2^n eigenvalues for each value $1/N$ and p . Normalisation of σ fixes $p = 2^{-n} - 1/N$. This guess is an element of the variational class the the minimum is taken over, hence it forms an upper bound

$$D_{\mathcal{F}}(\bar{\rho}(N)) \leq 3 - \frac{N}{2^n} - \frac{2^{n+1}}{N}. \quad (3.8)$$

In Figure 3.3 (b), we show that numerical calculations for $D_{\mathcal{F}}$ for flat spectra reveal that this upper bound is actually the exact result. We have verified this numerically up to $N = 2^8$ and by exact calculation up to $N = 6$ (109).

In Figure 3.3 (c) we show that moving away from the fixed point by changing f leaves $D_{\mathcal{F}}$ initially unchanged, until we get close to the critical point separating the topologically trivial and non-trivial phases. This is because the interaction distance like the entanglement spectrum tells us about the virtual edge excitations. Within the non-trivial phase there is a virtual parafermionic edge excitation which disappears on crossing the phase transition. This is mirrored by the plateau in $D_{\mathcal{F}}$ in the non-trivial phase followed by $D_{\mathcal{F}}$ becomes very small in the trivial phase. The inset shows how the interaction distance exponentially approaches the characteristic value for the phase as the size L_A of the subsystem is increased beyond the correlation length. For the case of \mathbb{Z}_4 parafermions, $D_{\mathcal{F}} = 0$ not only at the fixed point but for any value of f .

The supremum of the upper bound on $D_{\mathcal{F}}$ over flat spectra $\bar{\rho}$ is $3 - 2\sqrt{2}$, which is approached by rational approximations $N/2^n$ to $\sqrt{2}$ for increasing n . We conjecture that it is not possible to exceed this value for the interaction distance. Indeed, extensive numerical searches for a counterexample which exceeds this bound has failed. This highlights how parafermion models are very dissimilar to

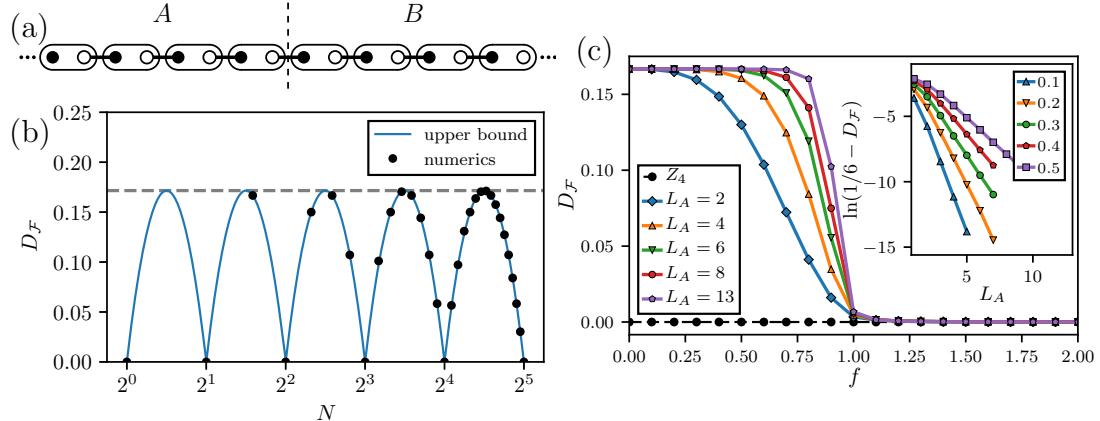


Figure 3.3: Interaction distance for parafermion chains. (a) Illustration of a parafermion chain at a fixed point, partitioned into subsystems A and B . (b) Interaction distance for parafermion chains at the non-trivial fixed point for \mathbb{Z}_N parafermion chains. The comparison is with the upper bound in Equation (3.8). The dashed line is the maximum value $3 - 2\sqrt{2}$. (c) Except where indicated this is for \mathbb{Z}_3 -parafermion chains and system size $L = 12$. Away from the fixed point, the interaction distance approaches a phase specific value when the subsystem size L_A is much larger than the correlation length. In contrast, for \mathbb{Z}_4 (data here is for $L = 8$) the interaction distance is always zero. (inset) Clearer view of the exponential convergence with L_A for \mathbb{Z}_3 parafermion chains. Lines are labelled with the value of f .

fermionic ones.

3.5 Conclusions

Entanglement is of increasing importance in the study of quantum many-body systems, improving our understanding particularly in the cases of symmetry-protected topological phases and topological order. The entanglement entropy and related entanglement spectrum are the most often employed, detecting correlations across the system. The entanglement entropy can be used to distinguish ergodic and non-ergodic systems, as well as the different forms of ergodicity breaking. In subsequent chapters, we will use entanglement measures to probe the usual dynamics of a Rydberg atom system.

We introduced a measure, the interaction distance, which distills information

3. ENTROPY AND ENTANGLEMENT IN INTERACTING QUANTUM SYSTEMS

about deviations from Gaussianity out of the entanglement spectrum. The interaction distance is of most interest when it is zero or merely very small. A striking feature of \mathbb{Z}_N -parafermion models is that some have exactly zero $D_{\mathcal{F}}$, as seen in Figure 3.3. This suggests there may be some way to “fermionise” these models. Indeed, an exact mapping to free fermions was subsequently identified in the case of \mathbb{Z}_4 parafermion chains (32). Such a strong result is not possible for higher powers of two, but there may still be a fermionisation of only the ground state or low-lying excitations. Beyond identifying non-interacting systems, small values for the interaction distance appear to indicate effective descriptions of the low-energy physics by fermionic or boson quasiparticles. The value of the interaction distance might be connected to the timescales at which low-energy configurations of quasiparticles relax, with higher quality quasiparticles featuring both lower $D_{\mathcal{F}}$ and longer lifetimes.

Chapter 4

Phenomenology of weak ergodicity breaking in a constrained quantum system

In this chapter we will focus on the behaviour of the Rydberg atom chain in the limit of strong van der Waals forces which produces a perfect Rydberg blockade. A recent experiment observed coherent oscillatory dynamics when quenched from a highly non-equilibrium state (19). In the model of this experiment, we will demonstrate the presence of strong quantum revivals where the entire wavefunction with good fidelity periodically recurs. We also find that the entanglement entropy contains a signature of these oscillations. The overall trend in the entanglement entropy is a linear increase in the quench experiment. However the slope depends strongly on the initial state with the Néel state initial configuration showing a slower rate of entanglement generation. This is surprising because the model cannot be included within our existing classifications of quantum systems which fail to thermalise, as discussed in Chapter 2. This remarkable fact is evidenced by the Wigner-Dyson class level statistics that the spectrum exhibits.

We will then relate the dynamical behaviour observed to the presence of a number of atypical eigenstates embedded among many typical eigenstates throughout the spectrum. The relationship between dynamics and eigenstates is illustrated with a discussion of the consequences of perfect quantum revivals on the

4. PHENOMENOLOGY OF WEAK ERGODICITY BREAKING IN A CONSTRAINED QUANTUM SYSTEM

eigenstates and spectrum. We will also examine matrix elements of some local observables and compare findings against the predictions of the eigenstate thermalisation hypothesis (ETH). In this we will see the presence of the atypical eigenstates and suggest that even the typical states parametrically disagree with the ETH prediction. These findings will show this model to be a very interesting system in which to explore quantum dynamics.

4.1 Cold-atom quantum simulators

The experimental platform is cold neutral atoms coupled with highly-excited Rydberg states (82, 175), see Figure 4.1. Transitions are laser driven between the ground state of individual atoms $|\circ\rangle$ and a Rydberg state $|\bullet\rangle$, passing through an intermediate state. These experience repulsive van der Waals interactions with a strength $V_{i,j} \approx Cr_{i,j}^{-6}$ ($C > 0$) between pairs of atoms $\{i, j\}$ both in the Rydberg state at a separation of $r_{i,j}$. The kind of set-up can be used to implement quantum gates (80, 82, 139, 178). An effective Hamiltonian, without explicit time dependence, for this system is as follows:

$$H = \sum_j \left(\frac{\Omega_j}{2} X_j - \Delta_j Q_j \right) + \sum_{i < j} V_{ij} Q_i Q_j, \quad (4.1)$$

where Δ_j are the laser detunings and Ω_j are the effective Rabi frequencies. The operator X_j generates transitions between $|\circ\rangle$ and $|\bullet\rangle$ on atom j , while Q_j projects into the Rydberg state $|\bullet\rangle$ on atom j . The parameters Δ_j and Ω_j are individually controllable by adjusting the intensity and frequency of the laser drive to each atom. The interaction energies V_{ij} can also be controlled by changing the distance between the atoms. In absence of the interactions, isolated atoms undergo Rabi oscillations. At resonance $\Delta = 0$, the atoms oscillate between the \circ and \bullet states.

The strong interactions between Rydberg atoms produces an effective constraint which removes the possibility of simultaneous excitation in Rydberg states when the atoms are sufficiently close. This effect is known as the Rydberg blockade (82), which forms the basis for the implementation of quantum gates in Rydberg atom systems (80, 139, 178). The blockade radius R_b is defined as the

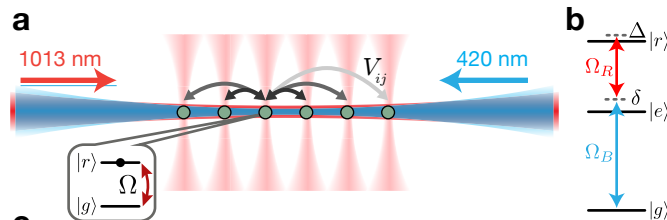


Figure 4.1: Experimental platform consisting of individual cold atoms trapped and arranged by optical tweezers. The atoms are laser driven into a highly-excited Rydberg state. Controllable interactions are present between nearby atoms in their Rydberg states. Figure is reproduced from Ref. (19).

separation at which $V_{i,j} = \Omega$. Effectively, within this radius simultaneous excitation is prevented and outside it excitations are independent.

The operation of the quantum simulator starts with the insertion of atoms into the tweezer array. The atoms are then manipulated into a chosen arrangement (16, 48, 89) and brought into their simultaneous ground state $|\circ\circ\circ\cdots\rangle$ by optical pumping. After this initialisation, the traps are switched off and the system is left to evolve under the Hamiltonian H as the tunable control fields $\Omega(t)$ and $\Delta(t)$ can be varied. The optical trap is then turned back on. Since the Rydberg state $|\bullet\rangle$ is anti-binding to the trapping potential, it is ejected from the trap. The final state is observed with fluorescent imaging, measuring the positions of atoms within the trap and, effectively, the state each atom was in before the trapping was resumed.

When Δ/Ω is large and negative the ground state has each atom in their \circ state. On the other hand, when Δ/Ω is large and positive the ground state is a state where the number of atoms in their Rydberg state is maximised, subject to the Rydberg blockade constraints. These states are the so-called Rydberg crystals (51, 129), with different orders corresponding to spontaneously breaking translation symmetry. In the experiment reported by Ref. (19), the system is first prepared as described above before adiabatic sweeping from large negative Δ/Ω to large positive. This prepares a Rydberg crystal state depending on the blockade radius, see the schematic in Figure 4.2. In the particular case of $V_{i,i+1} \gg \Delta \gg \Omega \gg V_{i,i+2}$ this process prepares a \mathbb{Z}_2 Rydberg crystal $|\bullet\circ\circ\circ\cdots\rangle$. This is analogous to the Néel antiferromagnetic order, or a \mathbb{Z}_2 charge density wave.

4. PHENOMENOLOGY OF WEAK ERGODICITY BREAKING IN A CONSTRAINED QUANTUM SYSTEM

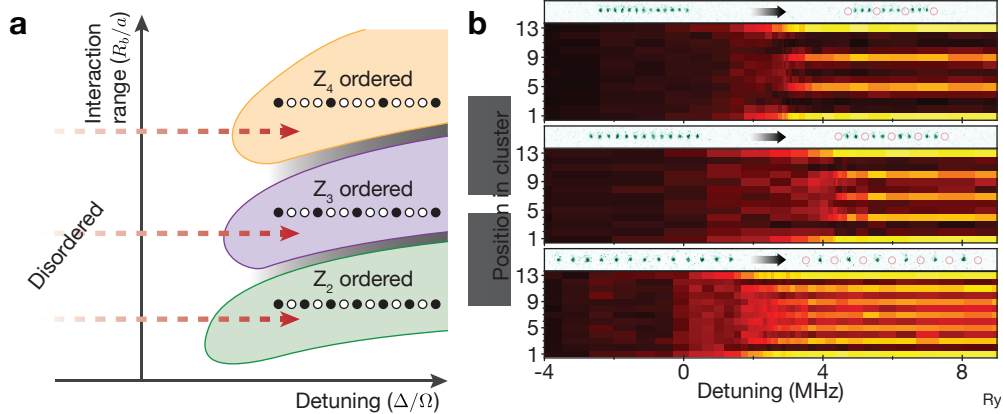


Figure 4.2: Schematic showing how various Rydberg crystal states (51, 129) can be prepared by an adiabatic sweep from large negative to large positive Δ/Ω . (a) The particular crystal states obtained depends on the interaction strength C , through the blockade radius R_b . (b) Excitation probability across the preparation sweep for different Rydberg crystals. Figure is reproduced from Ref. (19).

Similarly, other Rydberg crystals, such as Z_3 and Z_4 orders, can be prepared by expanding the Rydberg radius.

After preparing an initial Z_2 Rydberg crystal a quench is taken to resonance ($\Delta = 0$). As the system is left to evolve it was found to periodically return, with high probability, to its initial Z_2 configuration, passing through the other Z_2 crystal translated by a single site, $|\circ\bullet\bullet\cdots\rangle$. The oscillations can be quantified with the domain wall density, where a domain wall is a $\circ\bullet$ pattern. The quench is performed many times, stopping and measuring the state of each atom after different amounts of time has elapsed to build a picture of what happens when the system is left to evolve. These experimental results are reproduced in Figure 4.3. The domain wall density was found to oscillate beyond the local relaxation timescale $1/\Omega$. In Ref. (19), a matrix product state (MPS) description of the dynamics is found which qualitatively reproduces these oscillations, the result of this approximation is also shown in Figure 4.3.

The finding is surprising, given that there are no known conserved quantities beyond energy and spatial reflection, and is far from any known integrable point (51). We should expect such a system to thermalise rapidly, especially considering that the initial state energy-density corresponds to an infinite-

4.2 Effective model, Hilbert space and symmetries

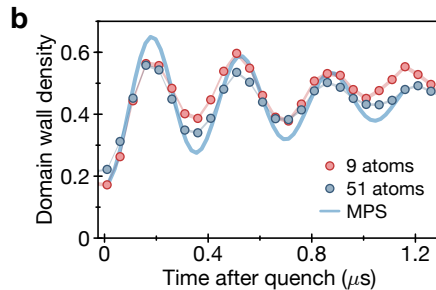


Figure 4.3: Domain wall density features coherent oscillations following a quench. These last much longer than the natural relaxation timescale $1/\Omega$. Frequency is largely independent of system size. The MPS line is a matrix-product state approximation to the time-evolution from Ref. (19). Figure is reproduced from Ref. (19).

temperature ensemble within the subspace that satisfies the Rydberg blockade constraint. In Chapter 4, we will examine this problem using the numerical solution of an effective model for the system. There we will find that this feature is highly state dependent. Most initial states with the same mean energy will thermalise rapidly. This contrast is unexpected in conventional forms of ergodicity breaking.

4.2 Effective model, Hilbert space and symmetries

The local Hilbert space for each atom is taken to have two states: the ground state \circ and an excited, or Rydberg, state \bullet . The transition between these two states is laser driven at resonance producing Rabi oscillations. However, strong van der Waals interactions between adjacent excitations shift their energies and take transitions off-resonance in this case. Oscillations are hereby prevented from forming adjacent excitation $\bullet\bullet$ patterns. The effective dynamics generates transitions between \circ and \bullet locally, but only if both adjacent atoms are in their ground states. The following are examples of allowed and disallowed transitions:

$$\circ\circ\circ \leftrightarrow \circ\bullet\circ, \quad \circ\circ\bullet \not\leftrightarrow \circ\bullet\bullet. \quad (4.2)$$

4. PHENOMENOLOGY OF WEAK ERGODICITY BREAKING IN A CONSTRAINED QUANTUM SYSTEM

This dynamical constraint leaves the Hilbert space highly reducible. Each $\bullet\bullet$ is a frozen pattern and its presence or absence in a particular location is an integral of motion. Wherever these patterns occur the system is split into two isolated systems, on either side of the pattern, terminating with open boundaries. We can therefore consider only the sector (or component) where all configurations with two adjacent excitations $\bullet\bullet$ are excluded, and in this sector the dynamics is closed. We will also refer to this as the constrained Hilbert space.

We can write a Hamiltonian for the effective dynamics as

$$H = \sum_{j=1}^N P_{j-1} X_j P_{j+1}, \quad (4.3)$$

where N is the number of sites, from which we derive the name ‘‘PXP’’ model. The Pauli matrix X_j generates spin flips on atom j and $P_j = |\circ\rangle_j \langle\circ|_j$ is a projector into the \circ state of atom j . The derivations of Equation (4.3) will be discussed in more detail in Section 4.5.1. It will be useful to define orthocomplementary projectors $Q_j = 1 - P_j$. The local operator algebra satisfies the relations

$$XP = QX, \quad X^2 = 1, \quad P^2 = P, \quad Q = 1 - P, \quad (4.4)$$

where the subscript tensor factor labels were omitted. Naturally, operators acting on different tensor factors commute. Another operator that we use is $Z_j = Q_j - P_j$ which anti-commutes with X_j . Periodic boundary conditions are implemented by identifying site $N+1$ with site 1. For open boundaries we add the boundary terms $X_1 P_2$ and $P_{N-1} X_N$ and remove any term which would be undefined. This Hamiltonian as written is valid for all the different irreducible components (according to the frozen patterns), but we will interpret it as only acting on the component free of frozen patterns.

Now we turn to determining the dimension of the constrained Hilbert space \mathcal{P} . Let d_n be the dimension of the constrained Hilbert space of a open system of n sites. We may glue on the left end of the system the pattern \circ or $\bullet\circ$, regardless of what basis configuration is to the right, to form another allowed basis configuration. Each allowed configuration is either prefixed with \circ or $\bullet\circ$ and then what follows is an allowed configuration. This establishes a one-to-

4.2 Effective model, Hilbert space and symmetries

one correspondence between those configurations of n sites prefixed by \circ and configurations of $n - 1$ sites; and also between those configurations of n sites prefixed by $\bullet\circ$ and configurations of $n - 2$ sites. From this we may deduce that the dimension satisfies the linear recurrence

$$d_n = d_{n-1} + d_{n-2}, \quad (4.5)$$

with initial conditions $d_0 = 1$ and $d_1 = 2$. This generates the well-known Fibonacci sequence.

The periodic system Hilbert space for n sites can be formed by taking the open Hilbert space of the same number of sites and removing the configurations which both begin and end with \bullet . This implies that

$$d_n^{\text{PBC}} = d_n - d_{n-4}, \quad (4.6)$$

where d_n^{PBC} is the dimension of the constrained Hilbert space for a system of n sites with periodic boundary conditions.

Finally, we discuss the symmetries of the PXP model of Equation (4.3). Restriction to particular symmetry sectors is essential when calculating measures of quantum chaos such as the level statistics, and greatly reduces the computational cost in calculations. The PXP model has a spatial inversion symmetry I which maps sites $j \mapsto L - j + 1$. For periodic boundary conditions the system also has a translation symmetry producing in total a dihedral group for the space group symmetries. Additionally, there exists an operator,

$$\mathcal{C} = \prod_j Z_j, \quad (4.7)$$

which anticommutes with the Hamiltonian. This produces a spectral reflection symmetry in the energy spectrum where each eigenstate at an energy E (for $E > 0$) is partnered with another at an energy $-E$. Unless otherwise specified, results will be given for periodic boundary conditions with the spatial symmetries taken into account. In this way we can obtain the full eigendecomposition of the Hamiltonian for large systems up to $N = 32$ sites.

4. PHENOMENOLOGY OF WEAK ERGODICITY BREAKING IN A CONSTRAINED QUANTUM SYSTEM

4.3 Quantum revival

We previously saw that some local observables display long-lived oscillations when the system is prepared in the Néel state. As we will demonstrate below, we can see the stronger phenomenon of quantum revivals, which is a periodic recurrence in the state of a quantum system (136). Let the state at time t be $|\psi(t)\rangle$ and define a function

$$g(t) = |\langle\psi(0)|\psi(t)\rangle|^2. \quad (4.8)$$

This is variously known as the Loschmit echo, return probability or autocorrelation function. A quantum revival occurs when this return probability reaches some appreciable fraction of unity (the quality of the revival) for a time that is longer than the energy scales involved but shorter than the exponentially long timescale of a quantum Poincaré recurrence (23). These Poincaré recurrences are disregarded because they are a generic effect of a finite number of degrees of freedom and their timescales are much longer than what could be observed in experiment. If a system undergoes periodic quantum revival then all non-trivial observables will pick up this oscillatory behaviour explaining the non-equilibrium dynamics observed in experiment. In Figure 4.4 (a) we show (as also reported in Ref. (19)) that this effective model exhibits quantum revivals following a quench from a Néel state. This can also be seen in the oscillatory behaviour of local observable expectation values such as a local Z operator as shown in Figure 4.4 (b). In the experiments a more complicated observable detecting domain walls between different \mathbb{Z}_2 charge-density waves was used (19). In this section, we will familiarise ourselves with some general results of perfect revivals, focussing on the spectral properties, to build an intuition on what features are related to quantum revivals. Then we shall numerically examine the eigendecomposition of Equation (4.3) for these signatures.

It will be helpful to consider the time-evolution operator,

$$U(t) = \exp(-iHt). \quad (4.9)$$

We will say that a state $|v\rangle$ is periodic if there exists some time τ and a scalar γ

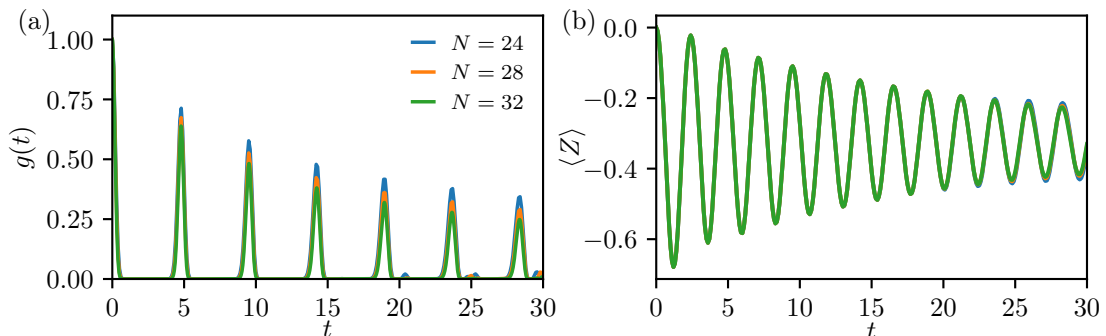


Figure 4.4: Oscillatory dynamics of the effective model Equation (4.3) following a quench to a Néel state. (a) Periodic revival can be seen in the return probability or fidelity $g(t)$ of Equation (4.8). (b) Oscillations in local observable Z expectation value are consistent between system sizes N for times $O(N)$. Data shown is for a periodic system of system size N .

such that

$$U(\tau) |v\rangle = \gamma |v\rangle, \quad (4.10)$$

with $|\gamma| = 1$. To describe the relationship between periodicity and the eigenvalue decomposition we will make use of a few concepts. Firstly, the eigenvalue support of a state $|u\rangle$ is the set of all eigenvalues θ_r of H where $\langle r|u\rangle \neq 0$ for a corresponding eigenvector $|r\rangle$. Secondly, the r -th order Krylov subspace generated by an operator H and $|v\rangle$ is

$$\mathcal{K}_r(H, |v\rangle) = \text{span}\{|v\rangle, H|v\rangle, H^2|v\rangle, \dots, H^{r-1}|v\rangle\}. \quad (4.11)$$

If for any $|v\rangle$ in a subspace V the image $H|v\rangle$ is contained within V then we say that V is H -invariant or closed under H . If our original vector space is finite-dimensional then clearly \mathcal{K}_r will be closed for some r . This closed Krylov subspace is also the minimal H -invariant subspace that contains $|v\rangle$, which can be seen because given the subspace contains $H^k|v\rangle$ it must contain $H^{k+1}|v\rangle$ in order to be H -invariant. Hence, by induction, any such closed subspace must contain this closed Krylov subspace. The eigenvalues contained within the closed Krylov subspace are the eigenvalue support of $|v\rangle$. The significance of the eigenvalue support will be made clear in the following proof reproduced from Ref. (61).

Theorem 1 (Ratio condition). *Let u be a vector which is periodic under U . For*

4. PHENOMENOLOGY OF WEAK ERGODICITY BREAKING IN A CONSTRAINED QUANTUM SYSTEM

any $\theta_k, \theta_l, \theta_r, \theta_s$ eigenvalues in the support of u and $\theta_r \neq \theta_s$ then

$$\frac{\theta_k - \theta_l}{\theta_r - \theta_s} \in \mathbb{Q}. \quad (4.12)$$

This condition is known as the ratio condition.

Proof. Since u is periodic then there exists time τ and constant γ , with $|\gamma| = 1$, such that

$$\langle u | U(\tau) | u \rangle = \gamma. \quad (4.13)$$

Because $U(\tau)$ is unitary we have

$$\gamma |u\rangle = \sum_r \exp(-i\theta_r \tau) |r\rangle \langle r|u\rangle. \quad (4.14)$$

Now the vectors $|r\rangle$ form an orthonormal basis, and so

$$\exp(-i\theta_r \tau) = \gamma \quad (4.15)$$

for all $|r\rangle$ in the support of $|u\rangle$ and consequently $\tau(\theta_k - \theta_l)$ is a integer multiple of 2π . \square

It should be clear that if the ratio condition (4.12) holds in the eigenvalue support of $|u\rangle$, then $|u\rangle$ is periodic. Theorem 1 reveals that this condition is also necessary.

Corollary 1. *Consider a generic local many-body Hamiltonian H , with bandwidth $\|H\| = O(N)$ growing with the volume N . If a state $|v\rangle$ is periodic under the time evolution with a period $\tau = \Theta(1)$ convergent with system size N , then $|v\rangle$ can be decomposed as a linear combination of $O(N)$ energy eigenstates, and at least one of them $|u\rangle$ will have large overlap $|\langle u|v\rangle|^2 = \Omega(1/N)$ with the periodic state.*

Proof. Without loss of generality, one may choose a basis $\{|\mu\rangle\}$ of energy eigenstates where for each eigenvalue in the support of $|v\rangle$ there is exactly one basis state with non-zero overlap with $|v\rangle$. This is because $|v\rangle$, projected into a degenerate eigenspace, provides a eigenvector with non-zero overlap with $|v\rangle$. Then we can choose additional basis vectors within the subspace, mutually orthogonal and orthogonal with the projected vector, to form a basis.

In Theorem 1 we found that $\tau(\theta_k - \theta_l)$ was an integer multiple of 2π for any pair of eigenvalues θ_k, θ_l in the eigenvalue support of $|v\rangle$. This provides a minimum spacing between these eigenvalues and implies that there are $O(N)$ energy eigenvalues in the support of $|v\rangle$. Consequently at least one of the corresponding eigenvectors $|u\rangle$ has overlap $\Omega(1/\sqrt{N})$ with $|v\rangle$. \square

With these results on perfect revivals in mind, we turn back to our Rydberg atom system with its imperfect revivals. In Figure 4.5 we show the weight $|\langle \mathbb{Z}_2 | E \rangle|^2$ of each eigenstate E on the Néel state and the corresponding eigenvalues E for a periodic chain of length $N = 32$, produced by exact diagonalisation. The most striking feature is the band of high weight states with approximately equal energy spacings which are indicated with the red circles. The number of states in this band at each size is $N + 1$, with half of these states found in the zero-momentum, inversion-even sector and the others found in the π -momentum, inversion-odd sector. These states account for most of the weight of the Néel state and are an indication of the persistent revivals seen previously. Motivated by the significance of these states for describing the revivals we will in subsequent chapters seek an approximation scheme which finds these eigenvalues and their weights in the Néel state. Beside these most significant contributions, the eigenstates arrange themselves into “towers”, clusters of eigenstate at energies around those of the special states with atypically large overlap with the \mathbb{Z}_2 state. Together these give a comb-like shape to the energy-overlap plot of Figure 4.5.

4. PHENOMENOLOGY OF WEAK ERGODICITY BREAKING IN A CONSTRAINED QUANTUM SYSTEM

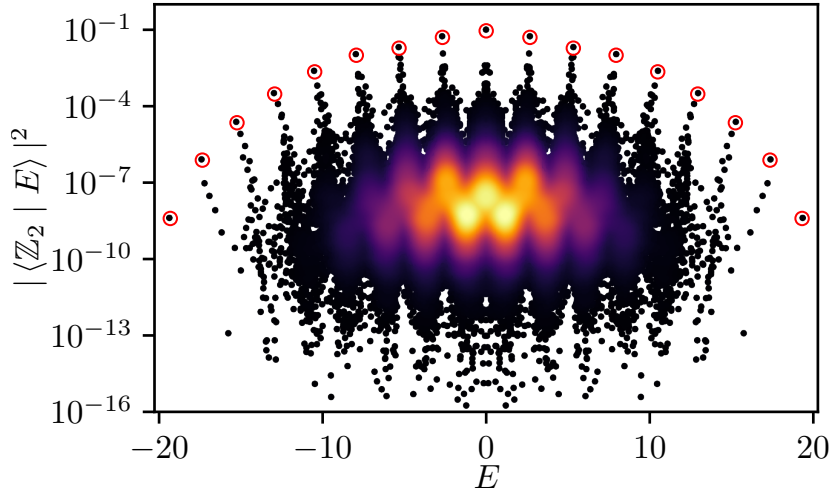


Figure 4.5: Scatter plot of energy and overlap with the Néel state for eigenstates. This exhibits a number of so-called special states highlighted by the red circles with anomalously large overlap. Where the density of points is high, colour is used to indicate their density. Data shown is for periodic system of size $N = 32$ in the $k = 0, I = +1$ sector.

4.4 Signatures of quantum chaos

In light of the highly regular dynamics observed in Figure 4.4, we might suspect that the system is close to some integrable point where it would be solvable exactly. There are even a number of known candidate integrable points in the vicinity of Equation (4.3) (49, 51), such as the Golden chain which is Yang-Baxter integrable. This is a quantum spin chain formulation of the A_4 restricted solid on solid (RSOS) model (11). However from all these the Hamiltonian differs by several terms with $O(1)$ couplings, thus it is not in a standard sense perturbatively close to these integrable points. From an analysis of several standard diagnostics of quantum chaos, we will show that our model is much more similar to chaotic systems than to integrable ones.

We will first examine the energy level spacing distribution (21, 125). Recall that in an ergodic and non-integrable phase we expect energy levels to exhibit spectral repulsion, whilst in an integrable system, or a many-body localised system (125), the integrals of motion cause an absence of level repulsion. A more detailed prediction for the level statistics of ergodic phases is found in the Wigner-

Dyson classes, which predicts a distribution of “unfolded” energy level spacings $P(s) = \left\langle s - \frac{E_{a+1} - E_a}{\delta_a} \right\rangle$ where δ_a is a mean level spacing. This unfolding is designed to control for the effects of a varying density of states, up to first order. For Hamiltonians that can be modelled as real symmetric matrices, such as the PXP model, the appropriate random matrix ensemble is the Gaussian orthogonal ensemble (GOE). In Figure 4.6 (a) we plot the distribution $P(s)$ which is found to be in good agreement with the Wigner-Dyson prediction for system size $N = 32$. There is an additional complication in that the model has an exponential number of states exactly degenerate at zero energy (in the middle of the spectrum) due to the interplay of symmetry, sublattice structure in the Hamiltonian and the Hilbert space structure explained in Ref. (145, 167, 168). This requires that these degenerate eigenvalues are removed before calculating level statistics.

In Figure 4.6 (b), we show the so-called r -statistic (120),

$$\langle r \rangle = \left\langle \frac{\min\{E_{i+1} - E_i, E_i - E_{i-1}\}}{\max\{E_{i+1} - E_i, E_i - E_{i-1}\}} \right\rangle_i. \quad (4.16)$$

It is useful because it removes dependence on the local density of states. As a single scalar statistic it is helpful for comparing a number of different systems and here provides an easier way to see the approach to the Wigner-Dyson ensemble with system size than examining the unfolded distributions $P(s)$. For the GOE the r -statistic gives $\langle r \rangle \approx 0.53$. For comparison, most integrable and many-body localised systems follow a Poisson statistics, since the energy levels are uncorrelated, which predicts $\langle r \rangle \approx 0.39$. Both level statistic measures provide good evidence that the model does not fall into one of the existing classes of non-ergodic models: those of exactly solvable, integrable or many-body localised systems.

In order to better understand the structure of the eigenstate we examine their components in the computational basis. The second participation ratio of an eigenstate ψ is a moment of the product state probability distribution for that state, explicitly

$$\text{PR}_2 = \sum_{\alpha} |\langle \alpha | E \rangle|^4, \quad (4.17)$$

4. PHENOMENOLOGY OF WEAK ERGODICITY BREAKING IN A CONSTRAINED QUANTUM SYSTEM

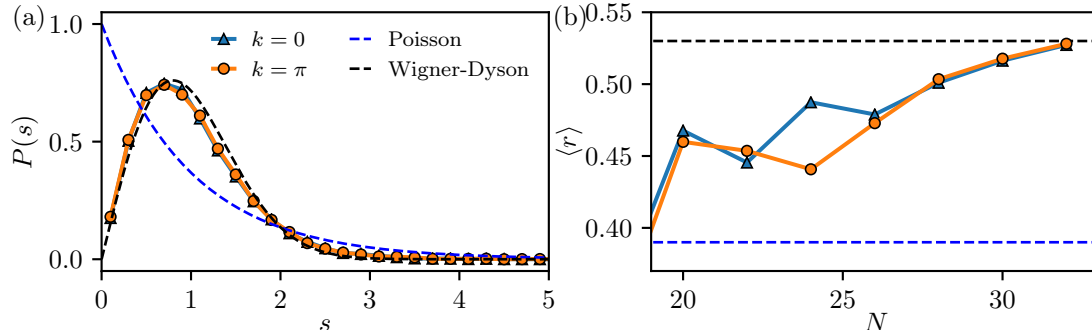


Figure 4.6: Absence of level repulsion in the PXP model. (a) Distribution of unfolded level spacings $P(s)$ for system size $N = 32$ exhibits level repulsion and is well described by the Wigner-Dyson prediction. (b) The r -statistic travels with increasing system size N towards the Wigner-Dyson GOE value of $\langle r \rangle \approx 0.53$. Data shown is for the $k = 0$, $I = +1$ and $k = \pi$, $I = -1$ sectors. Eigenvalues at zero energy have been removed because of an exponential degeneracy.

where the sum is over the basis of product states α with a definite value of Z_j for all j . It is a measure of the concentration or localisation of a state in a particular basis. In the context of Anderson localisation, PR_2 is used to characterise the localisation of wavefunctions in real-space (94). The classical configurations have identical mean energy and similar energy variances (each the square root of the number of sites which can undergo transition). Because of this, the ergodic hypothesis would predict that eigenstate would be delocalised in the product state basis, as a many-body analogue of the Berry-Tabor conjecture (21). In Figure 4.7 we plot the participation ratio PR_2 averaged alternately over typical eigenstates or only those special states. Typical states have a participation ratio which decays, consistent with the prediction, but the special states exhibit a participation ratio which decays at a rate much slower than predicted.

The leading theory of thermalisation in quantum many-body systems is the eigenstate thermalisation hypothesis (ETH) (44, 133, 159), which we reviewed in Chapter 2. In this scenario, individual eigenstates are expected to effectively reproduce the microcanonical ensemble for some family of physical observables (41). The ETH is an assumption about the form of observable matrix elements $O_{\alpha\beta} = \langle E_\alpha | O | E_\beta \rangle$, where $|E_\alpha\rangle$ is a highly-excited energy eigenstate, see Equation (2.7).

4.4 Signatures of quantum chaos

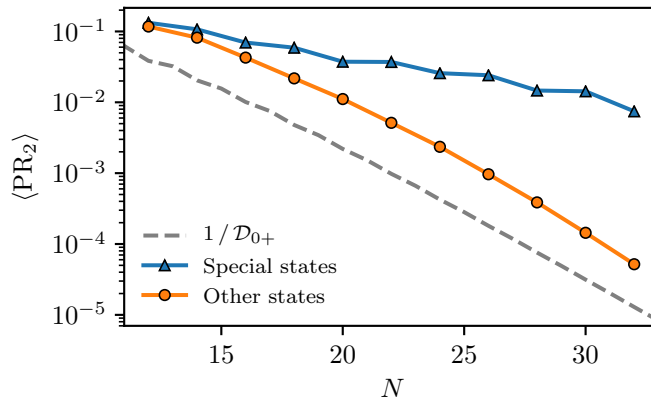


Figure 4.7: Participation ratios for eigenstates over the product state basis decays exponentially with system size. The dashed line shows the expected behaviour for typical states satisfying Berry’s conjecture. \mathcal{D}_{0+} is the dimension of the symmetry sector. The line labelled “special states” is the mean participation ratio for the middle 2/3 of the special states in order to exclude low-energy states. The participation ratio of special states decays at a rate inconsistent with the prediction. The line labelled “other states” is the mean of all states which are not special states and in contrast decays at a rate similar to the prediction. Data shown is for the $k = 0$, $I = +1$ sector.

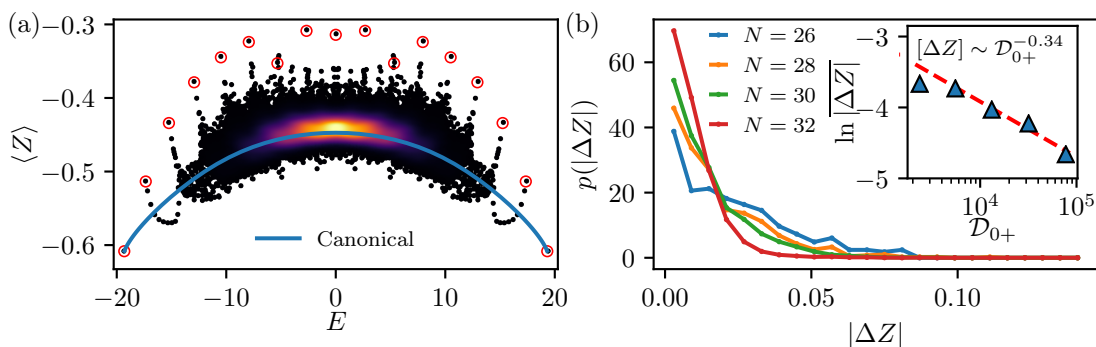


Figure 4.8: Diagonal matrix elements of Z in the energy eigenbasis. (a) Scatter plot of matrix elements against energy. The special states indicated with red circles have atypical matrix elements in violation of the ETH prediction. These have a greater density of excitations compared to typical states. The blue line shown is the expectation value of Z in a canonical ensemble with a mean energy of E . Data shown is for $N = 32$ in the $k = 0$, $I = +1$ sector. (b) Distribution of differences in diagonal matrix elements ΔZ for the observable in adjacent energy levels. Inset: the scaling of mean diagonal differences against symmetry-resolved Hilbert space dimension \mathcal{D}_{0+} follows a power law but the ETH prediction of the exponent is not met.

4. PHENOMENOLOGY OF WEAK ERGODICITY BREAKING IN A CONSTRAINED QUANTUM SYSTEM

In Figure 4.8 we show the diagonal matrix elements in the energy eigenbasis of an observable Z on an arbitrary site. The special states are highlighted with red circles. The line is the expectation value found in a thermal state with mean energy E . The typical expectation value around infinite temperature is non-zero as a result of the Hilbert space constraints. Once again, we see that the special states identified previously form outliers from the typical behaviour which clusters around the canonical ensemble prediction. Following Ref. (88) we define the differences of the diagonal matrix elements,

$$(\Delta Z)_\alpha = |\langle E_{\alpha+1} | Z | E_{\alpha+1} \rangle - \langle E_\alpha | Z | E_\alpha \rangle|. \quad (4.18)$$

The diagonal differences are insensitive to the smooth variation in the micro-canonical and envelope functions, provided the density of states is sufficiently high as these scale as $\exp^{-S(E)}$, where $S(E)$ is the thermodynamic entropy, and are thus much smaller than fluctuations in the second term of Equation (2.7). In Figure 4.8 we show the distribution of diagonal differences which narrows with increasing system size around zero. The data is selected from an interval $[0.05, 1.1]$ to avoid the degeneracy at zero energy and the edges of the spectrum where the density of states is much lower. In the inset we show the scaling of the mean diagonal difference with system size N up to $N = 32$; here \mathcal{D}_{0+} refers to the dimension of the symmetry-resolved Hilbert space, see Table 4.1. The dependence can be fit with a power-law but the exponent found (-0.34) differs from the ETH prediction of -0.5 . In more conventional systems ETH predictions can be confirmed in systems with Hilbert space dimensions significantly smaller than the largest sectors considered here (131, 132). However only the largest system sizes appear to be converged, thus we cannot rule out the possibility that the exponent flows with system size towards the ETH value. In integrable systems the observable matrix element can look similar to the ETH scenario, however the fluctuations only decay polynomially in system size (5).

The ETH was tested previously in a Fibonacci anyon chain (33) formed by taking the integrable Hamiltonian of Ref. (49) and adding anyon appropriate perturbations which break integrability. This system has a similar constrained Hilbert space structure although the Hamiltonian differs from the effective model

4.4 Signatures of quantum chaos

N	20	22	24	26	28	30	32
d_N	15 127	39 603	103 682	271 443	710 647	1 860 498	4 870 847
\mathcal{D}_{0+}	455	1 022	2 359	5 536	13 201	31 836	77 436

Table 4.1: Table of Hilbert dimensions for periodic systems of size N . d_N is the full Hilbert space dimension while respecting constraints. \mathcal{D}_{0+} is the dimension of the zero-momentum and inversion-even subspace.

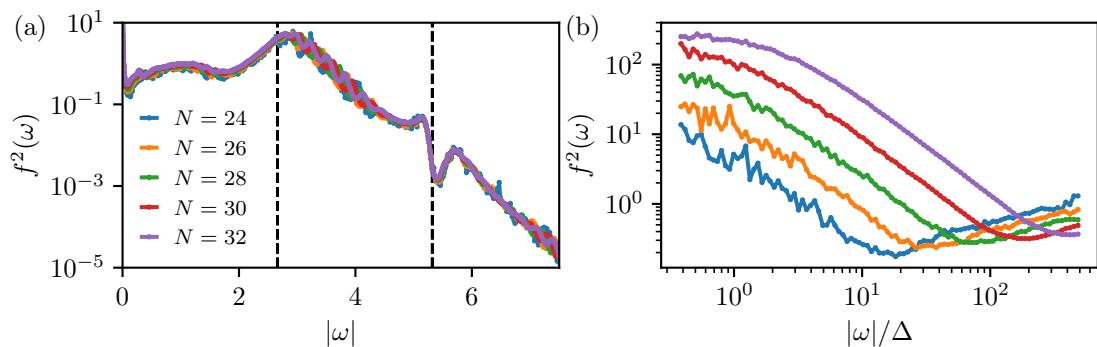


Figure 4.9: Envelope function controlling the off-diagonal matrix elements of the Z observable. (a) Envelope function $f^2(E, \omega)$ integrated over energy and plotted as a function of ω . This is independent of system size and decays exponentially with ω consistent with a local model satisfying ETH. However, a number of features appear at some of the harmonics of the oscillation frequency. These are indicated by the dashed lines. (b) With the frequency rescaled in terms of the mean many-body level spacing Δ , there is no well-developed Thouless plateau at this minimum energy scale. The largest sizes available show some rounding suggestive of the appearance of a Thouless plateau at larger sizes.

of Rydberg atoms in Equation (4.3). They found that the ETH predictions were satisfied, which means that these differences cannot be simply attributed to the constraints.

We can isolate the envelope function from the off-diagonal matrix elements as follows:

$$f^2(E, \omega) = e^{S(E)} \langle |\langle \beta | Z | \alpha \rangle|^2 \delta(E_\alpha - E_\beta - \omega) \rangle_{\alpha, \beta}, \quad (4.19)$$

where the angle brackets $\langle \cdot \rangle_{\alpha, \beta}$ denote averaging over all pairs of eigenstates α and β . In Figure 4.9 (left) we see that at large ω the envelope function decays exponentially. This is the expected behaviour for local systems where large ω transitions are many-body processes that appear only at high orders in pertur-

4. PHENOMENOLOGY OF WEAK ERGODICITY BREAKING IN A CONSTRAINED QUANTUM SYSTEM

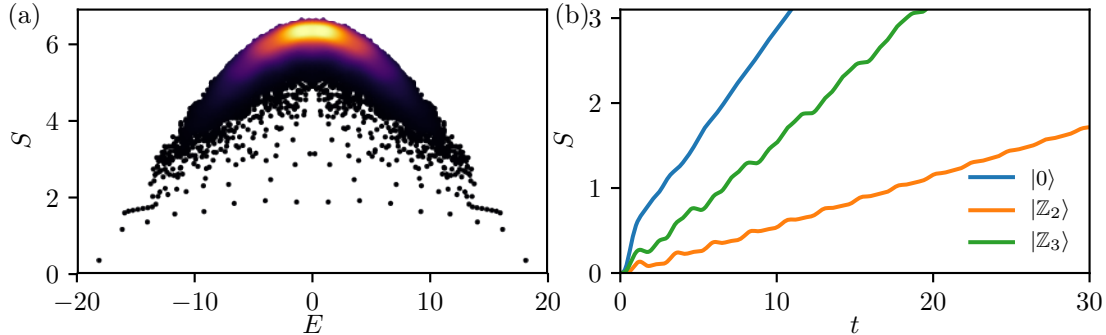


Figure 4.10: Entanglement entropy for the PXP model. (a) Scatter plot of energy and bipartite von Neumann entanglement entropy for eigenstates of a periodic system of $N = 32$ sites. (b) Growth of bipartite entanglement entropy following various product state quenches in an infinite system with open boundary conditions. $|0\rangle = |\circ\circ\circ\circ\dots\rangle$

bation theory (3, 117). At intermediate ω , we see non-monotonic behaviour at frequencies corresponding to harmonics of the oscillation frequency $E \approx 1.33$. These kind of features can appear in thermalising systems but there they are found at frequencies that scale as $1/N$ (41). We could interpret this as a sign that the bulk of the eigenstates have an imprint of the special states and are not fully random.

Another feature of thermalising systems is that $f^2(\omega)$ at small ω saturates to a value constant with respect to ω , a feature known as a Thouless plateau (46, 93). This sets a maximum energy scale after which we expect observables to have thermalised. In Figure 4.9 (right), we once again show the envelope function however focussing on the very small ω regime. We rescale the frequency by the mean level spacing Δ (as a function of energy) to show that there is little sign of a Thouless plateau even at the scale of adjacent energy levels. There appears a rounding of the curve with system size which is suggestive of the eventual appearance of a plateau at some larger size.

Thermalisation of all observables within a small subsystem \mathcal{A} , as expected in the eigenstate thermalisation scenario, implies the entanglement entropy is equal to the thermodynamic entropy of \mathcal{A} at a temperature T . The thermodynamic entropy is an extensive quantity, scaling in proportion to the volume of \mathcal{A} and is greatest in the middle of the spectrum where the many-body density of states is

greatest. In Figure 4.10 (a) we show the bipartite von Neumann entanglement entropy. This means the subsystem \mathcal{A} is chosen to be some contiguous set of $N/2$ atoms out of the total of N . The bulk of the eigenstates fall onto a parabola showing that most of the eigenstates cluster around the thermodynamic entropy as would be expected in a thermalising system. Against the pattern however, outliers are again visible with much lower than typical entropy. These are the same states identified by their atypical overlap with the $|\mathbb{Z}_2\rangle$ states. It is however not possible to reliably distinguish between linear and logarithmic scaling with N for these outlier states over the limited range of system sizes available. Integrable systems can show this same phenomena of rare states with greatly reduced entanglement entropy (5, 144), but remember that these typically follow Poisson level statistics.

In chaotic systems the initial growth of entanglement in such a quench experiment is linear in time, however this is not a reliable sign of chaotic dynamics. Indeed, integrable systems can show this same phenomenon despite forming the prototypical non-chaotic systems. The converse implicate works better; in Anderson localised systems where the entanglement growth saturates quickly to a non-extensive value and in many-body localised systems where the growth is logarithmic (14, 186). We show the growth of entanglement following a quench from various product states in Figure 4.10 (b). This calculation was performed using the time-evolving block decimation (TEBD) algorithm directly in the thermodynamic limit of an open boundary system, the so-called infinite boundary conditions (170). In this technique computational complexity is controlled by the entanglement giving a window into the short-time dynamics where the entanglement is relatively small. The results are converged in the maximum bond dimension for the times shown in the figure. What we see in this system however is a strong dependence of the slope on the initial state. With the initial state being $|\mathbb{Z}_2\rangle$ the linear growth is much reduced from typical configurations which behave more similarly to the polarised state, denoted $|0\rangle$ here.

4. PHENOMENOLOGY OF WEAK ERGODICITY BREAKING IN A CONSTRAINED QUANTUM SYSTEM

4.5 Effect of perturbations

So far we have seen interesting dynamical and eigenstate properties in the pure PXP model. We expect the phenomena observed to be unstable under generic perturbations leading to the restoration of conventional thermalisation. However, a better understanding of which perturbations leave the special states unharmed and those most effective at removing them could provide clues to better understand the origin of the phenomenon. In this section we will first consider some “physical” perturbations, which can be motivated as corrections to the model which are likely to appear in physical realisations. Furthermore, we discuss several deformations that bring the PXP model to previously studied exactly solvable points (49, 51, 98). We will demonstrate that these perturbations are destructive to the oscillations, which shows that the effects seen are not due to proximity to a previously studied integrable point.

4.5.1 Physical perturbations

In this section we will take a step back from the effective PXP model and use perturbation theory to first derive it and then corrections for finite interaction energy between adjacent Rydberg atoms. This will produce a number of local perturbations which are likely to form small corrections on any physical realisation. We will start however from a time-independent Hamiltonian that strictly speaking is already a highly simplified effective Hamiltonian for a complicated arrangement of lasers and other optical elements (19),

$$H = \sum_j \left(\frac{\Omega}{2} X_j - \Delta n_j \right) + \sum_{i,j} V_{i,j} Q_i Q_j, \quad (4.20)$$

where Ω is the Rabi frequency, Δ is a detuning for when the drive is off resonance and V is the van der Waals interaction energy. Rescale the Hamiltonian by a factor of $1/V$ and introduce a small parameter $\epsilon = \Omega/(2V)$. Now we have a Hamiltonian

$$H = H_0 + \epsilon H_1 = \sum_j Q_j Q_{j+1} + \epsilon \sum_j X_j. \quad (4.21)$$

The dominant term H_0 counts the number of adjacent excitations; accordingly its eigenvalues are the non-negative integers and is highly degenerate. The perturbation H_1 admits a simple interpretation as the trivial paramagnet; its eigenvalues are every other integer between $-N$ and $+N$ inclusive.

The tool we will use to resolve this degenerate perturbation theory problem and produce an effective Hamiltonian is the Schrieffer-Wolff transformation (26, 147). First we introduce the low-energy subspace \mathcal{P} corresponding to the zero eigenvalue subspace of H_0 , which is equivalent to a projector into that subspace

$$\mathcal{P} = \prod_j (\mathbb{1} - Q_j Q_{j+1}). \quad (4.22)$$

The complementary subspace is defined by $\mathcal{Q} = \mathbb{1} - \mathcal{P}$. The subspace \mathcal{P} is spanned by configurations with definite occupations where no two excitations are adjacent. Now the Schrieffer-Wolff effective Hamiltonian may be calculated perturbatively to first order as

$$H_{\text{SW}} = \epsilon H_0 \mathcal{P} + \mathcal{P} H_1 \mathcal{P} + \sum_{n>1} \epsilon^n H_{\text{SW}}^{(n)} = \epsilon \mathcal{P} \left(\sum_j P_{j-1} X_j P_{j+1} \right) \mathcal{P} + O(\epsilon^2), \quad (4.23)$$

for finite N . The leading term is our promised effective model for the limit $V \gg \Omega$. We will often simply write it as $H_{\text{eff}} = \sum_j P_{j-1} X_j P_{j+1}$ and implicitly project into \mathcal{P} as it is block diagonal. The purpose of H_0 is seen to produce a set of constraints, that no two excitations may be adjacent. The space of solutions to these constraints is \mathcal{P} — our constrained Hilbert space.

We might wonder what happens when the constraint energy scale V is made finite. Our first concern should be whether the perturbation series will converge. Standard results on the Schrieffer-Wolff transformation (26) show that the series will converge absolutely if

$$V \geq V_c = \frac{\Omega N}{8}. \quad (4.24)$$

The dependence on N is unfortunate for the thermodynamic limit, but for every finite size it shows there is a finite V sufficiently large that these corrections are perturbative. Increasing V (or decreasing Ω) appropriately as the thermodynamic limit is taken is surely less demanding than isolating a N -qubit system from the

4. PHENOMENOLOGY OF WEAK ERGODICITY BREAKING IN A CONSTRAINED QUANTUM SYSTEM

vagaries of its environment. Furthermore, this inequality might be too stringent, as this bound doesn't know anything about locality or any other structure of the system. It also is concerned with eigenstate or infinite-time properties whereas finite-time properties can be much better behaved (3).

If we are however curious as to the effects the perturbation might have, we ought to consider the second-order correction. First, let us introduce some notation. Define $\mathcal{O}(H_1)$ as the off-block part of H_1 , that contains the generated transitions between the low-energy subspace where no constraints are violated and the complementary high-energy subspace, and the propagator superoperator

$$\mathcal{L}(X) = \sum_{i,j} \frac{|i\rangle \langle i| X |j\rangle \langle j|}{E_i - E_j}, \quad (4.25)$$

where the energies and eigenvectors are of H_0 . The second-order correction can now be computed as

$$H_{\text{SW}}^{(2)} = b_1 \mathcal{P}[\mathcal{L}(\mathcal{O}(H_1)), \mathcal{O}(H_1)]\mathcal{P} \quad (4.26)$$

$$= b_1 \mathcal{P}H_1 \left(\mathcal{P}_{(1)} + \frac{1}{2}\mathcal{P}_{(2)} \right) H_1\mathcal{P} \quad (4.27)$$

where $\mathcal{P}_{(n)}$ is the eigenspace of H_0 with eigenvalue n . This is because the action H_1 on the low-energy subspace can only generate either one or two excitations of H_0 . From here simply substitute H_1 and perform some algebraic manipulations to arrive at

$$H_{\text{SW}}^{(2)} = -\mathcal{P} \sum_j \left(2Q_j - \frac{1}{2}Q_{j-1}Q_{j+1} + X_j X_{j+1} \right) \mathcal{P}, \quad (4.28)$$

assuming periodic boundary conditions.

To summarise, this perturbation can be used to simulate the effect of weakening the constraint energy scale V without resorting to calculation in the unconstrained Hilbert space. At second order, it consists of constrained hopping, next-nearest neighbour interaction between Rydberg excitations and a chemical potential. In addition, we will consider the following other local perturbations to

4.5 Effect of perturbations

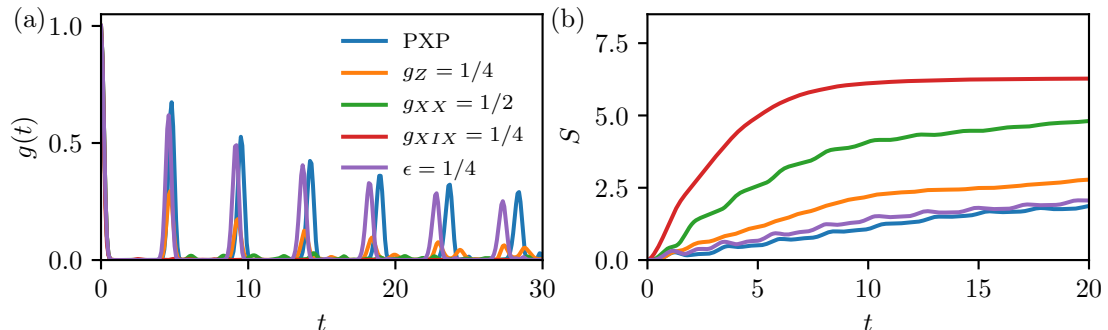


Figure 4.11: (a) Periodic quantum revivals are dampened by the influence of the perturbations. However, some are more effective than others. (b) Von Neumann entanglement entropy dynamics under the influence of perturbations for the midpoint bipartition. The perturbations are defined in Equations (4.28) and (4.29). The longer ranged XIX perturbation is most effective at promoting the generation of entanglement and damping oscillations from the signal. The shorter ranged perturbations, including the perturbation designed to mimic finite interaction energy, tend to affect the dynamics less strongly. The line labelled by ϵ is the second order perturbation theory in $\epsilon = \Omega/(2V)$. Coupling constants were chosen to make the operator norm of the perturbations approximately equal. Calculations are for a periodic system of $N = 28$ sites.

the PXP Hamiltonian,

$$\delta H_Z = g_Z \sum_j Z_j, \quad (4.29a)$$

$$\delta H_{XX} = g_{XX} \sum_j \mathcal{P} X_j X_{j+1} \mathcal{P}, \quad (4.29b)$$

$$\delta H_{XIX} = g_{XIX} \sum_j \mathcal{P} X_j X_{j+2} \mathcal{P}. \quad (4.29c)$$

These can be given physical interpretations: H_Z is a uniform chemical potential and H_{XX} and H_{XIX} are hopping processes subject to the constraint. These form part of the second order correction $H_{\text{SW}}^{(2)}$ to finite interaction energy, but are likely to be generated by any other imperfections in the system. We note that these perturbations lift the zero-energy degeneracy, as they commute with both the spectral reflection symmetry and spatial inversion (145, 167, 168).

In Figure 4.11 we show the effect of these perturbations on the unusual dynam-

4. PHENOMENOLOGY OF WEAK ERGODICITY BREAKING IN A CONSTRAINED QUANTUM SYSTEM

ics of our system following a quench from the \mathbb{Z}_2 state. The perturbations from Equations (4.28) and (4.29) are used with coupling constants chosen to give them all approximately equal operator norms. These are by no means small perturbations, especially considering the exponentially small many-body level spacing in the $N = 28$ site periodic system. The addition of the longer range terms XX and XIX are best at increasing the rate of entropy production, consistent with how we expect terms like these to increase the speed at which information travels in the system. Surprisingly the addition of the XX and $H_{SW}^{(2)}$ perturbations have little effect on the oscillations in the entropy, whereas Z dampens them and XIX essentially erases them. This doesn't translate immediately into the fidelity dynamics where there are no revivals with XX despite oscillations in the entropy. The fidelity dynamics with the XX perturbation decays rapidly and equally there are no special eigenstates, but when combined into $H_{SW}^{(2)}$ the perturbation is much better tolerated. For the XIX perturbation, it might be that the extent of the term makes the constraint less important. It is of particular relevance that the $H_{SW}^{(2)}$ perturbation, even though with a coupling beyond the range at which the series converges, does not affect the findings significantly, something that is related to prethermalisation (1, 47).

Moreover, in Figure 4.12 these differences also play out in the off-diagonal matrix elements of a local Z observable. In Figure 4.12 (a), the XIX perturbation broadens and shifts the anomalous peak and other features seen before in Figure 4.9, which appeared at harmonics of the oscillation frequency, analogous to the erasure of oscillations in the entropy dynamics. In Figure 4.12 (b), we show the envelope function with frequency rescaled by the many-body level spacing Δ . Only with the XIX perturbation does a Thouless plateau appear, extending up to around 10 times Δ , indicating a regime of very small energy fluctuations where random matrix theory predictions are in operation. Other predictions of ETH are similarly restored, such as the inverse square-root scaling in diagonal matrix element fluctuations. As was found in the entropy dynamics the other perturbations affect the results much less significantly and no Thouless plateau is observed even around $\omega \approx \Delta$. The XX perturbation, which retains entropy oscillations while removing fidelity oscillations, is among those with no Thouless plateau.

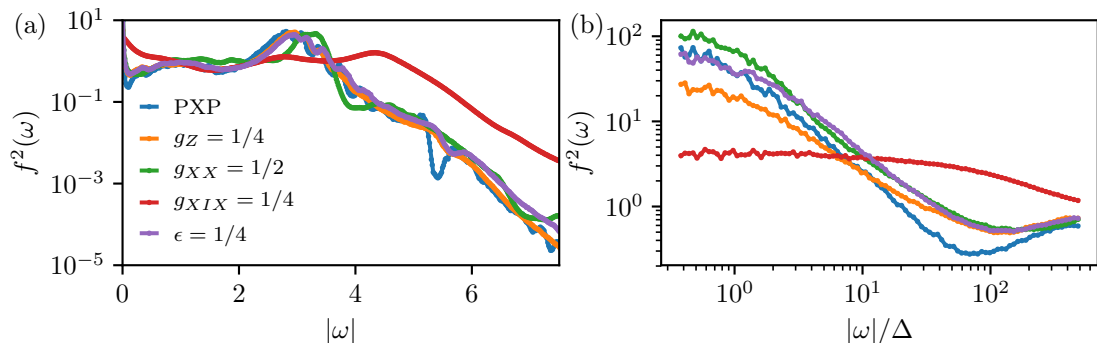


Figure 4.12: Local Z observable off-diagonal matrix elements under the influence of perturbations. See Equation (4.19). (a) Envelope function $f^2(E, \omega)$ integrated over energy as a function of ω for the shorter-range perturbations retains the anomalous peak. The longer-range XIX perturbation broadens and shifts this peak and washes out many of the other features. (b) With the frequency rescaled by the mean many-body level spacing Δ , the XIX perturbation leads to the emergence of a Thouless plateau. In contrast the other perturbations, even though they are not small, are not effective at restoring ETH predictions. In particular the effect of the perturbation designed to mimic finite interaction energy doesn't strongly effect the behaviour.

Thus, we conclude that what we have seen so far is not isolated to a finely tuned point, and local perturbations, even those that are in no sense small, do not necessarily destroy or remove the non-equilibrium phenomena. There are however other perturbations, such as XIX , which are much more effective at restoring conventional thermalisation whilst still respecting the constraints. As in the unperturbed case, the non-equilibrium dynamics can lead to a small number of atypical eigenstates but also affects the full spectrum of eigenstates as can be seen in deviations from ETH predictions. This contrasts with the behaviour expected around integrable points where almost all perturbations lift integrability and restore eigenstate thermalisation with exponential sensitivity due to the many-body density of states.

4.5.2 Integrable deformations

After showing physically motivated perturbations tend to restore thermalisation, I turn now to discuss related models that have been more deliberately constructed.

4. PHENOMENOLOGY OF WEAK ERGODICITY BREAKING IN A CONSTRAINED QUANTUM SYSTEM

There are a number of special models which might live on an extended parameter space that includes the PXP model. A one-parameter family of integrable models considered by Ref. (51), which features the so-called “golden chain” model of Fibonacci anyons (49), a quantum group version of the Heisenberg XXX chain. In addition, there is a one-parameter family of frustration-free Hamiltonians formed from the PXP Hamiltonian, plus a number of terms diagonal in the product state basis (98).

The integrable models of Ref. (51) can be obtained by adding the term,

$$\delta H_v = - \sum_j \mathcal{P} [v Q_{j-1} Q_{j+1} + (v^{-1} - v) Q_j] \mathcal{P} \quad (4.30)$$

with one free real parameter v . This can be solved using the Bethe-ansatz (51). The integrable line features a quantum tricritical and a quantum critical point at $v = \pm((\sqrt{5} + 1)/2)^{5/2}$, respectively (51, 140). This perturbation is never small for any value of v . On this line, the special eigenstates from PXP are strongly perturbed, have large energy variances and the decay of oscillations following a \mathbb{Z}_2 quench is much faster. Moreover we did not observe low-entanglement eigenstates in the middle of the spectrum, unlike in the unperturbed model, see Figure 4.10.

The frustration-free model of Ref. (98) is found by adding a term,

$$\delta H_z = \sum_j (z P_{j-1} P_j P_{j+1} + z^{-1} P_{j-1} Q_j P_{j+1}), \quad (4.31)$$

which allows for the exact solution of its ground state for any $z \in \mathbb{R}$ with an exact matrix product state (MPS) representation (98). Again, this perturbation is never small for any value of z . Variational approximations to the PXP ground state can be formed using the same MPS Ansatz (79, 168). This successfully reproduces local observables, such as the energy density, to high precision. As was the case for the integrable model, we find that there are no analogous low entropy states and the special eigenstates from PXP are not stable to the action of the perturbed Hamiltonian. Following a \mathbb{Z}_2 quench, we find that the fidelity oscillations always decay much faster.

In summary, we observed that deforming the PXP model towards nearby solvable points does not improve the robustness of the special eigenstates. In-

stead, such deformations lead to their complete disappearance. This suggests that despite the existence of extended parameter spaces featuring several integrable points, these do not explain for the phenomena observed in the model without these perturbations.

4.6 Conclusions

We have demonstrated that the PXP model displays an unconventional form of ergodicity breaking where the dynamical approach to equilibrium is strongly dependent on the initial condition. This stands in contrast to more familiar ergodicity breaking in quantum systems which is all-or-nothing. Most dramatically this is seen in the fidelity which undergoes periodic quantum revival following a quench from the Néel state, which is related to the presence of a number of special eigenstates with anomalous support on the initial state. The consequent oscillatory behaviour in many local observables gives this physical relevance and has been observed in a recent experiment (19). This is also present in the dynamics of local observables and entanglement entropy.

Alongside these dynamical properties are those associated with the eigenstates. In particular, the special states form violations of conventional eigenstate thermalisation by exhibiting atypical matrix elements of local observables. Furthermore, in the remainder of the eigenstates there are signs of anomalous thermalisation. The absence of a Thouless plateau in the envelope function, along with the parametrically slower decay of fluctuations in the diagonal matrix elements, stands against the detailed predictions of the eigenstate thermalisation hypothesis.

Careful statements of the ETH however will only make claims about the thermodynamic limit. We would suggest that for the PXP model, or similar systems that are not integrable or disordered, the methods available do not allow one to speak definitively about thermodynamic limit. For any computing capability there exists a size that cannot be reasonably calculated. For that, and subsequent sizes, conventional thermalisation cannot be excluded, but this is actually independent of whether the hypothesis is true or otherwise. Definitive answers to these questions might be provided by identifying further algebraic structure

4. PHENOMENOLOGY OF WEAK ERGODICITY BREAKING IN A CONSTRAINED QUANTUM SYSTEM

within the model, but there are no guarantees that this exists. Indeed, in the largest size systems for which we can do calculations there appear features suggestive of an eventual return to conventional thermalisation. This would be similar to integrability which is highly sensitive to perturbation, where any finite non-integrable perturbation restores thermalisation at some long time scale and large system size. The behaviour before that eventual return to thermalisation is referred to as prethermalisation (22). A corollary to this similarity would be that with some perturbation to the PXP model we might find a model which idealises the phenomena seen here, and stabilises it to arbitrarily long times and large sizes. This is a thread that we will pick up in a later chapter.

Chapter 5

Forward-scattering approximation and quantum scars

In the previous chapter we saw that the quantum revival observed in experiments is underlined by the presence of a vanishingly small fraction of eigenstates with anomalously large overlap with the initial state. The most significant contributions arose from states forming a highest overlap band with approximately evenly spaced eigenvalues. Further, these special states had anomalous participation ratios and much reduced entropy in comparison to typical states at their energy densities. In this chapter we will seek to explain these findings using a technique we call a forward-scattering approximation, that we introduced in Ref. (167, 168). Within this approximation we find approximations to the eigenpairs forming the highest overlap band with the Néel state, producing explanations of the revivals and the other anomalous properties of these special states. Complete solution of the PXP model is likely impossible, whereas calculations within this approximation can be done efficiently in a number of different ways. We will show in detail how calculations can be performed by linear recurrences and transfer matrices, and briefly mention those using matrix-product states (MPS).

The PXP Hamiltonian can be viewed as the adjacency matrix of a graph where vertices are in correspondence with basis configurations and an edge is

5. FORWARD-SCATTERING APPROXIMATION AND QUANTUM SCARS

present if the Hamiltonian generates a transition between those two states as all the matrix elements of the Hamiltonian in this basis are either zero or one. For open boundary conditions this forms a family of graphs (indexed by N) known as the Fibonacci cubes, or for periodic boundaries the Lucas cubes. An example of the Lucas cube of dimension 6 is shown in Figure 5.1 with vertices labelled by the configuration of a periodic system of 6 sites.

The Fibonacci and Lucas cubes share many properties with the simpler hypercube graphs (92). The hypercube graphs correspond to the trivial paramagnet Hamiltonian, $H = \sum_j X_j$, which has a trivial oscillatory dynamics for any initial product state. These graphs have a number of intriguing graph theoretic properties; they are isometric subgraphs of hypercubes and median graphs (91), which means that for any triple of vertices there is a unique median vertex that belongs to some shortest path between any pair of vertices from that triple. This imprecise notion of similarity is inspiration for their application in network topologies as alternatives to hypercube networks (39, 76, 92). In the same manner we will model the PXP Hamiltonian as a deformed version of the trivial paramagnet.

5.1 Forward-scattering approximation

In this section we will develop a method of constructing approximations to those special eigenstates most important for describing the behaviour of the Néel state. The basic idea follows the Lanczos recurrence (96) which builds an orthonormal basis of Lanczos vectors for the Krylov subspace generated by the acting Hamiltonian on an initial state. This method is often used as an algorithm to find eigenstates and to compute the action of the matrix exponential such as for time evolution. The additional ingredient is an approximation, that in a certain way the PXP Hamiltonian acts similarly to the trivial paramagnet Hamiltonian.

We will start by carrying through the Lanczos tridiagonalisation on the N -dimensional hypercube graph. The Lanczos recurrence recursively constructs the sequence of Lanczos vectors using the matrix action,

$$\beta_{j+1} |v_{j+1}\rangle = H |v_j\rangle - \alpha |v_j\rangle - \beta_j |v_{j-1}\rangle, \quad (5.1)$$

5.1 Forward-scattering approximation

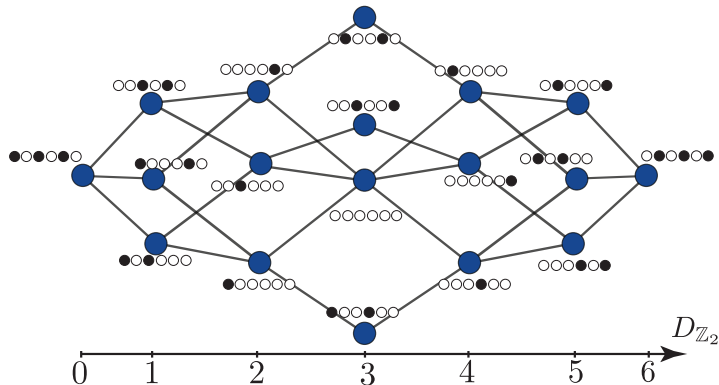


Figure 5.1: Illustration of a Lucas cube graph. The vertices are labelled with the allowed configurations for the periodic chain of 6 sites. Edges are present whenever the Hamiltonian generates transitions between the two corresponding configurations. The vertices are arranged horizontally according to the Hamming distance $D_{\mathbb{Z}_2}$ from the Néel state indicated on the axis below. The forward-propagating part of the Hamiltonian moves to the right, incrementing $D_{\mathbb{Z}_2}$, whereas the backward-propagating term moves one to the left.

where the coefficients α_j and β_j are chosen to ensure that the vectors are normalised and mutually orthogonal. Take as an initial vector $|v_0\rangle = |0\rangle = |\circ\circ\circ\circ\cdots\rangle$, the polarised state and begin to form the sequence of Lanczos vectors. Taking the first matrix-vector product, $A|0\rangle$, we produce a state which is a superposition of all states with a single spin flip. The hypercube graph has the symmetric group S_N for its an automorphism group, which in the many-body picture corresponds to taking permutations of the spins. This symmetry forces all of the vector components for the single spin flips to be equal.

Taking a second product for $A^2|0\rangle$ we produce a state which is a superposition of all states reached by two spin flips. Some of these paths go back on themselves whereas the majority feature spin flips on two distinct sites. Those that go back on themselves produce the initial vector $|0\rangle$ and this component of the state will be removed when orthogonalising against the previous Lanczos vectors. Within the component with two distinct flips, the same automorphism group as before ensures all the probability amplitudes are equal because any two disjoint spin flips are equivalent according to the symmetric group action.

From here we proceed inductively. First, we classify the product state basis

5. FORWARD-SCATTERING APPROXIMATION AND QUANTUM SCARS

vectors according to the minimum number of spin flips that connects them with the initial state. This is their Hamming distance from the initial state. For presentational simplicity, take a splitting of the N -dimensional hypercube adjacency matrix A into two parts

$$A^+ = \sum_j X_j Q_j, \quad A^- = \sum_j X_j P_j, \quad (5.2)$$

the former of which always increases the Hamming distance from the polarised state $|0\rangle$ and the latter always decreases this. Suppose that for some n , the j -th element (starting from zero) for any $j < n$ in the sequence of Lanczos vectors is the equal-weight positive superposition of all basis states with j flips from the initial polarised state $|0\rangle$:

$$|v_j\rangle = \binom{N}{j}^{-\frac{1}{2}} \sum_{\substack{S \subseteq [N] \\ |S|=j}} X_S |0\rangle, \quad (5.3)$$

where $[N]$ is set of natural numbers up to N . We now calculate the backward scattering part:

$$A^- v_{n-1} = \binom{N}{n-1}^{-\frac{1}{2}} \sum_{\substack{S \subseteq [N] \\ |S|=n-1}} \sum_{j \in S} X_{S \setminus j} |0\rangle \quad (5.4)$$

$$= \binom{N}{n-1}^{-\frac{1}{2}} (N-n+2) \sum_{\substack{S' \subseteq [N] \\ |S'|=n-2}} X_{S'} |0\rangle \quad (5.5)$$

$$= \sqrt{(n-1)(N-n)} v_{n-2}, \quad (5.6)$$

and find it proportional to the previous Lanczos vector. The orthogonalisation will remove this component from the next Lanczos vector.

5.1 Forward-scattering approximation

Correspondingly, the forward scattering part,

$$A^+ |v_{n-1}\rangle = \binom{N}{n-1}^{-\frac{1}{2}} \sum_{\substack{S \subseteq [N] \\ : |S|=n-1}} \sum_{j \notin S} X_{S \sqcup j} |0\rangle \quad (5.7)$$

$$= \binom{N}{n-1}^{-\frac{1}{2}} n \sum_{\substack{S' \subseteq [N] \\ : |S|=n}} X_{S'} |0\rangle \quad (5.8)$$

$$= \sqrt{n(N-n+1)} |v_n\rangle \quad (5.9)$$

is found to be proportional to $|v_n\rangle$, which extends the domain of validity of Equation (5.3) to $j = n$ completing the inductive step. By induction, we then have that Equation (5.3) is valid for all $j \geq 0$.

The off-diagonal elements for the tridiagonal matrix produced by these Lanczos iterations are seen to be

$$\beta_j = \sqrt{j(N-j+1)}. \quad (5.10)$$

The diagonal elements all vanish because the hypercube is a bipartite graph. An unusual feature of these iterations is that the process terminates after N iterations which is signalled by the Lanczos vector $|v_{N+1}\rangle$ being the zero vector. This produces an invariant Krylov subspace of dimension $N + 1$. Diagonalising the adjacency matrix in this subspace will produce exact eigenpairs.

We now turn to the the problem of the PXP Hamiltonian. Once again take a splitting of the Hamiltonian $H = H^+ + H^-$ into forward and backwards propagating parts:

$$H^+ = \sum_{x \text{ even}} P_{x-1} P_{x+1} X_x Q_x + \sum_{x \text{ odd}} P_{x-1} P_{x+1} X_x P_x, \quad (5.11)$$

$$H^- = \sum_{x \text{ even}} P_{x-1} P_{x+1} X_x P_x + \sum_{x \text{ odd}} P_{x-1} P_{x+1} X_x Q_x, \quad (5.12)$$

the former of which always increases the Hamming distance from the Néel state and the latter always decreases this. See the diagram in Figure 5.1. Substituting

5. FORWARD-SCATTERING APPROXIMATION AND QUANTUM SCARS

this splitting into the Lanczos recurrence yields

$$|w_j\rangle = \beta_j |v_j\rangle = H |v_{j-1}\rangle - \alpha_{j-1} |v_{j-1}\rangle - \beta_{j-1} |v_{j-2}\rangle, \quad (5.13)$$

$$= H^+ |v_{j-1}\rangle - \alpha_{j-1} |v_{j-1}\rangle + (H^- |v_{j-1}\rangle - \beta_{j+1} |v_{j+2}\rangle). \quad (5.14)$$

Now we make the assumption that the final term

$$|\delta w_j\rangle = H^- |v_{j-1}\rangle - \beta_{j-1} |v_{j-2}\rangle, \quad (5.15)$$

is unimportant and can be safely ignored. This step cannot be rigorously justified, but later in Section 5.2 we will quantify these errors. Fairly accurate results can be obtained for either local observables or short times. Even for non-local quantities such as the return probability good estimates of the revival frequency can be obtained. It can also be viewed as a heuristic coming from the graph structure. Around each vertex of a Fibonacci or Lucas cube the connectivity in its neighbourhood is similar to a hypercube with a dimension between $N/2$ and N . The similarity of Fibonacci cubes to hypercubes has motivated a great deal of work on their structure (92). Together with the fact that H is bipartite and thus $\alpha_j = 0$, we arrive at

$$\beta_j |v_j\rangle = H^+ |v_{j-1}\rangle, \quad (5.16)$$

which is our forward-scattering Lanczos recurrence. The vectors $|v_j\rangle$ of this sequence starting from $|v_0\rangle = |\mathbb{Z}_2\rangle$ form an orthonormal subspace because each is in a different Hamming distance sector. Accordingly there are $N + 1$ elements in the sequence because it is not possible to be more than N spin flips away from any state. After this number of steps the recurrence closes, producing the zero vector. It turns out that the coefficients β_j can be calculated by a number of efficient means, and these will be the subject of several subsequent sections.

Diagonalising the tridiagonal matrix generated produces Ritz estimates for eigenvalues and eigenvectors of H . These forward-scattering Ritz values and overlaps with the Néel state are shown in Figure 5.2 (a) and compared with the numerically exact eigenvalue decomposition for system size $N = 32$. In this forward-scattering subspace we get good approximations to the special states of the highest-overlap band which underlie the phenomena observed in experiment.

5.1 Forward-scattering approximation

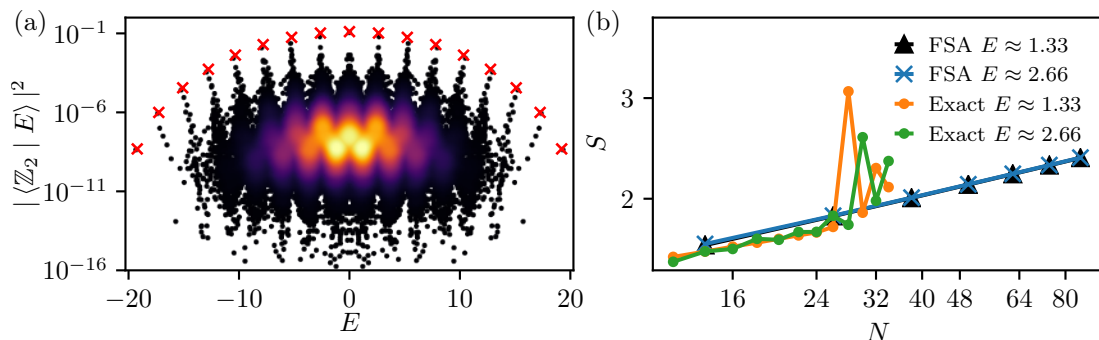


Figure 5.2: Comparison between the forward-scattering approximation and the numerically exact eigenvalue decomposition. (a) Scatter plot of energy against overlap with \mathbb{Z}_2 for the forward-scattering approximation (crosses) and the numerically exact eigenvalue decomposition. Data is for system size $N = 32$ in the zero-momentum, inversion-even sector. (b) Scaling of bipartite entanglement entropy with system size for both special eigenstates and their approximations with the forward-scattering analysis.

In Figure 5.2 (b), we show the scaling of the bipartite entanglement entropy for the special eigenstates and their forward-scattering approximations. The exact eigenstates were found with a shift-invert Lanczos algorithm. The entropy of the ground state and some low-lying excited states follows an area law, as expected for a gapped system. The entropy of the special states, with the exception of the exact eigenstates for the largest sizes, grows as a logarithm of system size. This is surprising as logarithmic scaling of entropy is normally found in critical-point ground states (29, 171), and typically highly excited states follow an extensive volume law scaling. Intriguingly, parallel developments in the AKLT model have found rare highly-excited yet non-thermal states also with logarithmic entanglement entropy (116). We interpret the erratic behaviour, see Figure 5.2 (b), in the largest sizes as an indicator that the atypical states are unstable with system size and will become thermal for sizes that are not numerically accessible. The non-equilibrium properties seen will be retained however for some finite time. The lack of proper thermalisation at these very large sizes suggests that the model for small sizes is perturbatively close to another model in which the properties observed are retained in the thermodynamic limit. This is something we will explore in the next chapter.

5. FORWARD-SCATTERING APPROXIMATION AND QUANTUM SCARS

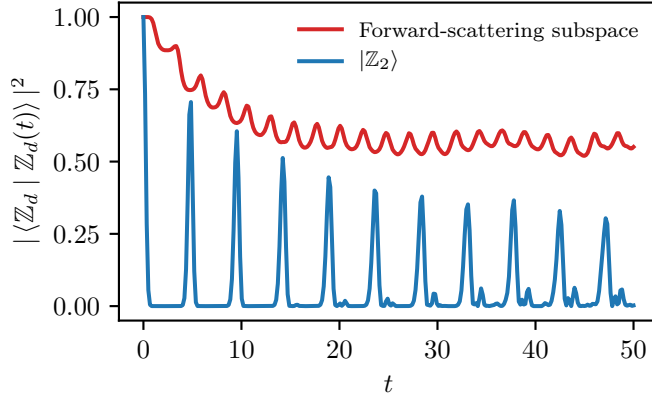


Figure 5.3: Time series of quantum revival probability to the Néel state and probability to be found within the forward-scattering subspace for system size $N = 32$. The latter is measured by the expectation value of the projector into the subspace \mathcal{K} .

The logarithmic growth in entropy also indicates that the Lanczos vectors $|v_j\rangle$ can be approximated by matrix product states (MPS) with polynomial time and space complexity in N and j . This suggests an algorithm where a matrix product operator (MPO) representation for H^+ is applied to each Lanczos vector and then compressed to a lower bond dimension MPS in the same way as in the time evolving block decimation (TEBD) or DMRG algorithms. Indeed this is what was done to calculate the entropies for system sizes up to 80 sites (168).

In Figure 5.3 the red curve tracks the probability that the system is within the forward-scattering subspace over time. That this changes over time indicates that the subspace is not exactly H -invariant and that some probability “leaks out” of it. The subspace probability is non-monotonic with peaks that coincide with returns to the initial $|\mathbb{Z}_2\rangle$ state or the translated state $|\circ\bullet\bullet\bullet\rangle$, which appears as frequency doubling with respect to the return probability curve in blue. The gap between the revival probability and the subspace probability shows the effect of dephasing within the forward-scattering subspace. Algebraically, this means that the algebra generated by H^+ and H^- is not closed like a ladder algebra, and is deformed away from that of $\mathfrak{su}(2)$. This algebraic perspective will be taken up in Chapter 6, where we attempt to remove the deformation.

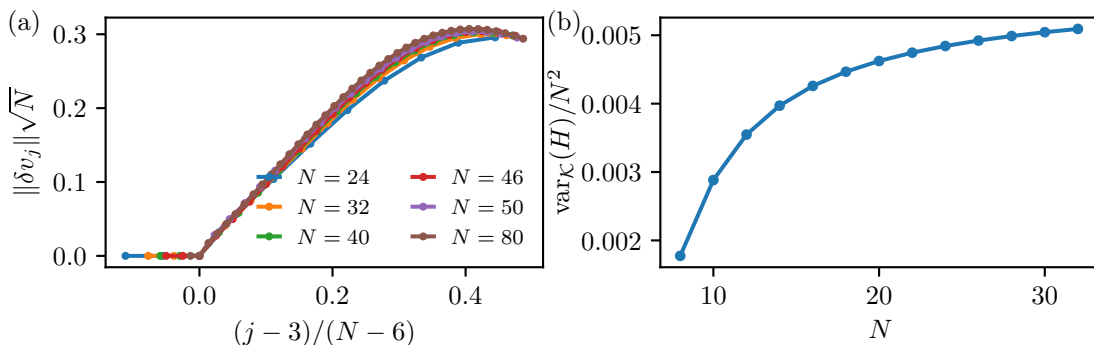


Figure 5.4: Error quantities in the forward-scattering analysis. (a) Forward-scattering step errors $\|v_j\|$ against step index j for a range of system sizes. Axes are rescaled to achieve a good scaling collapse showing that $\|v_j\| = O(\sqrt{N})$ for fixed j/N . (b) Subspace variance against system size N . Scaling shows that $\text{var}_{\mathcal{X}}(H) = O(N^2)$.

5.2 Error analysis

In this section we will calculate the errors incurred in individual steps of the forward-scattering approximation and measure errors in the entire procedure through a quantity we call the subspace variance. First, the error made in a single Lanczos iteration is the difference between the backward-scattered part and the β term in the Lanczos recurrence it is approximated as cancelling, i.e.,

$$|\delta w_j\rangle = H^- |v_{j-1}\rangle - \beta_{j-1} |v_{j-2}\rangle. \quad (5.17)$$

More important will be the error vector $|\delta v_j\rangle$, defined as $\beta_j |\delta v_j\rangle = |\delta w_j\rangle$, which is the relative error in the Lanczos vector $|v_j\rangle$. After a little manipulation the squared-norm of the error vector can be brought to the following form

$$\|\delta w_j\|^2 = \langle v_{j-1} | [H^+, H^-] | v_{j-1} \rangle + \beta_j^2 - \beta_{j-1}^2 \quad (5.18)$$

in terms of the commutator $[H^+, H^-]$, which turns out to be remarkably simple. In Figure 5.4 we see that $\|\delta w_j\|^2$ is at most $O(N)$ as to be expected from Equation (5.18).

For a second measure of the accuracy of the forward-scattering approximation we will examine the energy fluctuations for states in the forward-scattering

since $(H^+)^2$ is traceless. This gives

$$\text{tr}\{\mathcal{K}H^-H^+\} = \sum_{j=0}^N \langle v_j | H^-H^+ | v_j \rangle = \sum_{j=0}^N \beta_{j+1}^2 \langle v_{j+1} | v_{j+1} \rangle = \sum_{j=1}^N \beta_j^2. \quad (5.26)$$

Putting this together we have that

$$\text{var}_{\mathcal{X}}(H) = \text{tr}\{\mathcal{K}[H^+, H^-]\}. \quad (5.27)$$

Incidentally,

$$\text{var}_{\mathcal{X}}(H) = \sum_j \|\delta w_j\|^2, \quad (5.28)$$

showing that these two measures of error are related to one another. This is all consistent with $\text{var}_{\mathcal{X}}(H)$ being at most $O(N^2)$, as shown in Figure 5.4 (b). This does not affect the short time behaviour of local observables since these can be produced with a fixed size system according to the Lieb-Robinson bound; these can be modelled with a system size independent error. Long range observables however, such as return probability, have no such protection. As their range increases the quality of the approximation will generically decrease.

5.3 Linear recurrence system

The recurrence defining the forward-scattering approximation, that we introduced in Section 5.1, is

$$\beta_j |v_j\rangle = A^+ |v_{j-1}\rangle. \quad (5.29)$$

Calculating the off-diagonal matrix elements directly from this formula is inefficient due to the exponential growth in the dimension of the connected subspace of the PXP model, and for this reason we seek more efficient methods. First, in Eq. (5.30), it will be shown that β coefficients are determined by the number of loops reaching a given distance from the initial state. Recursive expressions for these loop countings will then be derived for open boundary conditions, yielding as main results Eqs. (5.36), (5.37) and (5.38). Analogous expressions for periodic boundary conditions are given in Eqs. (5.44), (5.45) and (5.47). These results

5. FORWARD-SCATTERING APPROXIMATION AND QUANTUM SCARS

allow for the exact computation of Hamiltonian matrix elements, commutators of H^+ and H^- and some simple local observables using dynamic programming techniques. The complexity is polynomial in the system size and in the more complicated case of periodic boundaries large systems with size of the order of hundreds of sites are practical.

By repeated substitution of Equation (5.29) into itself we reach

$$\begin{aligned}\beta_j^2 &= \langle v_{j-1} | H^- H^+ | v_{j-1} \rangle \\ &= \frac{\langle v_0 | (H^-)^j (H^+)^j | v_0 \rangle}{\prod_{k=1}^{j-1} \beta_k^2} \\ &= \frac{\langle v_0 | (H^-)^j (H^+)^j | v_0 \rangle}{\langle v_0 | (H^-)^{j-1} (H^+)^{j-1} | v_0 \rangle}.\end{aligned}\tag{5.30}$$

From this we recognise the amplitude

$$W_{N,j} = \langle v_0 | (H^-)^j (H^+)^j | v_0 \rangle\tag{5.31}$$

as the number of shortest closed paths reaching a distance of j from the initial \mathbb{Z}_2 configuration. The first subscript indicates the system size N . In terms of these numbers the off-diagonal elements are

$$\beta_j = \sqrt{\frac{W_{N,j}}{W_{N,j-1}}}.\tag{5.32}$$

Our goal here is to derive a linear recurrence system for calculating $W_{N,j}$ and our strategy will be to count loops recursively in terms of loops on smaller subsystems. We will first present results for open boundary conditions before moving on to the more complicated case of periodic boundaries.

5.3.1 Loop counting for open chains

Consider a loop of valid spin flips on the open system on N sites. This loop can be projected into two subsystems where each flip is assigned to the subsystem in which the spin in flips is located. We will choose the two subsystems to comprise of the two leftmost spins and the remaining $N - 2$ sites of the system.

5.3 Linear recurrence system

These subsystem loops are valid loops on the corresponding open systems of 2 and $N - 2$ sites. The original loop is one of the ways in which the spin flips of the subsystem loops can be interlaced such that the constraints are never violated. Given a pair of loops on the two subsystems we only need to know when the left-most spin of the right subsystem and the right-most spin of the left subsystem are flipped, if at all, in order to count the ways in which they can be interlaced. Because the loops discussed are properly shortest loops, these boundary spins are either flipped once moving away from the Néel state and once again on the return journey, or not at all. This key simplification comes from the forward-scattering assumption; without it there would be exponentially many boundary configurations. Evaluating $\langle 0 | (H^+)^j | 0 \rangle$ is equivalent to contracting a 2D tensor network, where one dimension is a discrete “imaginary time” for each application of H , the entropy of the network cut along the imaginary time dimension is $O(j)$, following an area law. This cannot be evaluated both exactly and efficiently (122). With the forward-scattering assumption only logarithmic boundary entropy is produced along the “imaginary time” direction which allows for efficient and exact evaluation. This will be reflected in the boundary vectors that are the partial contraction of the tensor network (which will be called $f_{N,j}$, $l_{N,j}$ etc.), only growing in dimension polynomially with j or N .

The most general shortest loop looks like a word

$$\underbrace{A \cdots AL \underbrace{A \cdots AR A \cdots A}_{a}}_j \mid \underbrace{A \cdots A}_{b} \underbrace{LA \cdots A RA \cdots A}_j, \quad (5.33)$$

where the symbol A stands-in for any spin flip (and each instance is different) of a bulk spin, L represents flipping the leftmost spin and R the rightmost spin. The symbols appear in the order which the represented moves occur in the loop, the vertical line separates the forward and backward steps in the loop and the braces are counting the number of symbols that appear in a certain portion of the word terminated by the appearance of an L or R symbol. The order in which the L and R flips appear, if at all, in the forward and backward half-words is not constrained, Equation (5.33) represents only one possible ordering.

5. FORWARD-SCATTERING APPROXIMATION AND QUANTUM SCARS

We will start by considering only the case of open boundaries. Let \mathcal{F} be the combinatorial class of forward-scattering loops on a system with open boundaries where the left-most spin remains fixed throughout the process. This class is graded by the size of the system N and the number of forward and backward transitions j . Similarly, let \mathcal{L} be the class where the left-most spin is flipped at some point of the process and is additionally graded by a and b . The index a specifies the number of forward steps which follow the flip of the leftmost spin, b is the number of backward steps preceding the return flip of the leftmost spin. These classes are defined recursively from the following equations,

$$\mathcal{F} = \begin{array}{c} \bullet \circ \\ \bullet \circ \end{array} * (\mathcal{F} + \mathcal{L}), \quad (5.34)$$

$$\mathcal{L} = \begin{array}{c} \bullet \circ \\ \circ \circ \\ \bullet \circ \end{array} * (\mathcal{F} + \mathcal{L}) + \begin{array}{c} \bullet \circ \\ \circ \circ \\ \bullet \circ \\ \bullet \circ \\ \bullet \circ \end{array} * \mathcal{L}, \quad (5.35)$$

where the $*$ operation glues together two collections of loops by producing the collection of all possible interlacings where the right boundary of the left operand has been joined to the left boundary of the right operand that satisfy the Fibonacci constraint. The loop diagrams are showing successive configurations along a loop in the vertical direction and the horizontal line separates the forward and backward steps.

These equations can be made explicit by introducing the counting sequences for the classes. Let $f_{N,j}$ be the number of shortest loops on the open chain of N sites reaching a Hamming distance of j from the Néel state where the leftmost spin is invariant, and let $l_{N,j}^{a,b}$ count those loops where the leftmost spin is flipped. These are the counting sequences for \mathcal{F} and \mathcal{L} , respectively. The previous equations then become,

$$f_{N,j} = f_{N-2,j} + \sum_{a',b'} l_{N-2,j}^{a',b'}, \quad (5.36)$$

$$l_{N,j}^{a,b} = f_{N,j-1} + \sum_{a',b'} L^{a,a'} l_{N-2,j-2}^{a',b'} L^{b,b'}, \quad (5.37)$$

where $L^{a,a'} = \min(a, a' + 1)$. Equation (5.36) captures the idea that we may

5.3 Linear recurrence system

glue two additional sites and the loop of doing nothing onto any loop on the reduced system. The first term in Equation (5.37) captures the idea that we can also glue a loop in which only the leftmost site transitions onto any loop on the reduced system. The second term counts the ways that that loops where both of the additional sites transition can be joined, while respecting the constraint that crosses the boundary on which they are joined. The right site in the left-subsystem can only be excited after the leftmost site of the right-subsystem has its excitation removed. Finally, the class of all loops in $\mathcal{F} + \mathcal{L}$ and can be counted by

$$W_{N,j} = f_{N+2,j}, \quad (5.38)$$

because for every loop on N sites we may glue the trivial loop on two-sites onto its left boundary to get a distinct loop on $N + 2$ sites, and for every loop on $N + 2$ sites where the leftmost two-sites never transition we may cut off the leftmost two sites to get a distinct loop on N sites.

Let us illustrate how the recurrence works on an example with $N = 4$ site open chain. Directly from Eq. (5.31), it is easy to show that the number of loops for different j sectors is given by $W_{4,1} = 2$, $W_{4,2} = 5$, $W_{4,3} = 13$, and $W_{4,4} = 25$. Using the recurrence, we can obtain these values starting from a smaller $N = 2$ site chain. In that case, the admissible j are given by 0, 1 and 2, and the only non-zero coefficients are $f_{2,0} = l_{2,1}^{0,0} = l_{2,2}^{1,1} = 1$. Then, applying Eqs. (5.38), (5.36), and (5.37), we have

$$\begin{aligned} W_{4,1} &= f_{6,1} = f_{4,1} + \sum_{a,b=0} l_{4,1}^{a,b}, \\ f_{4,1} &= \sum_{a',b'} l_{2,1}^{a',b'} = 1, \\ l_{4,1}^{a,b} &= f_{4,0} = 1, \end{aligned} \quad (5.39)$$

thus we get $W_{4,1} = 1 + 1 = 2$. Analogous calculation gives $W_{4,2} = 5$. For $W_{4,3}$ we

5. FORWARD-SCATTERING APPROXIMATION AND QUANTUM SCARS

need to include the L tensors. We have

$$\begin{aligned}
 W_{4,3} &= f_{6,3} = f_{4,3} + \sum_{a,b=0}^2 l_{4,3}^{a,b}, \\
 f_{4,3} &= 0, \\
 l_{4,3}^{a,b} &= f_{4,2} + \sum_{a',b'} L^{a,a'} L^{b,b'} l_{2,1}^{a',b'} = 1 + L^{a,0} L^{b,0}.
 \end{aligned} \tag{5.40}$$

Therefore, we obtain

$$W_{4,3} = \sum_{a,b=0}^2 (1 + \min(a, 1) \min(b, 1)) = 9 + 4 = 13, \tag{5.41}$$

as anticipated. Repeating this procedure and using Eq. (5.30), we can obtain the set of $N + 1$ coefficients β_j that form the tridiagonal matrix in the forward-scattering approximation.

5.3.2 Loop counting on periodic chains

Turning now to periodic boundaries, we must keep track of what happens at the subsystem right boundary in order to retain the information required to ensure the constraints are not violated, when the left and right sides are glued together. We reinterpret \mathcal{F} and \mathcal{L} with the additional requirement that for all the loops in these classes the rightmost site is at no point excited. This gives us two new classes, \mathcal{R} and \mathcal{M} , which are the analogues of \mathcal{F} and \mathcal{L} , except that the rightmost site is now excited at some point of the process. Additionally, these are graded by new indices c and d which mark the locations of the right boundary transitions as shown back in Equation (5.33). The new classes satisfy identical equations to the previous classes

$$\mathcal{R} = \begin{array}{c} \bullet \circ \\ \bullet \circ \end{array} * (\mathcal{R} + \mathcal{M}), \tag{5.42}$$

$$\mathcal{M} = \begin{array}{c} \bullet \circ \\ \circ \circ \\ \circ \circ \\ \bullet \circ \end{array} * (\mathcal{R} + \mathcal{M}) + \begin{array}{c} \bullet \circ \\ \circ \circ \\ \circ \bullet \\ \circ \circ \\ \bullet \circ \end{array} * \mathcal{M}. \tag{5.43}$$

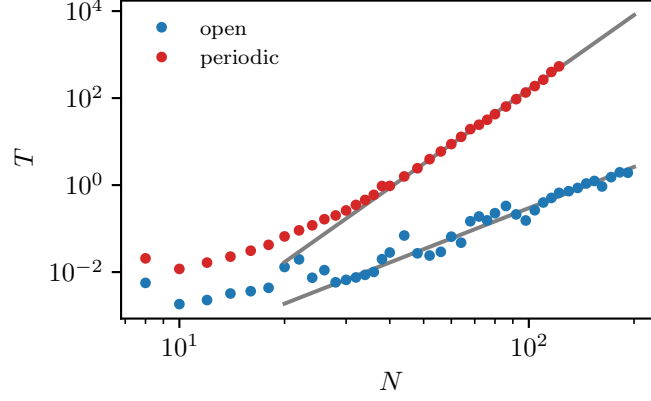


Figure 5.5: Computation time T in seconds for calculating the full set of β coefficients as a function of system size N . This is done, for both open and periodic boundaries, using dynamic programming, with the results of previous system sizes cached. A linear regression suggests an asymptotic scaling of $T = \Theta(N^3)$ for open boundaries and $T = \Theta(N^6)$ for periodic boundaries.

This is because the the gluing process never changes, whether the rightmost site is excited or not.

Keeping track of how all these indices are changed as loops are interlaced during gluing results in the following set of equations:

$$r_{N,j}^{c,d} = r_{N-2,j}^{c,d} + \sum_{a',b'} m_{N-2,j}^{a',b',c,d}, \quad (5.44)$$

$$m_{N,j}^{a,b,c,d} = r_{N,j-1}^{c-\delta(c \geq a), d-\delta(d \geq b)} + \sum_{a',b',c',d'} T^{c,c',a,k} m_{N-2,j-2}^{a',b',c',d'} T^{d,d',b,m}, \quad (5.45)$$

where

$$T^{a,c,a',c'} = \delta_{a \neq c} \sum_{k=0}^{\min(a',a-1)} \delta_{k \neq c} \delta_{c', c-\delta(c \geq a)-\delta(c \geq k)}. \quad (5.46)$$

Finally, the total number of loops is found by demanding compatibility between the left and right boundaries:

$$W_{N,j} = f_{N,j} + \sum_{a,b} l_{N,j}^{a,b} + \sum_{a>c, b>d} m_{N,j}^{a,b,c,d}. \quad (5.47)$$

The two methods of either direct computation with Eq. (5.29) and the use of

5. FORWARD-SCATTERING APPROXIMATION AND QUANTUM SCARS

the linear recurrence can be compared and indeed agree to machine precision. The recurrence method, however, gives access to much larger system size and is also more accurate. The exponential time complexity of the naïve method translates into an exponential number of arithmetic operations as sources of rounding errors. The grey lines on Figure 5.5 indicate linear regressions to the tail of the data series and the slope suggests an asymptotic scaling of $T = \Theta(N^3)$ for open boundaries and $T = \Theta(N^6)$ for periodic boundaries. The calculations were performed on a single workstation, and clearly size of the order of hundreds of sites are feasible, far beyond the possibilities of exact numerical methods.

5.4 Asymptotics and zig-zag surfaces

In this section we will uncover a classical statistical mechanical model for which the forward-scattering behaviour of PXP is encoded in the partition function. This will provide a clearer picture of the objects computed in the previous section and allow us to work directly in the thermodynamic limit. One way in which this is interesting is in the search for a classical system with a correspondence to the quantum model, that could be identified as underlying the non-equilibrium properties seen. This would be analogous to the connection between the unstable periodic orbit in the stadium billiard and the scarred wavefunctions in the quantised version. It was for precisely this relationship that the term *quantum scar* was originally coined.

The first problem that must be handled is the sheer number of loops, which grows much too fast. For $j \ll N$ the number of loops is approximately $(j!)^2$, corresponding to all the different orderings, which is faster than any exponential growth. We cannot hope to describe such a growth rate with a transfer matrix calculation. If for each transition we instead associate a continuous imaginary time in the interval $[0,1]$, then the total measure is instead unit rather than $(j!)^2$. We now have a statistical model as above but on deciding to place a forward and backward transition on a site also chooses (uniformly) a valid imaginary time for

5.4 Asymptotics and zig-zag surfaces

each of those transitions. The partition function for this model,

$$\tilde{W}_N(\mu) = \sum_j \frac{1}{(j!)^2} W_{N,j} p(\mu)^j (1 - p(\mu))^{N-j}, \quad (5.48)$$

is an exponential generating function (in $p/(1-p)$) for the number of loops considered previously. The argument μ should be thought of as a chemical potential. Alternatively, this is the expected number of forward-scattering loops when each site transitions with probability p , rescaled by the aforementioned $(j!)^2$ factor. The original object of interest can be recovered with an inverse Laplace transform,

$$W_N(k) = \frac{1}{2\pi i} \lim_{t \rightarrow \infty} \int_{\gamma-it}^{\gamma+it} d\mu \tilde{W}(\mu) (e^\mu + e^{-\mu})^N e^{\mu k} \quad (5.49)$$

$$= \frac{W_{N,j}}{(j!)^2} \delta_{k,2j-N}. \quad (5.50)$$

This can be imagined as a process that zips over the chain deciding with a probability

$$p(\mu) = \frac{e^{-\mu}}{e^{+\mu} + e^{-\mu}} \quad (5.51)$$

to make a transition on the current site. The random process described which generates configurations of this model suggests an alternative picture for the system. Configurations are coupled pairs of zigzag sequences which are alternately increasing and decreasing with synchronised resetting. Configurations are sequences consisting of zigzag runs, which are alternately increasing and decreasing, and between them empty sections. Each zigzag run starts on an even site with an exponential distribution of lengths. The empty sections consist of at least one element and follow an exponential distribution, subject to the even starting constraint aforementioned. Strictly speaking, we will only analyse the case of open boundary conditions in this section. However, the choice of boundary conditions will asymptotically only change by a constant factor (i.e. $W_{j,N}^{\text{PBC}} = \Theta(W_{j,N}^{\text{OBC}})$) that is smooth in p and therefore the β coefficients are asymptotically equal.

5. FORWARD-SCATTERING APPROXIMATION AND QUANTUM SCARS

5.4.1 Differential solution for the case of $p = 1$

For now, take the special case of $p = 1$ or $j = N$ which is much simpler. Suppose $u(x)$ is a (non-normalised) probability density for loop configurations where the left-boundary transitions at an imaginary time x measured from the midpoint (like a in Equation (5.33)). We can define a transfer operator for gluing two sites onto the left boundary as

$$(Tu)(y) = \int_0^1 dx \min(x, y) u(x). \quad (5.52)$$

This is an integral operator with a kernel function $T(y, x) = \min(x, y)$. This can be found by noticing that if the new left boundary transitions at y , then the intermediate site must transition ($p = 1$) after both x and y , and the measure of these possibilities is $\min(x, y)$.

The asymptotic form for large N can be found by solving for the dominant eigenvalue in the eigenvalue equation, $(Tu_\lambda)(y) = \lambda u_\lambda(y)$. Take derivatives,

$$\lambda u'_\lambda(y) = \frac{d}{dy} \int_0^1 dx \min(x, y) u_\lambda(x) \quad (5.53)$$

$$= \int_0^1 dx \Theta(x > y) u_\lambda(x), \quad (5.54)$$

$$\lambda u''_\lambda(y) = \frac{d}{dy} \int_0^1 dx \Theta(x > y) u_\lambda(x) \quad (5.55)$$

$$= - \int_0^1 dx \delta(y - x) u_\lambda(x) = -u_\lambda(y). \quad (5.56)$$

A general solution to this familiar differential equation is

$$u_\lambda(y) = A_\lambda \cos \frac{1}{\sqrt{\lambda}}(1 - y) + B_\lambda \sin \frac{1}{\sqrt{\lambda}}(1 - y), \quad (5.57)$$

for some constants A_λ and B_λ . The boundary conditions to consider are

$$\lambda u_\lambda(0) = (Tu_\lambda)(1) = \int_0^1 dx \min(x, 0) u_\lambda(x) = 0 \quad (5.58)$$

and

$$\lambda u'_\lambda(1) = \int_0^1 dx \Theta(x > 1) u_\lambda(x) = 0. \quad (5.59)$$

Whence the eigenvalues of T are determined to be

$$\lambda_k = \frac{4}{\pi^2 k^2}, \quad (5.60)$$

for k odd. This reproduces a classic result on alternating sequences known as André's theorem (162). The corresponding eigenfunctions are

$$u_{\lambda_k} = \cos \frac{1}{\sqrt{\lambda_k}}(1 - y). \quad (5.61)$$

The end result is an asymptotic estimate

$$W_{N,N} \sim (N!)^2 \left(\frac{4}{\pi^2} \right)^{2N}. \quad (5.62)$$

5.4.2 Numerical solution and analytic bounds in general

For the more general case when $p \neq 1$ the transfer operator is

$$\begin{aligned} \lambda u(x, x') = \int_0^1 dx \int_0^1 dx' & \left((1-p)^2 u(x, x') \delta(y) \delta(y') + p(1-p) u(x, x') \right. \\ & \left. + p^2 \min(x, y) \min(x', y') u(x, x') \right). \end{aligned} \quad (5.63)$$

The first term is when neither of the two additional sites transitions, this produces delta functions as a “mass” at $y = 0$. These can be interpreted as the left boundary site not transitioning, as the measure for the disallowed process (the third term) vanishes at this point. The second term is when, in the two site system glued on the left, the initially \bullet site on the new boundary transitions but the initially \circ intermediate site does not; this process erases information about the previous state. The third term is the only term that survives in the previously considered $p = 1$ case, corresponding to the case when both of the additional sites transition.

5. FORWARD-SCATTERING APPROXIMATION AND QUANTUM SCARS

Alternatively the distribution can be separated into a continuous portion u and a point mass f at $y = y' = 0$, following the convention chosen in the previous sections,

$$\lambda u(y, y') = \int_0^1 dx \int_0^1 dx' (p(1-p) + p^2 \min(x, y) \min(x, y')) l(x, x') + p(1-p)f, \quad (5.64)$$

$$\lambda f = \int_0^1 dx \int_0^1 dx' (1-p)^2 l(x, x') + (1-p)^2 f. \quad (5.65)$$

We can eliminate f from the problem as follows

$$\lambda f = (1-p)^2 \left(\int_0^1 dx \int_0^1 dx' l(x, x') + f \right), \quad (5.66)$$

$$f = \frac{(1-p)^2}{\lambda - (1-p)^2} \int_0^1 dx \int_0^1 dx' l(x, x'), \quad (5.67)$$

whence we find

$$\lambda l(y, y') = \int_0^1 dx \int_0^1 dx' (\alpha_\lambda + p^2 \min(x, y) \min(x', y')) l(x, x'), \quad (5.68)$$

where

$$\alpha_\lambda = \frac{\lambda p(1-p)}{\lambda - (1-p)^2}. \quad (5.69)$$

This is then a problem which would have to be solved self-consistently for λ , however it is already even under the fiction that α_λ and λ are independent. We could attempt the same procedure and derive an equivalent differential equation away from the previously considered case of $p = 1$. This produces a simple enough differential equation, however the constant term in the transfer operator creates non-local boundary conditions and so far has resisted solution. We will instead show numerical solution for and analytic bounds on the dominant eigenvalue of this transfer operator.

The main tool we use to provide bounds is a Collatz-Wielandt (37, 110) formula for compact operators for which we sketch a proof. Let $A : M \rightarrow M$ on a

5.4 Asymptotics and zig-zag surfaces

Banach space M with a Schauder basis be some compact and strongly positive operator according to some total order cone K , with positive spectral radius. Define functions $f(u)$ and $g(u)$ for any u interior to the order cone as

$$f(u) = \min_x \frac{(A(u))(x)}{u(x)} \quad \text{and} \quad g(u) = \max_x \frac{(A(u))(x)}{u(x)}. \quad (5.70)$$

We have written elements of M as functions of elements from some base space X . This should be understood as minimising (or maximising) over some set of functionals which span the algebraic dual. Now “pointwise” we have that

$$0 \leq f(u)u(x) \leq Au(x) \leq g(u)u(x). \quad (5.71)$$

Using the Krein-Rutman theorem, which generalises the Perron-Frobenius theorem to Banach spaces (95), the spectral radius of A is infact an algebraically simple eigenvalue λ with a strictly positive eigenvector, and the same is true of the dual operator A^T . Let w be this eigenvector, then

$$0 \leq f(u)\langle w, u \rangle \leq \lambda\langle w, u \rangle \leq g(u)\langle w, u \rangle. \quad (5.72)$$

Since w and u are both interior to the total cone, $\langle w, u \rangle > 0$ and we arrive at the general bound

$$0 \leq f(u) \leq \lambda \leq g(u). \quad (5.73)$$

Starting from Equation (5.65), we apply these inequalities to the dual transfer operator, as T is non-symmetric and this provides better bounds. The preconditions for the Collatz-Wielandt formula are all satisfied, provided p is not 0 or 1 — cases which can be resolved by continuity. The transfer operator is considered over space $1 \oplus C([0, 1]^2)$, where 1 is the one-dimensional vector space representing the point mass and $C([0, 1]^2)$ is the function space of continuous functions from the unit square. By choosing an element u that is the sum of the positive unit vector for the point space and a positive constant function over the unit square, we arrive at the bounds,

$$1 - p + \frac{p^2}{4} \geq \lambda \geq 1 - p. \quad (5.74)$$

5. FORWARD-SCATTERING APPROXIMATION AND QUANTUM SCARS

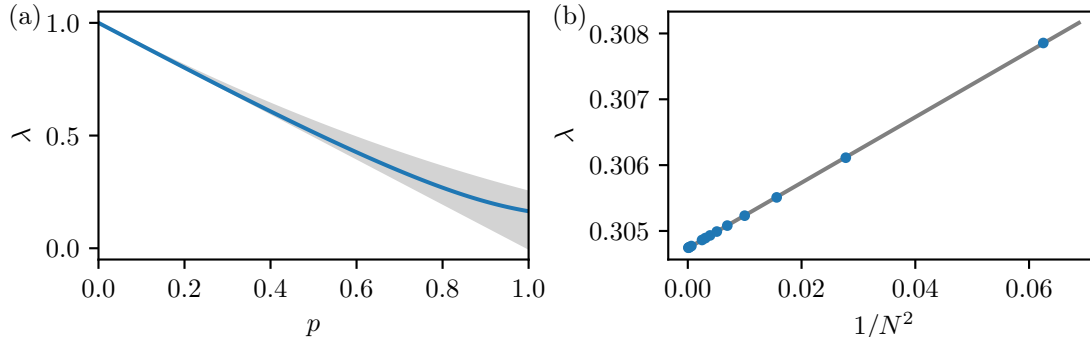


Figure 5.6: Numerical solution for the dominant eigenvalue λ of the transfer operator, Equation (5.63). (a) Dominant eigenvalue λ as a function of the transition probability p . The shaded area is the feasible region for the bounds in Equation (5.74). (b) Convergence of the numerical solution for λ scales as $1/N^2$ as finer discretisations are taken.

These bounds are shown as the shaded area in Figure 5.6 (a) alongside the value obtained by numerical solution. The bound can also be seen by considering the *columns* of the discretised transfer operator that follows.

We find numerical solution of Equation (5.65) by discretising the unit square into an N by N grid. This leads to transfer matrices of the form

$$\left(\begin{array}{c|c} (1-p)^2 & \frac{1}{N^2}(1-p)^2 \\ \hline p(1-p) & \frac{1}{N^2} \left(p(1-p) + p^2 \frac{2 \min(j,k)+1}{2N} \frac{2 \min(j',k')+1}{2N} \right) \end{array} \right), \quad (5.75)$$

where the right column takes an extra indices k and k' and the bottom row takes extra indices j and j' . This means that the top-right block is a N^2 -dimensional row vector, the bottom-left block is a N^2 -dimensional column vector and the bottom-right block a N^2 by N^2 matrix. In Figure 5.6 (b) we show the convergence as the discretisation is made finer (i.e. $N \rightarrow \infty$) for $p = 0.75$, as expected for smooth solutions convergence is proportional to $1/N^2$. The curve shown in Figure 5.6 (a) is the result of extrapolating from these discretised solutions with a linear regression.

In this section, we have shown how quantities can be calculated within the forward-scattering approximation even directly in the thermodynamic limit. We demonstrated this for finding the matrix elements of the Hamiltonian in the

Lanczos basis. However, this could be extended to find matrix elements of local observables or correlation functions. This extension would work by describing each local operator insertion as an alternative transfer operator in the product.

5.5 Conclusions

In this chapter we have developed a way of identifying a subspace which is approximately dynamically separated from the rest of the Hilbert space. This subspace we call the forward-scattering subspace \mathcal{K} , and calculations within it we call forward-scattering approximations (FSA). The subspace \mathcal{K} contains the initial state and has high overlap with all of the special eigenstates, thus it provides a description for the non-equilibrium physics observed in the experiment (19). We can interpret \mathcal{K} as being analogous to the bouncing ball quasi-modes in the story of single-particle quantum scars. The main achievement is in identifying this subspace out of the exponentially large dimensional full Hilbert space, and then showing that quantities within it can be calculated efficiently. Central to the method is a splitting of the Hamiltonian into two terms which are identified with raising and lower operators. This gives rise to the physical interpretation of the subspace, and the dynamics therein, being that of a large deformed spin. This intuition will be further developed in Chapter 6.

We created systems of linear recurrences which show that calculations projected into the subspace \mathcal{K} can be performed exactly in polynomial time. This was used to find matrix elements of the Hamiltonian in this subspace. Other quantities such as commutators, $[H^+, H^-]$ and some local observables, can be calculated in the same way. We also showed how the PXP model in this approximation is related to a statistical mechanical model of alternating surfaces and transfer operator calculations, which were solved exactly at a special point. By discretising the transfer operator problem, we can calculate within the FSA directly in the thermodynamic limit, with only a controllable additional discretisation error. In this way the time complexity is made independent of system size N .

A concern is the errors of the approximations in the analysis which leads to a leaking of probability out of the special subspace. Errors were found to be small,

5. FORWARD-SCATTERING APPROXIMATION AND QUANTUM SCARS

suitable for the recovery of local observables in dynamics, but eigenstates can be exponentially sensitive through their dependence on the density of states. The subsequent chapter will focus on mitigating this by the use of local perturbations. Not only will this stabilise an internally coherent (undeformed) large spin that is well isolated from the complementary subspace, but the errors in the forward-scattering method will be reduced until they are as small as one part in a million up to the largest accessible system sizes.

Chapter 6

Enhanced quantum revival and emergent $SU(2)$ dynamics

The picture we have advanced in Chapter 4 to explain the experimental findings is one of a small non-ergodic subspace of scarred eigenstates hiding within an otherwise thermalising spectrum. In Chapter 5, we found that the effective model for the Rydberg atom experiment has a non-ergodic large spin subspace. This subspace was constructed only approximately, analogously to the bouncing ball quasi-modes in the single-particle quantum scar, in the hope of using it to show the existence of the scarred eigenstate, and to study their properties. The Hamiltonian within this subspace was generated by a pair of raising and lowering operators, H^+ and H^- . It's good to keep in mind alternative propositions such as proximity to integrability (86). In Section 4.5.2, we looked at known nearby integrable points, which were found to have little to do with the behaviour of the PXP model. The integrability hypothesis would then rely on some hitherto unknown realisation of an integrable system. According to this hypothesis the entire Hilbert space would become strongly non-ergodic sufficiently close to this purported integrable point. In the opposite direction when leaving the integral point, it would require that some eigenstates of this integrable point are less sensitive to integrability breaking to leave behind a remnant of special eigenstates.

In this chapter, based on our work in (35), we will show the non-ergodic subspace can be enhanced by addition of small extra terms, while the complementary

6. ENHANCED QUANTUM REVIVAL AND EMERGENT SU(2) DYNAMICS

subspace remains thermal, contrary to hypothesis of proximity to integrability. First, we will review the findings of Ref. (86). We then show that, with numerically optimised coefficients, the quantum revival can be made almost perfect with a suitable exponentially local perturbation. At the same time, the growth in entanglement is nearly arrested. We find with this carefully chosen deformation, the forward-scattering subspace of Chapter 5, appropriately modified, becomes almost exactly closed under the dynamics. At the end, we discuss some related results on other anomalously non-thermal quantum systems.

6.1 Deformation to suppress level repulsion

First, we cover the results of Ref. (86). To facilitate a change in notation, we restate the Hamiltonian as

$$H_0 = \sum_j P_{j-1} X_j P_{j+1}. \quad (6.1)$$

We will consider systems $H = H_0 + h \delta H_2$ with perturbation

$$\delta H_2 = \sum_j P_{j-1} X_j P_{j+1} (Z_{i+2} + Z_{i-2}). \quad (6.2)$$

This is equivalent to the perturbation used in Ref. (86), where they found a minimum in the r -statistic, defined in Equation (4.16), for open boundary conditions at around $h \approx 0.01$. It can be motivated as the only perturbation within this range that preserves both the spatial-inversion and time-reversal symmetries, and the spectral reflection symmetry. They interpreted this finding as a signature of a close-by near-integrable point and conjectured that the behaviour of the unperturbed system (6.1) was due to proximity to that special point in parameter space.

In Figure 6.1, we show the same result, although for the case of periodic boundaries where care must be taken to resolve all the spatial symmetries. Here a dip in the r -statistic is observed, this time around $h \approx 0.024$. The difference between boundary conditions is not particularly unusual as integrable systems are

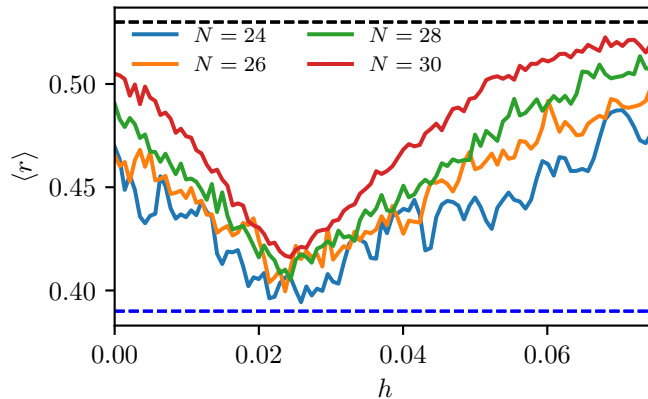


Figure 6.1: Minimum in the r -statistic. As reported in Ref. (86) the r -statistic with perturbation, Equation (6.2), displays a minimum as a function of h around $h \approx 0.024$ for periodic boundaries, this is around twice the value found for open boundary conditions. Ref. (86) conjectured that this is an indicator of a nearby integrable point, whose proximity explain the behaviour of the unperturbed model in Equation (6.1).

often quite sensitive to boundary conditions. We will examine the consequences of this perturbation on the dynamical and algebraic properties explored previously. We will find that these properties can also be greatly improved with the addition of this perturbation.

6.2 Deformation to stabilise revivals

The optimal coupling constant for the dynamical properties is found to be $h \approx 0.05$, i.e. , around twice as large as the perturbation which minimises $\langle r \rangle$. Later in the chapter we will demonstrate that with additional perturbations the improvement can be such that for $N = 32$ sites the first revival has a probability deficit of around 10^{-6} . This is not to say that there is no near-integrable point or that it is not relevant, but that this would a priori give the expectation to find the best oscillatory behaviour at that same integrable point. For now, it is good to observe that at this point of interest ($h \approx 0.05$) the r -statistic is trending toward the GOE value $\langle r \rangle \approx 0.53$ with increasing system size N .

In Figure 6.2 we show the effect of the deformation on (a) the fidelity $g(t) = |\langle \mathbb{Z}_2 | \psi(t) \rangle|^2$ and (b) the midpoint entanglement entropy S for the unperturbed

6. ENHANCED QUANTUM REVIVAL AND EMERGENT SU(2) DYNAMICS

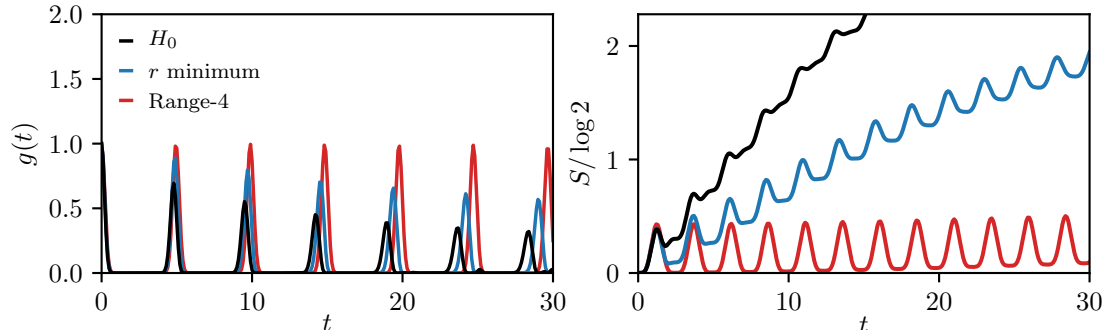


Figure 6.2: Enhanced oscillatory dynamics of the PXP model with range-4 perturbation. Many-body fidelity g and bipartite entanglement entropy S following a quench from the Néel state for the system with perturbation eq. (6.2). The perturbation chosen to minimise the r -statistic ($h \approx 0.024$) improves fidelity of revivals and suppresses the linear growth in entropy. The optimal value for this effect is however around $h \approx 0.048$.

model $h = 0$ (black), the coupling that minimises the r -statistic $h \approx 0.024$ (blue) and the value chosen to maximise the return probability $h \approx 0.048$ (red). The return probability is enhanced and the entropy growth suppressed by the $\langle r \rangle$ minimising coupling constant. At the optimal value around $h \approx 0.0481$ this effects is greatly enhanced leading to fidelity $g(\tau) \approx 0.998$ at its first maximum for $N = 32$ sites. Furthermore the linear growth in entanglement entropy is greatly slowed down with more pronounced oscillations.

6.3 Algebraic argument for revival stabilisation

This effect can be seen in the forward-scattering analysis, introduced in Chapter 5, as a partial cancellation in the first non-trivial forward scattering error. More precisely we can show, after redefining the raising and lower operators H^\pm , that the component of $H^- H^+ |v_2\rangle$ perpendicular to $|v_2\rangle$ is minimised close to the value observed.

The forward and backward scattering, or variously raising and lowering, operators are a splitting of the Hamiltonian H into parts which raise and lower the eigenvalue of the alternating field operator $A = -\sum_j (-1)^j Z_j$ respectively.

6.3 Algebraic argument for revival stabilisation

Explicitly these are

$$H^\pm = \sum_j (P_{2j-2} S_{2j-1}^\pm P_{2j} W_{2j-1} + P_{2j-1} S_{2j}^\mp P_{2j+1} W_{2j}) \quad (6.3)$$

where

$$W_j = 1 + h(Z_{j-2} + Z_{j+2}). \quad (6.4)$$

We will connect the forward-scattering errors to the behaviour of the commutator $[H^+, H^-]$, which is more convenient for calculation. First, define a number of error quantities:-

$$\epsilon_\mu^{(j)} = \min_\mu \| (H^- H^+ - \mu) |j\rangle \|, \quad (6.5)$$

$$\epsilon_\lambda^{(j)} = \min_\lambda \| ([H^+, H^-] - \lambda) |j\rangle \|, \quad (6.6)$$

$$\epsilon_\kappa^{(j)} = \min_\kappa \| (H^+ H^- - \kappa) |j\rangle \|. \quad (6.7)$$

The subscripts μ , λ and κ are simply labels rather than variables or indices. If the forward-scattering analysis were exact, then these quantities would all be zero, indeed $\epsilon_\mu^{(j)}$ is just a new name for the original forward-scattering error from Section 5.2. Now, from the triangle inequality,

$$\| (H^- H^+ - \mu) |j\rangle \| \leq \| ([H^+, H^-] - \lambda) |j\rangle \| + \| (H^+ H^- - \mu) |j\rangle \|, \quad (6.8)$$

for any choice of λ, κ and μ such that $\lambda + \kappa = \mu$. We can first minimise the first term of the right-hand side over λ , then minimise the left-hand side which breaks the relationship between κ and μ . Finally, κ is then free to be minimised leading to a triangle inequality between the different error quantities,

$$\epsilon_\mu^{(j)} \leq \epsilon_\lambda^{(j)} + \epsilon_\kappa^{(j)}. \quad (6.9)$$

The process can be followed to find the two other triangle inequalities to demonstrate that the error quantities form the sides of a triangle.

If we look more closely at $\epsilon_\kappa^{(2)}$, we see that it vanishes because there is only one state at a Hamming distance of one with the appropriate symmetry. This means

6. ENHANCED QUANTUM REVIVAL AND EMERGENT SU(2) DYNAMICS

that the first non-trivial forward scattering error $\epsilon_\mu^{(2)}$ is equal to the commutator error $\epsilon_\lambda^{(2)}$, which allows us to focus on the commutator error. Beyond $j = 2$ where $\epsilon_\kappa^{(2)}$ may not vanish, we would still expect each of these quantities to be similar in magnitude as they all essentially measure the extent to which the forward-scattering subspace is not H -invariant around the state $|j\rangle$.

In calculating the commutator $H^z = [H^+, H^-]$, we can break up the calculation into the commutators of individual terms. If the centres of these terms (the site on which the S^\pm operator sits) are separated by more than 2 sites then the commutator vanishes. Additionally, if the centres are separated by a single site, then the commutator vanishes because the products attempt a forbidden $\circ\circ \leftrightarrow \bullet\bullet$ transition. The remaining contributions can be calculated to find

$$\begin{aligned}
H^z &= \sum_j (-1)^{j+1} \left(P_{j-1} P_{j+1} W_j^2 [S_j^+, S_j^-] + P_{j-2} P_j P_{j+2} [S_{j-1}^+ W_{j-1}, S_{j+1}^- W_{j+1}] \right. \\
&\quad \left. - P_{j-2} P_j P_{j+2} [S_{j-1}^- W_{j-1}, S_{j+1}^+ W_{j+1}] \right), \\
H^z &= \sum_j (-1)^{j+1} \left(P_{j-1} Z_j P_{j+1} W_j^2 \right. \\
&\quad \left. + 2h P_{j-2} P_j P_{j+2} (2 + h(Z_{j-3} + Z_{j+3})) (S_{j-1}^+ S_{j+1}^- + S_{j-1}^- S_{j+1}^+) \right).
\end{aligned} \tag{6.10}$$

To calculate the first non-trivial error, we first find the Lanczos vector

$$|2\rangle = \gamma_2 \sum_j \left(S_{2j}^- S_{2j+2}^- + (1 - 2h) \sum_{k>j+1} S_{2j}^- S_{2k}^- \right) |0\rangle, \tag{6.11}$$

where γ_2 is a constant chosen for normalisation. Then, we calculate the action of H^z upon it,

$$\begin{aligned}
H^z |2\rangle &= \gamma_2 \sum_j \left(f_2(h, N) S_{2j}^- S_{2j+2}^- + (1 - 2h) f_4(h, N) S_{2j}^- S_{2j+4}^- \right. \\
&\quad \left. + (1 - 2h) f_6(h, N) \sum_{k>j+1} S_{2j}^- S_{2k}^- \right) |0\rangle
\end{aligned} \tag{6.12}$$

6.3 Algebraic argument for revival stabilisation

where the functions

$$f_2(h, N) = -(1 - 2h)^2 \left(\frac{N}{2} - 4 \right) - 1 - 12h + 12h^2, \quad (6.13)$$

$$f_4(h, N) = -(1 - 2h)^2 \left(\frac{N}{2} - 5 \right) - 1 - 20h + 12h^2 - \frac{8h}{1 - 2h}, \quad (6.14)$$

$$f_6(h, N) = -(1 - 2h)^2 \left(\frac{N}{2} - 6 \right) - 2 - 24h + 24h^2, \quad (6.15)$$

can be determined by careful and lengthy calculation from Equation (6.10) and Equation (6.11).

The greatest number of contributions come from the f_6 term which then essentially sets the constant of proportionality λ between $|2\rangle$ and $H^z |2\rangle$. The number of contributions for terms carrying f_2 and f_4 are equal, hence the error scales like

$$\left(\epsilon_\lambda^{(2)} \right)^2 \propto (f_6 - f_2)^2 + (f_6 - f_4)^2. \quad (6.16)$$

The minimum point is found at

$$h = \frac{29}{82} - \frac{\sqrt{159}}{41} \approx 0.0461, \quad (6.17)$$

which is around 10% from the numerically observed value at $N = 20$, a discrepancy due to finite N . This suggests that the additional term leads to an improvement in the oscillatory dynamics through improving the accuracy of the forward-scattering analysis, as opposed to some entirely separate effect.

Without perturbation, we previously observed that the scatter plot between eigenstate overlap with the Néel state and energy has a characteristic structure, with a band of special states approximately equally spaced in energy and with anomalously large overlap with the Néel state. These special states also had anomalously low entanglement entropy, with typical states forming a narrow parabola shaped distribution where the entanglement entropy is related to the subsystem thermodynamic entropy. These results are reproduced in the left column of Figure 6.3 for $N = 30$ sites.

We track the effects of the addition of the perturbation in Figure 6.3. In the middle column of Figure 6.3, we consider the effect when the coupling constant which minimises the r -statistic around $h \approx 0.02$. The overlap panel dis-

6. ENHANCED QUANTUM REVIVAL AND EMERGENT SU(2) DYNAMICS

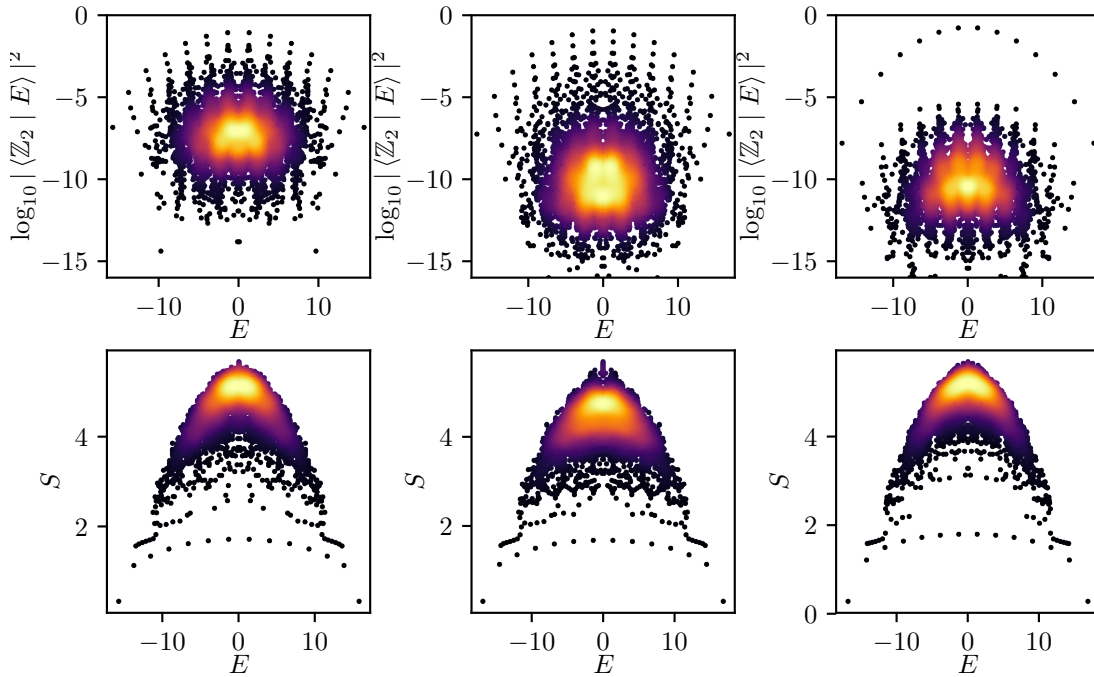


Figure 6.3: Eigenstate properties of the PXP model with range-4 perturbation. Top row: Scatter plot of eigenstate overlap with $|\mathbb{Z}_2\rangle$ and energy. Bottom row: Scatter plot of eigenstate midpoint entanglement entropy with energy. Results are for (left) unperturbed model, (middle) perturbation with strength $h \approx 0.02$ chosen to minimise the r -statistic and (right) with strength $h \approx 0.0481$ which maximises the quality of the quantum revivals. Where the density of points is high, colour is used to indicate their density.

plays a striking visual regularity, organising into vertical “towers” and horizontal “bands”. We also observe the broadening of the distribution of entanglement entropies for typical states in the bottom row. This is consistent with the deviation from Wigner-Dyson level statistics at this point and suggestive of a broader breakdown of eigenstate thermalisation for the entire spectrum.

In the right column we move on to the coupling strength which leads to the highest quality revivals. The main effect seen at this coupling strength is the separation in overlap between the special states from the remainder. Furthermore, the remaining states concentrate around the same energies as the special states. The resulting narrow peaked distribution of overlap against energy is consistent with the high quality revivals observed in its Fourier transform, the Loschmidt echo. For typical states the entanglement entropy forms a narrow parabola once again, indicative of the return to eigenstate thermalisation for typical states. These results support the hypothesis that an isolated non-thermal H -invariant subspace hidden within an ergodic “bulk” and that this reason for the dynamical phenomena is independent of any nearby integrable point contrary to Ref. (86).

6.4 Long-range deformation

The success in improving the non-equilibrium dynamics with the simple perturbation suggests it may be possible to further enhance the effect. It is natural to consider longer-range versions of the same perturbation of the form

$$\delta H = \sum_{d=2}^{\infty} h_d \sum_j P_{j-1} X_j P_{j+1} (Z_{j+d} + Z_{j-d}), \quad (6.18)$$

where $\{h_d\}$ are a sequence of coupling constants. With this perturbation the precession rate, between \circ and \bullet , of each site is influenced by the states of atoms at increasing distances.

We numerically optimise the coupling constants to maximise the fidelity g at the first revival. The coupling constants found in this way are shown in Figure 6.4. In the following section we will give details about this optimisation and the optimisation of related cost functions. The coupling constants are found to

6. ENHANCED QUANTUM REVIVAL AND EMERGENT SU(2) DYNAMICS

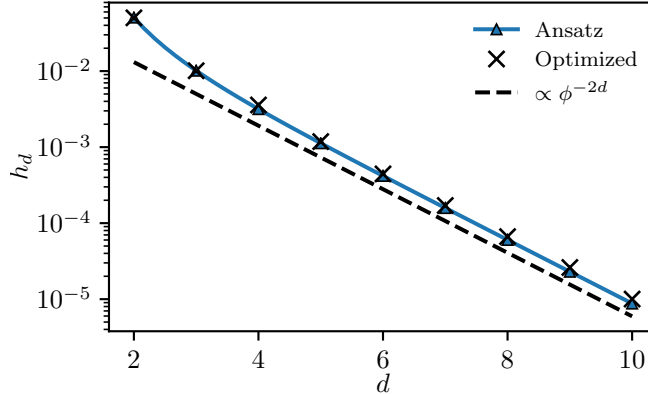


Figure 6.4: Coupling constants h_d in Equation (6.18) when chosen to maximise the fidelity at first revival. These decay exponentially and are well fit by Equation (6.19).

be exponentially decaying making this an (exponentially) local perturbation that can be fit by the simple function form

$$h_d \approx \frac{c}{(\phi^{+(d-1)} - \phi^{-(d-1)})^2} \quad (6.19)$$

where ϕ is the golden ratio and c is some constant factor. The denominator of this expression is a Fibonacci number.

In Figure 6.5 we compare the original unperturbed system, the system with the optimal short-range perturbation Equation (6.2) found previously and the optimal long-range perturbation Equation (6.18) for a periodic system of $N = 32$ sites. The quantum fidelity periodically revives with very small losses. This can be seen in the inset to Figure 6.5 (a) which zooms in around the first revival at a time τ . The infidelity here can be made as small as $1 - g(\tau) \approx 10^{-6}$. Consistently the entanglement entropy at each revival drops back nearly to zero removing the linear growth typical of thermalising systems.

While this deformed model shows very stable non-equilibrium dynamics the bulk of the spectrum remains thermal. To demonstrate this, we compute the distribution of unfolded level spacings $P(s)$ shown in Figure 6.6 and the r-statistics (inset). Both are consistent with the Wigner-Dyson surmise and show level repulsion. Furthermore the trend with increasing system size N is clearly towards

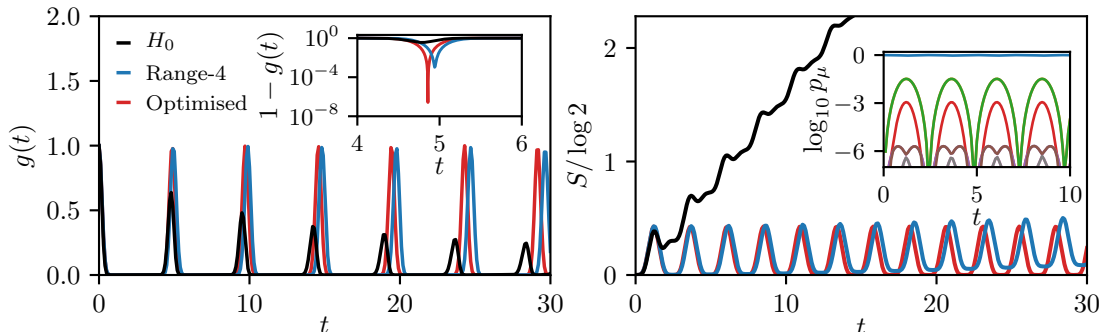


Figure 6.5: Enhanced oscillatory dynamics of the PXP model with long-ranged perturbation. Many-body fidelity g (left) and bipartite entanglement entropy S (right) following a quench from the Néel state for the system with perturbation Equation (6.2). Data is for system size $N = 32$. (left inset) Close up on the infidelity $1 - g$ at first revival shows the difference between the effects of the short-range perturbation Equation (6.2) and the long-range perturbation Equation (6.18). (right inset) Clear oscillations in the leading eigenvalues of the reduced density matrix for the half system with the long-range perturbation.

the GOE value of $\langle r \rangle \approx 0.53$.

The near perfect fidelity revivals with the deformed Hamiltonian suggests there is a small-dimensional subspace that has very high overlap with the initial state and is closed under the action of the Hamiltonian. In the following section we will see that the forward-scattering subspace itself is almost H -invariant at this point. This then suggests that the H^+ and H^- form a closed algebra within this subspace \mathcal{K} . We numerically verify the approximate root system,

$$\mathcal{K}([H^z, H^\pm]) \approx \pm \Delta \mathcal{K}(h^\pm) \quad (6.20)$$

where Δ is a scalar constant and superoperator \mathcal{K} acts by projecting into the subspace \mathcal{K} . To the extent Equation (6.20) holds, the algebra generated in the subspace is that, up to a multiplicative factor, of a representation of $SU(2)$. The manner in which the forward-scattering subspace is constructed suggests that this should be a single large spin representation (spin $S = N/2$).

In this identification the forward-propagating and backward-propagating parts of the Hamiltonian are taken to be similar to raising and lower operators of this large spin. The matrix elements are the β coefficients that were calculated

6. ENHANCED QUANTUM REVIVAL AND EMERGENT SU(2) DYNAMICS

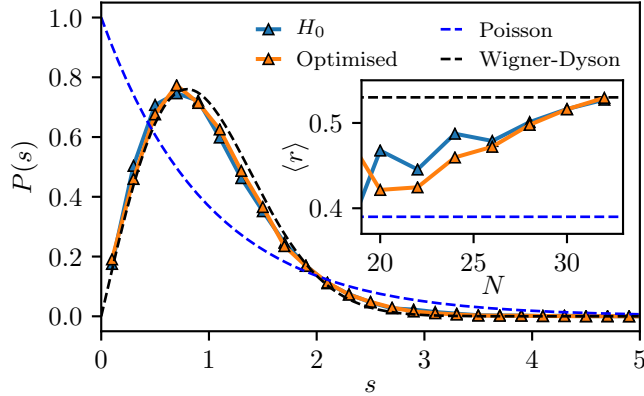


Figure 6.6: Level statistics in the PXP model with long-ranged perturbation. Distribution $P(s)$ of unfolded level spacings s for the system with the optimal long-range perturbation and the unperturbed system for comparison. As expected from the r -statistic shown in Figure 6.1 both are well described by the Wigner surmise and exhibit level repulsion. (inset) The r -statistic converges with system size N towards the GOE value.

previously in the case without perturbation. The SU(2) theory prediction for these matrix elements is

$$\beta_k \propto \sqrt{(k + N/2 + 1)(N/2 - k)}. \quad (6.21)$$

This is shown in Figure 6.7 (a) where we find the optimised model can be well fit to this functional form. In contrast, the unperturbed model noticeably deviates from the curve. The commutator $H_z = [H^+, H^-]$ then plays the role of a rescaled S^z spin projection operator in this picture. Projected into the forward-scattering subspace, H_z forms a diagonal matrix. We find the diagonal matrix elements $H_k^z = \langle k | H^z | k \rangle$ in Figure 6.7 (b) to be well fit by a straight line as is to be expected from a spin projection operator. Finally, in this picture, the oscillatory dynamics following a quench to $|\mathbb{Z}_2\rangle$ can be intuitively understood as the precession around a field aligned in the x -direction of a spin originally aligned in the z -direction.

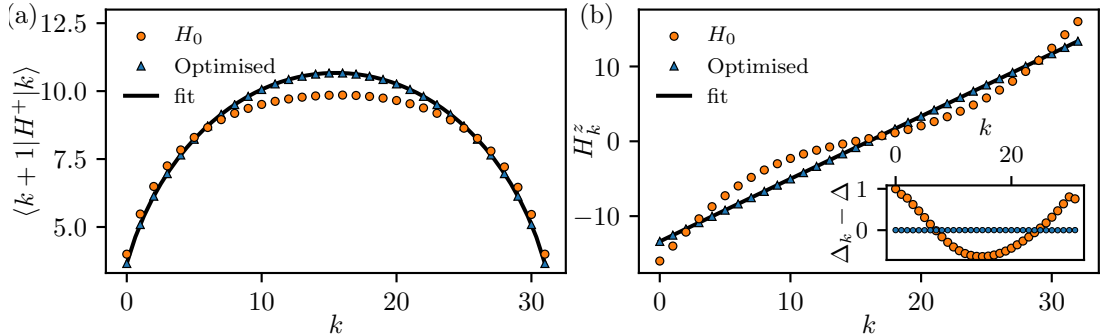


Figure 6.7: Algebraic structure in forward-scattering subspace. This is a comparison between the unperturbed system and that with the optimal long-range perturbation, Equation (6.18). (left) Off-diagonal matrix elements of the Hamiltonian in the forward-scattering subspace $\beta_{k+1} = \langle k+1|H^+|k\rangle$. (right) Diagonal matrix elements of forward-scattering commutator $H_z = [H^+, H^-]$. The matrix elements of the optimised model are fit to a curve directly proportional to $\sqrt{(k+1)(N-k)}$, which is the curve these coefficients follow for the unconstrained paramagnet.

6.5 Parameter optimisation

In the previous section we presented results for coupling constants $\{h_d\}$ chosen to maximise the return probability of the Néel state at the first revival. It was found that this infidelity could be made remarkably small, while preserving the ergodic nature of the remainder of the Hilbert space. This suggests the phenomena observed is independent of integrability. In this section we now discuss some details of this optimisation procedure, and compare that with some alternative optimization schemes. Since optimizing the fidelity revivals simultaneously tunes several properties of the system (e.g. the microscopic structure of eigenstates and their energy separation), we would like to understand the effect of perturbations on each one of these properties. The evaluation of these alternative quantities in some cases could be much more computationally tractable than calculating the fidelity time-series. For this, we shall consider some alternative cost functions (or figures of merit) which capture different properties of the system that we expect to be important for producing the high return probability. As we explain below, these cost functions are defined to vanish for the optimal model when there is an exact $SU(2)$ invariant subspace.

6. ENHANCED QUANTUM REVIVAL AND EMERGENT SU(2) DYNAMICS

We start by introducing these different cost functions. The first cost function is our main object of interest – the return probability at the first revival. In a short time interval around each revival, the fidelity is reliably unimodal, and as such we can use a golden-section search to efficiently determine the location of the revival peak, that is the period of the revival. On top of this, there is a variational optimization for the couplings $\{h_d\}$. Since we do not have much intuition about the cost function expressed in terms of the couplings, we resort to a general optimisation strategy, specifically we used the Nelder-Mead simplex search, as implemented in the Scipy Python package. We use the same type of search when optimizing any of the other cost functions mentioned below.

The second measure we consider is the subspace variance, which was introduced in Section 5.2, which measures the energy fluctuations of a subspace. In terms of the projection superoperator \mathcal{K} into the forward scattering subspace it can be expressed as

$$\text{var}_{\mathcal{K}}(H) = \sum_j \text{var}_{\tilde{\psi}_j}(H) = \text{tr}\{\mathcal{K}H^2 - (\mathcal{K}H)^2\}. \quad (6.22)$$

Additionally, common to the case without perturbation discussed in the previous chapter, this quantity is equivalent to the trace of the commutator,

$$\text{var}_{\mathcal{K}}(H) = \text{tr}\{\mathcal{K}[H^+, H^-]\} = \text{tr}\{\mathcal{K}(H^z)\}, \quad (6.23)$$

which featured in the derivation of the optimal short range perturbation. We will use this to measure H -invariance for the forward-scattering subspace \mathcal{K} . If the subspace variance were zero then the forward-scattering subspace would be closed. Recall that the presence of perfect revivals would require the existence of such a low dimensional closed subspace necessary, see Section 4.3. This measure is also computationally easier than finding the revival peak as it can be obtained with matrix product state methods. With this measure, beyond testing for a low-complexity approximately H -invariant subspace, we are testing our hypothesis that the subspace can be generated with our matrix splitting $H = H^+ + H^-$.

The third measure is a FSA error cost function — the first non-trivial forward-

scattering error from Section 5.2,

$$\|\delta v_3\|^2 = \|H^- |3\rangle - \beta_3 |2\rangle\|^2 = \langle 3| H^+ H^- |3\rangle - \beta_3^2. \quad (6.24)$$

The FSA error must be zero if the forward-scattering subspace is to be H -invariant, but is itself not a sufficient condition. It is but one contribution to the subspace variance, which is the sum of the forward-scattering errors at each step.

The final surrogate we use seeks to measure how “anharmonic” are the energy spacings. We do this by taking the Ritz values (i.e. the FSA approximations to the associated special eigenvalues) and finding the least-squares fit to having equally spaced energy levels, i.e. minimising the root-mean-square of the residuals. Precisely, this is

$$f_{\text{rval}} = \min_{m,c} |\epsilon_j - jm - c|^2, \quad (6.25)$$

where $\{\epsilon_j\} = \text{eig}(\mathcal{K}(H))$ are the sorted Ritz values. This measure is testing the idea that in the effective decoupled subspace, the Hamiltonian acts as a S^x generator of a large-spin representation of $\text{SU}(2)$. Unlike the previous cost functions which were focussed on how well decoupled the forward-scattering subspace is from the rest of the system, the present Ritz-value cost function only sees the dynamics within the subspace.

The different optimisation schemes are found to result in very similar coupling constants, in particular they all follow the same rough dependence on d as captured by Equation (6.19). The coupling constants $\{h_d\}$ are shown together in Figure 6.8 (a), which we found by numerical optimisation for a system of $N = 20$ sites. Optimising for the harmonic spacing of Ritz values leads to some non-monotonic behaviour in the coupling constants, but these still follow the same general trend. They also behave inconsistently with regards to system size which indicates this measure is not particularly well behaved.

We show the correlations between the different optimisation schemes in Figure 6.8 (b). In each of the four panels we find the optimised coupling constants according to a particular cost function (given on the x -axis), and then evaluated the cost according to each of the figures of merit (marked according to the legend). We performed these calculations, again, for a size of $N = 20$ because of

6. ENHANCED QUANTUM REVIVAL AND EMERGENT SU(2) DYNAMICS

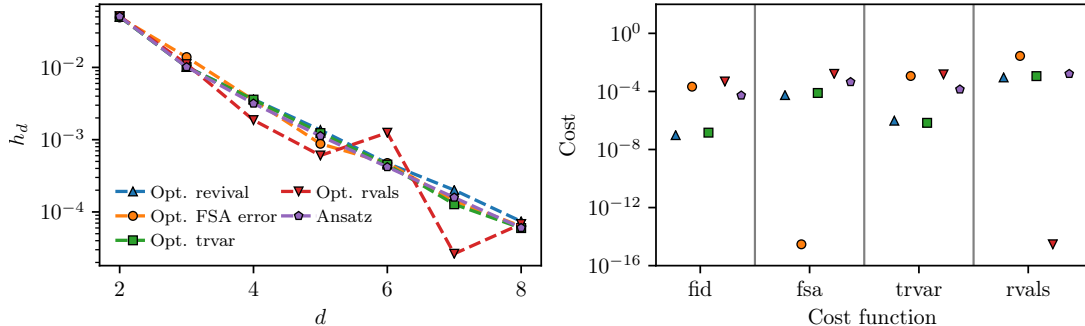


Figure 6.8: Cross-comparison of the different cost functions. (a) Coupling constants for the perturbation found by minimizing various cost functions. The labels: “fid” refers to the fidelity deficit at the first revival (also used in the main text); “fsa” to the first non-trivial forward-scattering error, Equation (6.24); “trvar” to the subspace variance, 6.22, and “rvals” to the anharmonicity of Ritz values, 6.22. (b) Evaluating the results of each of these optimization choices against these same figures of merit. Different optimization choices are labelled in the same way as in the left panel. The trace variance works as a good surrogate for the fidelity deficit, which implies that the most important factor in producing the quantum revivals is creating a good closed subspace.

the large number of different couplings that need to be examined. One feature that particularly stands out is that optimizing for the first non-trivial error in the FSA is no longer sufficient to find the fidelity maximum once longer range terms are added beyond range 4. It’s possible to make this cost function very small, however this has little further impact on the revivals or trace variance. In contrast, optimising for the subspace variance fares much better – its optimal model also produces fidelity revivals with very similar accuracy. This highlights how having a low-dimensional approximately H -invariant subspace, which contains the initial state, is a stringent condition and strongly correlates with high-quality revivals. Finally, while the harmonic spacing of the Ritz values is needed to produce revivals, it appears to trade off with increased line width. As a consequence, optimising for harmonic energy spacing fares comparatively poorly in terms of return probability and the other figures of merit. In conclusion, being able to generate a low-dimensional, almost H -invariant subspace appears to be the most important factor responsible for the oscillatory dynamics in the fidelity.

6.6 Toy model and eigenstate embedding

Our results are part of a rapidly developing field of anomalous thermalisation. Here we will discuss some of these other developments and how they might relate to our results on the PXP model. The predictions of eigenstate thermalisation are widely (161) expected to hold for all eigenstates at finite energy density and in the limit of large systems under the following conditions: (i) Absence of local conserved quantities, (ii) Short-range interactions, (iii) Translation invariance. In support of this, exceptions to eigenstate thermalisation are typically found to violate these conditions. Integrable systems have local conserved quantities and thermalise to a generalised Gibbs' ensemble (172) and do not satisfy the ETH. Anderson and many-body localised systems also have local conserved quantities beside not satisfying translation invariance. The challenge is to find exceptions to the canonical thermalisation without violating these preconditions.

The idea of Ref. (153) is to “embed” non-thermal eigenstates corresponding to the (degenerate) ground states of frustration free models into the middle of an otherwise thermal spectrum. The construction starts from a family of local projection operators $\{P_i\}$ that are not assumed to commute with one another. These operators pick out a subspace \mathcal{T} which is their common nullspace, i.e.

$$P_i |\psi\rangle = 0, \quad (6.26)$$

for all i and $|\psi\rangle \in \mathcal{T}$. The subspace must be non-trivial. A Hamiltonian can then be constructed as

$$\hat{H} = \sum_i P_i h_i P_i + H', \quad (6.27)$$

where $[H', P_i] = 0$ for all i and the subspace \mathcal{T} is \hat{H} -invariant. The h_i are chosen under the conditions that $P_i h_i P_i$ is a local operator such that \hat{H} is short-range, but are otherwise arbitrary. It is not required that $[P_i, H]$ or even $[h_i, P_i]$ are necessarily equal to zero. Topological order is commonly studied in the form of frustration-free stabiliser models. In Ref. (121) this method was used to embed the degenerate ground states of topological phases into the middle of the spectrum.

6. ENHANCED QUANTUM REVIVAL AND EMERGENT SU(2) DYNAMICS

In Ref. (35), we introduced an example of this construction that closely resembles the PXP model. The model is of a chain of N spin-1/2 degrees of freedom. Define projectors

$$P_{i,j} = \frac{1}{4} (1 - X_i X_j - Y_i Y_j - Z_i Z_j) \quad (6.28)$$

which has a subspace invariant under exchange of site i and j as its nullspace. The n -th symmetric power of the spin-1/2 representation is the spin- $n/2$ representation. Hence the common nullspace of $P_{i,i+1}$ for $i = 1, \dots, N$ is this large spin representation, because the transpositions $(i, i+1)$ generates the symmetric group S_N . Using these we can produce a toy model,

$$H = \sum_j X_j + V_{j-1,j+2} P_{j,j+1} \quad (6.29)$$

where $V_{j-1,j+2}$ is a generic two-site operator supported on the sites $\{j-1, j+2\}$. Therefore, $V_{j-1,j+2}$ commutes with $P_{j,j+1}$ as they have non-overlapping support. The only relevant part of the Hamiltonian in the subspace is the $\sum_j X_j$ term, which in this subspace generates an X rotation of this large spin and produces equally spaced eigenvalues. All other terms act as the zero operator. This toy model demonstrates the key features we see in the PXP model. Perfect quantum revivals are obtained starting from either of the two eigenvectors of $\sum_j Z_j$ within this subspace, which are both unentangled states. These two initial states have mean energy zero, but by choice of the $V_{j-1,j+2}$ this can be made the middle of the spectrum, coexisting with the absolutely continuous spectrum. This example illustrates how one might obtain results similar to those we observed in the PXP model with and without perturbation by this method of embedding.

In another recent development, exact excited eigenstates were constructed in the AKLT model (115, 116) using a method known as the single-mode approximation (67). The single-mode approximation is an Ansatz formed by linear combinations of matrix-product states that are that of the ground state but with a single site tensor substituted. The AKLT model (4) is one of a family of frustration free stabiliser Hamiltonians built from projectors into particular spin representations. This includes the Majumdar-Gosh model (102) that was used to construct one of the examples in Ref. (153). The ground state stabilisers in

these models are spin projectors like those used in Equation (6.28) to construct our toy model.

In another recent work by Lin and Motrunich (100), an exact MPS eigenstate was found at zero energy in the PXP model, where the spectrum is highly degenerate, and in the case of open boundary conditions another two exact eigenstates were identified. These were close to the special eigenstates we identified, they were found at similar energies and also have anomalously large overlap with \mathbb{Z}_2 but are not the same states. They then proceeded to construct other states on top of these using the single-mode approximation but unlike in the work on the AKLT model these were found to be only approximate.

6.7 Conclusions

In this chapter we have shown how the intriguing non-equilibrium dynamics observed in the PXP model can be stabilised and enhanced by the addition of exponentially local corrections terms. The fidelity revivals can be tuned to within 10^{-6} of a perfect revival by numerical variation of the small number of parameters in the correction. Most strikingly the entanglement entropy growth over time is almost arrested. These terms act to produce a well-isolated subspace of special states as can be shown with the subspace variance. Concomitantly, the Ritz values in this subspace become equally spaced consistent with the fidelity oscillations. The special subspace can be identified using the forward-scattering ideas from the previous chapter suitably adapted to the addition terms in the Hamiltonian. The isolation of the subspace and harmonically spaced eigenvalues together forms a $SU(2)$ root system, with raising and lower operators given by the forward and backward propagating parts of the FSA Hamiltonian splitting. In more physical language the special subspace behaves as a precessing coherent large spin.

This produces a picture quite similar to a class of model considered by (153), which features a non-thermal subspace at finite energy-density despite generically being non-integrable. Finding any of the other eigenstates need be no easier than finding highly excited states of a completely chaotic system. From this we suggest that the behaviour of the original PXP model is due to proximity to a model with

6. ENHANCED QUANTUM REVIVAL AND EMERGENT SU(2) DYNAMICS

exponentially localised corrections. This model would then fall into the class of Ref. (153) and is non-integrable, but none the less violates the predictions of eigenstate thermalisation.

Chapter 7

Conclusions

In this thesis, we have focussed on the strange behaviour of the Rydberg atom chain in the limit of strong van der Waals forces, as revealed in a recent experiment (19). There it was found that, following certain quenches, coherent oscillatory dynamics could be observed in observables such as the domain wall density. We have demonstrated that the effective model for this problem displays an unconventional form of ergodicity breaking, where the dynamical approach to equilibrium is strongly dependent on the initial condition. The picture we have advanced is one of a small non-ergodic subspace of scarred eigenstates, hidden within an otherwise thermalising spectrum.

In Chapter 4, we showed the presence of strong quantum revivals where the entire wavefunction with good fidelity periodically recurs. The oscillations can also be seen in the entanglement entropy, where the rate of entanglement generation depends strongly on the initial state. The atypical dynamical behaviour can be attributed to the presence of a small number of atypical eigenstates embedded among the many typical eigenstates throughout the spectrum. These special states have anomalously large overlap with the \mathbb{Z}_2 Rydberg crystal state, approximately evenly spaced eigenvalues and greatly reduced entropy compared to typical states at their energy densities. This allows for some initial conditions to rapidly equilibrate, whilst others show persistent non-equilibrium properties.

Surprisingly, the model cannot be included within the existing classifications of non-thermal quantum systems, as evidenced by the level statistics. Explicitly, this rules out strong ergodicity breaking such as integrability and many-body

7. CONCLUSIONS

localisation. However, the special states also form violations of conventional ideas of eigenstate thermalisation where each eigenstate ought to look typical for its energy density. Furthermore, in the remainder of the eigenstates there are signs of anomalous thermalisation. In contrast to the detailed predictions of the eigenstate thermalisation hypothesis, there is no Thouless plateau and the matrix element fluctuations decay parametrically slower than the prediction. These findings show this model to be a very interesting system in which to explore quantum dynamics.

These findings we explained using a technique we call a forward-scattering approximation. This efficiently finds approximations to the eigenstates forming the scarred subspace. The Hamiltonian within this subspace is generated by a pair of raising and lower operators, H^+ and H^- . From this, we can interpret the subspace as a large spin, precessing about a constant field. This picture is approximate as the subspace is neither truly closed, nor are the matrix elements within in exactly those of an $SU(2)$ generator. This leads to the decay in the oscillations over long times. To make sense of these findings, we recalled the distinction between ergodicity and unique ergodicity from single-particle quantum chaos (71). A quantum system can be quantum ergodic but not quantum unique ergodic when it has a small number of exceptional eigenstates, these are then referred to as a *quantum scar*. The approximately closed subspace could be considered analogous to the bouncing ball quasi-modes of the Bunimovich stadium, which were an important step in proving the existence of this single-particle quantum scar.

Next, we showed that the scarred subspace can be enhanced by addition of an exponentially local perturbation, while the complementary subspace remains thermal. In this way, the fidelity revivals can be tuned to within 10^{-6} of a perfect revival. Most strikingly, the growth in entanglement is nearly arrested. Once again a forward-scattering subspace can be identified, which becomes almost exactly closed under the dynamics. The forward-scattering subspace and the scarred subspace then almost exactly coincide, and the algebra within the space is essentially that of $\mathfrak{su}(2)$, giving its interpretation as a large spin subspace.

A common hypothesis is that the quantum scar could be an effect due to proximity to integrability (86), like the phenomena of prethermalisation (22). This

would rely on some hitherto unknown realisation of an integrable system perturbatively close to the PXP model. The entire Hilbert space would presumably become strongly non-ergodic sufficiently close to this purported integrable point. In the opposite direction, there would be some mechanism such that some eigenstates of this integrable point are less sensitive to the integrability breaking and leave behind a remnant of special eigenstates. The evidence for this hypothesis is mixed. While in Ref. (86) it was found that level repulsion, a key indicator of non-integrability, could be suppressed by the addition of a perturbation, we found in Ref. (35) that the usual dynamical properties could be improved by moving in the other direction.

As we noted in Chapter 6, the scarred subspace picture is compatible with a family of models recently devised with the construction of Ref. (153). These are non-integrable and qualify as quantum scarred models. They are constructed from frustration-free Hamiltonians, which provides an additional symmetry operator to separate the special eigenstates from the typical ones. Recent work has suggested a connection between the PXP model and the AKLT model of this form (152).

Another approach taken to the description of the usual dynamics in this system is the time dependent variational principle for matrix product (65, 66). The original variational Ansatz takes coherent states distinguishing only even and odd sites, and projects into the subspace which satisfies the constraints (19, 74). The classical phase space for these equations of motion features a stable periodic orbit, on which the initial Rydberg crystal states lie. The Lyapunov exponents (68) for this classical dynamical system vanish on this trajectory. At each point along a trajectory, an error is made in the variational approximation, which geometrically is the extent that the quantum dynamics points out of the manifold. The other trajectories in the phase space are drawn towards a fixed point where the error grows as the quantum evolution flow becomes perpendicular to the variational manifold. A hypothesis offered up in this line of research is that the periodic orbit in the variational manifold is a counterpart to the periodic orbits in classical billiard systems, which can ultimately lead to a single-particle quantum scar (74, 111). These TDVP methods have been extended to find additional weakly-entangled initial states with regular dynamics (111), and generalisations

7. CONCLUSIONS

to high-spin models (27, 74). Another interesting finding is the appearance of mixed phase space, where some regions are regular and toroidal whilst others are chaotic, in this system, and others beside (111).

There are many open directions around the PXP model. An important one is the ultimate fate in the thermodynamic limit: both dynamically and in eigenstate properties. This is a challenging problem for numerics which can often only see finite sizes, and probably too difficult to answer conclusively without an exact theory. At larger sizes, it might be that what is currently individual eigenstates might melt into those states close by in energy. It appears that the effective number of eigenstates that would share the quasi-mode character must be very small, at least compared to the exponential number required to dilute it enough to hide below the ETH fluctuations. This is similar to the spirit of single-particle quantum scars where the quasi-modes are concentrated into a small number of eigenfunctions. Otherwise, it would be very strange that, even when the density of states has become very large, it has not already occurred. Of course, with the exponential density of states, there is some principle which suppresses mixing with other eigenstates.

The PXP model has a wide variety of different presentations in one dimension: Rydberg atoms, dimers on a ladder, monomer-dimer models on the line and Fibonacci anyons. These all suggest different generalisations to two dimensions. For example, there has recently been great progress in the quantum simulation of lattice gauge theory (149). Lattice gauge theories are another setting in which constrained Hilbert spaces naturally arise. It seems reasonable to expect experiment similar to the one reported in Ref. (19) on 2D Rydberg atom lattices in the near future. After all, the experiment on the Rydberg chain was done by preparing many chains in parallel. It will be interesting to see how dimensionality, Hilbert space constraints and symmetries are important in the quantum scar. The ground space subspaces found in topologically protected spaces and their manipulation form the basis for topological quantum computation (123). It would be interesting to consider how the scarred subspace could be of use in a quantum information protocol.

More generally the outlook for future progress in our understanding of quantum dynamics is promising. With the growing capability of quantum simulation

experiments, we can expect that the many-body quantum scar is only one of the first surprises in quantum dynamics to be uncovered. May there be many more to come.

7. CONCLUSIONS

Bibliography

- [1] Abanin, D., De Roeck, W., Ho, W. W., and Huveneers, F. (2017). A Rigorous Theory of Many-Body Prethermalization for Periodically Driven and Closed Quantum Systems. *Communications in Mathematical Physics*, 354(3):809–827. 54
- [2] Abanin, D. A., Altman, E., Bloch, I., and Serbyn, M. (2019). Colloquium: Many-body localization, thermalization, and entanglement. *Reviews of Modern Physics*, 91(2):168. 2, 17
- [3] Abanin, D. A., De Roeck, W., and Huveneers, F. (2015). Exponentially Slow Heating in Periodically Driven Many-Body Systems. *Physical Review Letters*, 115(25):128150. 48, 52
- [4] Affleck, I., Kennedy, T., Lieb, E. H., and Tasaki, H. (1987). Rigorous results on valence-bond ground states in antiferromagnets. *Physical Review Letters*, 59(7):799–802. 102
- [5] Alba, V. (2015). Eigenstate thermalization hypothesis and integrability in quantum spin chains. *Physical Review B*, 91(1):155123. 21, 46, 49
- [6] Alba, V. and Calabrese, P. (2018). Entanglement dynamics after quantum quenches in generic integrable systems. *SciPost Physics*, 4:017. 21
- [7] Alba, V., Haque, M., and Läuchli, A. M. (2012). Entanglement spectrum of the Heisenberg XXZ chain near the ferromagnetic point. *Journal of Statistical Mechanics: Theory and Experiment*, 2012(08):P08011. 23
- [8] Alicea, J. and Fendley, P. (2016). Topological Phases with Parafermions: Theory and Blueprints. *Annual Review of Condensed Matter Physics*, 7(1):119–139. 27
- [9] Alt, H., Gräf, H. D., Harney, H. L., Hofferbert, R., Lengeler, H., Richter, A., Schardt, P., and Weidenmüller, H. A. (1995). Gaussian Orthogonal Ensemble Statistics in a Microwave Stadium Billiard with Chaotic Dynamics:

BIBLIOGRAPHY

- Porter-Thomas Distribution and Algebraic Decay of Time Correlations. *Physical Review Letters*, 74(1):62–65. 16
- [10] Anderson, P. W. (1958). Absence of Diffusion in Certain Random Lattices. *Physical Review*, 109(5):1492–1505. 17
- [11] Andrews, G. E., Baxter, R. J., and Forrester, P. J. (1984). Eight-vertex SOS model and generalized Rogers-Ramanujan-type identities. *Journal of Statistical Physics*, 35(3):193–266. 42
- [12] Arnol'd, V. I. (1997). *Mathematical Methods of Classical Mechanics*. Springer. 16
- [13] Babelon, O., Bernard, D., and Talon, M. (2009). *Introduction to Classical Integrable Systems*. Cambridge University Press, Cambridge. 16
- [14] Bardarson, J. H., Pollmann, F., and Moore, J. E. (2012). Unbounded Growth of Entanglement in Models of Many-Body Localization. *Physical Review Letters*, 109(1):017202. ix, 17, 22, 49
- [15] Barnett, A. (2006). Asymptotic rate of quantum ergodicity in chaotic Euclidean billiards. *Communications on Pure and Applied Mathematics*, 59(10):1457–1488. 6
- [16] Barredo, D., de Léséleuc, S., Lienhard, V., Lahaye, T., and Browaeys, A. (2016). An atom-by-atom assembler of defect-free arbitrary two-dimensional atomic arrays. *Science*, 354(6315):1021–1023. 33
- [17] Bauer, B. and Nayak, C. (2013). Area laws in a many-body localized state and its implications for topological order. *Journal of Statistical Mechanics: Theory and Experiment*, 2013(09):P09005. 17, 21
- [18] Baxter, R. J. (1982). *Exactly Solved Models in Statistical Mechanics*. Academic Press, London. 17, 27
- [19] Bernien, H., Schwartz, S., Keesling, A., Levine, H., Omran, A., Pichler, H., Choi, S., Zibrov, A. S., Endres, M., Greiner, M., Vuletić, V., and Lukin, M. D. (2017). Probing many-body dynamics on a 51-atom quantum simulator. *Nature*, 551(7682):579–584. 2, 3, 31, 33, 34, 35, 38, 50, 57, 83, 105, 107, 108
- [20] Berry, M. V. (1977). Regular and irregular semiclassical wavefunctions. *Journal of Physics A: Mathematical and General*, 10(12):2083–2091. 8

- [21] Berry, M. V. and Tabor, M. (1977). Level Clustering in the Regular Spectrum. *Proceedings of the Royal Society A: Mathematical, Physical and Engineering Sciences*, 356(1686):375–394. 14, 17, 42, 44
- [22] Bertini, B., Essler, F. H. L., Groha, S., and Robinson, N. J. (2015). Prethermalization and Thermalization in Models with Weak Integrability Breaking. *Physical Review Letters*, 115(18):180601. 58, 106
- [23] Bocchieri, P. and Loinger, A. (1957). Quantum Recurrence Theorem. *Physical Review*, 107(2):337–338. 11, 38
- [24] Bohigas, O., Giannoni, M. J., and Schmit, C. (1984). Characterization of Chaotic Quantum Spectra and Universality of Level Fluctuation Laws. *Physical Review Letters*, 52(1):1–4. 16
- [25] Bordia, P., Lüschen, H. P., Hodgman, S. S., Schreiber, M., Bloch, I., and Schneider, U. (2016). Coupling Identical one-dimensional Many-Body Localized Systems. *Physical Review Letters*, 116(14):140401. 2
- [26] Bravyi, S., DiVincenzo, D. P., and Loss, D. (2011). Schrieffer–Wolff transformation for quantum many-body systems. *Annals of Physics*, 326(10):2793–2826. 51
- [27] Bull, K., Martin, I., and Papić, Z. (2019). Systematic construction of scarred many-body dynamics in 1D lattice models. *arxiv.org*. 27, 108
- [28] Bunimovich, L. A. (1979). On the ergodic properties of nowhere dispersing billiards. *Communications in Mathematical Physics*, 65(3):295–312. 6, 7
- [29] Calabrese, P. and Cardy, J. (2004). Entanglement entropy and quantum field theory. *Journal of Statistical Mechanics: Theory and Experiment*, 2004(06):P06002. 21, 65
- [30] Calabrese, P. and Cardy, J. (2009). Entanglement entropy and conformal field theory. *Journal of Physics A: Mathematical and Theoretical*, 42(50):504005. 21
- [31] Calabrese, P. and Lefevre, A. (2008). Entanglement spectrum in one-dimensional systems. *Physical Review A*, 78(3):032329–4. 23
- [32] Calzona, A., Meng, T., Sasseti, M., and Schmidt, T. L. (2018). \mathbb{Z}_4 parafermions in one-dimensional fermionic lattices. *Physical Review B*, 98(20):201110. 30

BIBLIOGRAPHY

- [33] Chandran, A., Schulz, M. D., and Burnell, F. J. (2016). The eigenstate thermalization hypothesis in constrained Hilbert spaces: A case study in non-Abelian anyon chains. *Physical Review B*, 94(23):235122. 46
- [34] Choi, J. y., Hild, S., Zeiher, J., Schauss, P., Rubio-Abadal, A., Yefsah, T., Khemani, V., Huse, D. A., Bloch, I., and Gross, C. (2016). Exploring the many-body localization transition in two dimensions. *Science*, 352(6293):1547–1552. 2
- [35] Choi, S., Turner, C. J., Pichler, H., Ho, W. W., Michailidis, A. A., Papić, Z., Serbyn, M., Lukin, M. D., and Abanin, D. A. (2018). Emergent SU(2) dynamics and perfect quantum many-body scars. *arxiv.org*. 3, 85, 102, 107
- [36] Clarke, D. J., Alicea, J., and Shtengel, K. (2014). Exotic circuit elements from zero-modes in hybrid superconductor/quantum Hall systems. *Nature Physics*, 10(11):877–882. 27
- [37] Collatz, L. (1942). Einschließungssatz für die charakteristischen zahlen von matrizen. *Mathematische Zeitschrift*, 48(1):221–226. 80
- [38] Collin, D., Ritort, F., Jarzynski, C., Smith, S. B., Tinoco, I., and Bustamante, C. (2005). Verification of the Crooks fluctuation theorem and recovery of RNA folding free energies. *Nature*, 437(7056):231–234. 11
- [39] Cong, B., Zheng, S. Q., and Sharma, S. (1993). On simulations of linear arrays, rings and 2D meshes on Fibonacci cube networks. In *[1993] Seventh International Parallel Processing Symposium*, pages 748–751. IEEE Comput. Soc. Press. 60
- [40] Crooks, G. E. (1999). Entropy production fluctuation theorem and the nonequilibrium work relation for free energy differences. *Physical Review E*, 60(3):2721–2726. 11
- [41] D’Alessio, L., Kafri, Y., Polkovnikov, A., and Rigol, M. (2016). From quantum chaos and eigenstate thermalization to statistical mechanics and thermodynamics. *Advances in Physics*, 65(3):239–362. 2, 5, 13, 44, 48
- [42] de Verdiere, Y. C. (1985). Ergodicité et fonctions propres du laplacien. *Communications in Mathematical Physics*, 102(3):497–502. 9
- [43] Deutsch, D. and Jozsa, R. (1992). Rapid Solution of Problems by Quantum Computation. *Proceedings of the Royal Society A: Mathematical, Physical and Engineering Sciences*, 439(1907):553–558. 1

- [44] Deutsch, J. M. (1991). Quantum statistical mechanics in a closed system. *Physical Review A*, 43(4):2046–2049. 13, 44
- [45] Dyson, F. J. (1962). Statistical Theory of the Energy Levels of Complex Systems. I. *Journal of Mathematical Physics*, 3(1):140–156. 12
- [46] Edwards, J. T. and Thouless, D. J. (2001). Numerical studies of localization in disordered systems. *Journal of Physics C: Solid State Physics*, 5(8):807–820. 14, 48
- [47] Else, D. V., Fendley, P., Kemp, J., and Nayak, C. (2017). Prethermal Strong Zero Modes and Topological Qubits. *Physical Review X*, 7(4):09005. 54
- [48] Endres, M., Bernien, H., Keesling, A., Levine, H., Anschuetz, E. R., Krajenbrink, A., Senko, C., Vuletić, V., Greiner, M., and Lukin, M. D. (2016). Atom-by-atom assembly of defect-free one-dimensional cold atom arrays. *Science*, 354(6315):1024–1027. 33
- [49] Feiguin, A., Trebst, S., Ludwig, A. W. W., Troyer, M., Kitaev, A. Y., Wang, Z., and Freedman, M. H. (2007). Interacting Anyons in Topological Quantum Liquids: The Golden Chain. *Physical Review Letters*, 98(16):30. 42, 46, 50, 56
- [50] Fendley, P. (2012). Parafermionic edge zero modes in Zn-invariant spin chains. *Journal of Statistical Mechanics: Theory and Experiment*, 2012(11):P11020. 27
- [51] Fendley, P., Sengupta, K., and Sachdev, S. (2004). Competing density-wave orders in a one-dimensional hard-boson model. *Physical Review B*, 69(7):075128–15. ix, 33, 34, 42, 50, 56
- [52] Fidkowski, L. (2010). Entanglement Spectrum of Topological Insulators and Superconductors. *Physical Review Letters*, 104(13):130502. 23
- [53] Fidkowski, L. and Kitaev, A. Y. (2011). Topological phases of fermions in one dimension. *Physical Review B*, 83(7):075103. 23
- [54] Fradkin, E. and Kadanoff, L. P. (1980). Disorder variables and para-fermions in two-dimensional statistical mechanics. *Nuclear Physics*, 170(1):1–15. 27
- [55] Fuchs, C. A. and van de Graaf, J. (1999). Cryptographic distinguishability measures for quantum-mechanical states. *IEEE Transactions on Information Theory*, 45(4):1216–1227. 25
- [56] Garrison, J. R. and Grover, T. (2018). Does a Single Eigenstate Encode the Full Hamiltonian? *Physical Review X*, 8(2):348. 14, 21

BIBLIOGRAPHY

- [57] Genoni, M. G., Paris, M. G. A., and Banaszek, K. (2007). Measure of the non-Gaussian character of a quantum state. *Physical Review A*, 76(4):042327. 25
- [58] Genoni, M. G., Paris, M. G. A., and Banaszek, K. (2008). Quantifying the non-Gaussian character of a quantum state by quantum relative entropy. *Physical Review A*, 78(6):060303. 25
- [59] Gérard, P. and Leichtnam, E. (1993). Ergodic properties of eigenfunctions for the Dirichlet problem. *Duke Mathematical Journal*, 71(2):559–607. 9
- [60] Gertis, J., Friesdorf, M., Riofrio, C. A., and Eisert, J. (2016). Estimating strong correlations in optical lattices. *Physical Review A*, 94(5):053628. 25
- [61] Godsil, C. (2008). Periodic Graphs. *arxiv.org*. 39
- [62] Goldstein, S., Lebowitz, J. L., Tumulka, R., and Zanghi, N. (2006). Canonical Typicality. *Physical Review Letters*, 96(5):956. 12
- [63] Goldstein, S., Lebowitz, J. L., Tumulka, R., and Zanghi, N. (2010). Long-time behavior of macroscopic quantum systems. *The European Physical Journal H*, 35(2):173–200. 12
- [64] Gottesman, D. (1998). Theory of fault-tolerant quantum computation. *Physical Review A*, 57(1):127–137. 1
- [65] Haegeman, J., Cirac, J. I., Osborne, T. J., Pizorn, I., Verschelde, H., and Verstraete, F. (2011). Time-Dependent Variational Principle for Quantum Lattices. *Physical Review Letters*, 107(7):070601. 107
- [66] Haegeman, J., Lubich, C., Oseledets, I., Vandereycken, B., and Verstraete, F. (2016). Unifying time evolution and optimization with matrix product states. *Physical Review B*, 94(16):165116. 107
- [67] Haegeman, J., Michalakis, S., Nachtergaele, B., Osborne, T. J., Schuch, N., and Verstraete, F. (2013). Elementary Excitations in Gapped Quantum Spin Systems. *Physical Review Letters*, 111(8):1058. 102
- [68] Hallam, A., Morley, J., and Green, A. G. (2018). The Lyapunov Spectrum of Quantum Thermalisation. *arxiv.org*. 107
- [69] Hasan, M. Z. and Kane, C. L. (2010). Colloquium: Topological insulators. *Reviews of Modern Physics*, 82(4):3045–3067. 16, 23

- [70] Hassell, A. (2010). Ergodic billiards that are not quantum unique ergodic. *Annals of Mathematics*, 171(1):605–618. 9, 10
- [71] Hassell, A. (2011). What is quantum unique ergodicity? *Australian Mathematical Society Gazette*. 2, 5, 6, 8, 106
- [72] Hastings, M. B. (2007). An area law for one-dimensional quantum systems. *Journal of Statistical Mechanics: Theory and Experiment*, 2007(08):P08024–P08024. 21
- [73] Heller, E. J. (1984). Bound-State Eigenfunctions of Classically Chaotic Hamiltonian Systems: Scars of Periodic Orbits. *Physical Review Letters*, 53(16):1515–1518. 9, 10
- [74] Ho, W. W., Choi, S., Pichler, H., and Lukin, M. D. (2019). Periodic Orbits, Entanglement, and Quantum Many-Body Scars in Constrained Models: Matrix Product State Approach. *Physical Review Letters*, 122(4):040603. 107, 108
- [75] Horn, R. A. and Johnson, C. R. (1990). *Matrix Analysis*. Cambridge University Press. 25
- [76] Hsu, W. J. (1993). Fibonacci cubes—a new interconnection Topology. *IEEE Transactions on Parallel and Distributed Systems*, 4(1):3–12. 60
- [77] Hubbard, J. (1963). Electron Correlations in Narrow Energy Bands. In *Proceedings of the Royal Society of London. Series A*, pages 238–257. 17
- [78] Huse, D. A., Nandkishore, R., and Oganesyan, V. (2014). Phenomenology of fully many-body-localized systems. *Physical Review B*, 90(17):174202. 17
- [79] Iadecola, T., Schechter, M., and Xu, S. (2019). Quantum Many-Body Scars and Space-Time Crystalline Order from Magnon Condensation. *arxiv.org*. 56
- [80] Isenhower, L., Urban, E., Zhang, X. L., Gill, A. T., Henage, T., Johnson, T. A., Walker, T. G., and Saffman, M. (2010). Demonstration of a Neutral Atom Controlled-NOT Quantum Gate. *Physical Review Letters*, 104(1):010502. 32
- [81] Islam, R., Senko, C., Campbell, W. C., Korenblit, S., Smith, J., Lee, A., Edwards, E. E., Wang, C. C. J., Freericks, J. K., and Monroe, C. (2013). Emergence and Frustration of Magnetism with Variable-Range Interactions in a Quantum Simulator. *Science*, 340(6132):583–587. 2

BIBLIOGRAPHY

- [82] Jaksch, D., Cirac, J. I., Zoller, P., Rolston, S. L., Côté, R., and Lukin, M. D. (2000). Fast Quantum Gates for Neutral Atoms. *Physical Review Letters*, 85(10):2208–2211. 2, 32
- [83] Jarzynski, C. (1997). Nonequilibrium Equality for Free Energy Differences. *Physical Review Letters*, 78(14):2690–2693. 11
- [84] Keesling, A., Omran, A., Levine, H., Bernien, H., Pichler, H., Choi, S., Smaajdar, R., Schwartz, S., Silvi, P., Sachdev, S., Zoller, P., Endres, M., Greiner, M., Vuletić, V., and Lukin, M. D. (2019). Quantum Kibble–Zurek mechanism and critical dynamics on a programmable Rydberg simulator. *Nature*, 568(7751):207–211. 27
- [85] Khatami, E., Pupillo, G., Srednicki, M., and Rigol, M. (2013). Fluctuation-Dissipation Theorem in an Isolated System of Quantum Dipolar Bosons after a Quench. *Physical Review Letters*, 111(5):050403. 13, 14
- [86] Khemani, V., Laumann, C. R., and Chandran, A. (2018). Signatures of integrability in the dynamics of Rydberg-blockaded chains. *arxiv.org*. 85, 86, 87, 93, 106, 107
- [87] Kim, H. and Huse, D. A. (2013). Ballistic Spreading of Entanglement in a Diffusive Nonintegrable System. *Physical Review Letters*, 111(12):127205. 21
- [88] Kim, H., Ikeda, T. N., and Huse, D. A. (2014). Testing whether all eigenstates obey the eigenstate thermalization hypothesis. *Physical Review E*, 90(5):181. 46
- [89] Kim, H., Lee, W., Lee, H.-g., Jo, H., Song, Y., and Ahn, J. (2016). In situ single-atom array synthesis using dynamic holographic optical tweezers. *Nature Communications*, 7(1):1024. 33
- [90] Kitaev, A. Y. (2001). Unpaired Majorana fermions in quantum wires. *Phys. Usp.*, 44(10S):131–136. 26
- [91] Klavžar, S. (2005). On median nature and enumerative properties of Fibonacci-like cubes. *Discrete Mathematics*, 299(1-3):145–153. 60
- [92] Klavžar, S. (2011). Structure of Fibonacci cubes: a survey. *Journal of Combinatorial Optimization*, 25(4):505–522. 60, 64
- [93] Kota, V. K. B. (2014). *Embedded Random Matrix Ensembles in Quantum Physics*, volume 884 of *Lecture Notes in Physics*. Springer International Publishing, Cham. 14, 48

- [94] Kramer, B. and MacKinnon, A. (1999). Localization: theory and experiment. *Reports on Progress in Physics*, 56(12):1469–1564. 44
- [95] Kreĭn, M. G. and Rutman, M. A. (1948). Linear operators leaving invariant a cone in a Banach space. *Usp. Mat. Nauk*, 3(1(23)):3–95. 81
- [96] Lanczos, C. (1950). An iteration method for the solution of the eigenvalue problem of linear differential and integral operators. *Journal of Research of the National Bureau of Standards*, 45(4):255. 60
- [97] Laughlin, R. (1981). Quantized Hall conductivity in two dimensions. *Physical Review B*, 23(10):5632–5633. 16
- [98] Lesanovsky, I. (2012). Liquid Ground State, Gap, and Excited States of a Strongly Correlated Spin Chain. *Physical Review Letters*, 108(10):105301. 50, 56
- [99] Li, H. and Haldane, F. (2008). Entanglement Spectrum as a Generalization of Entanglement Entropy: Identification of Topological Order in Non-Abelian Fractional Quantum Hall Effect States. *Physical Review Letters*, 101(1):010504–4. 19, 22, 23
- [100] Lin, C.-J. and Motrunich, O. I. (2018). Exact Strong-ETH Violating Eigenstates in the Rydberg-blockaded Atom Chain. *arxiv.org*. 103
- [101] Lloyd, S. (1996). Universal Quantum Simulators. *Science*, 273(5278):1073–1078. 1
- [102] Majumdar, C. K. and Ghosh, D. K. (1969). On Next-Nearest-Neighbor Interaction in Linear Chain. I. *Journal of Mathematical Physics*, 10(8):1388–1398. 102
- [103] Marčenko, V. A. and Pastur, L. A. (2007). Distribution of Eigenvalues for Some Sets of Random Matrices. *Mathematics of the USSR-Sbornik*, 1(4):457–483. 23
- [104] Marian, P. and Marian, T. A. (2013). Relative entropy is an exact measure of non-Gaussianity. *Physical Review A*, 88(1):012322. 25
- [105] Markham, D., Miszczak, J. A., Puchała, Z., and Życzkowski, K. (2008). Quantum state discrimination: A geometric approach. *Physical Review A*, 77(4):042111. 25

BIBLIOGRAPHY

- [106] Mazurenko, A., Chiu, C. S., Ji, G., Parsons, M. F., Kanász-Nagy, M., Schmidt, R., Grusdt, F., Demler, E., Greif, D., and Greiner, M. (2017). A cold-atom Fermi–Hubbard antiferromagnet. *Nature*, 545(7655):462–466. 2
- [107] McMahon, P. L., Marandi, A., Haribara, Y., Hamerly, R., Langrock, C., Tamate, S., Inagaki, T., Takesue, H., Utsunomiya, S., Aihara, K., Byer, R. L., Fejer, M. M., Mabuchi, H., and Yamamoto, Y. (2016). A fully programmable 100-spin coherent Ising machine with all-to-all connections. *Science*, 354(6312):614–617. 2
- [108] Mehta, M. L. (2004). *Random Matrices*. Elsevier. 12
- [109] Meichanetzidis, K., Turner, C. J., Farjami, A., Papić, Z., and Pachos, J. K. (2018). Free-fermion descriptions of parafermion chains and string-net models. *Physical Review B*, 97(12):125104. 2, 19, 27, 28
- [110] Meyer, C. (2000). *Matrix Analysis and Applied Linear Algebra*. Other Titles in Applied Mathematics. SIAM. 80
- [111] Michailidis, A. A., Turner, C. J., Abanin, D. A., and Serbyn, M. (2019). Slow quantum thermalization and many-body revivals from mixed phase space. *arXiv.org*. 21, 107, 108
- [112] Mong, R. S. K., Clarke, D. J., Alicea, J., Lindner, N. H., Fendley, P., Nayak, C., Oreg, Y., Stern, A., Berg, E., Shtengel, K., and Fisher, M. P. A. (2014). Universal Topological Quantum Computation from a Superconductor-Abelian Quantum Hall Heterostructure. *Physical Review X*, 4(1):011036. 27
- [113] Monz, T., Schindler, P., Barreiro, J. T., Chwalla, M., Nigg, D., Coish, W. A., Harlander, M., Hänsel, W., Hennrich, M., and Blatt, R. (2011). 14-Qubit Entanglement: Creation and Coherence. *Physical Review Letters*, 106(13):130506. 2
- [114] Motruk, J., Berg, E., Turner, A. M., and Pollmann, F. (2013). Topological phases in gapped edges of fractionalized systems. *Physical Review B*, 88(8):085115. 27
- [115] Moudgalya, S., Rachel, S., Bernevig, B. A., and Regnault, N. (2017). Exact Excited States of Non-Integrable Models. *arxiv.org*. 102
- [116] Moudgalya, S., Regnault, N., and Bernevig, B. A. (2018). Entanglement of exact excited states of Affleck-Kennedy-Lieb-Tasaki models: Exact results, many-body scars, and violation of the strong eigenstate thermalization hypothesis. *Physical Review B*, 98(23):401. 65, 102

BIBLIOGRAPHY

- [117] Mukerjee, S., Oganesyan, V., and Huse, D. (2006). Statistical theory of transport by strongly interacting lattice fermions. *Physical Review B*, 73(3):1394. 48
- [118] Nielsen, M. A. and Chuang, I. L. (2000). *Quantum Computation and Quantum Information*. Cambridge University Press. 19, 20, 24, 25
- [119] O'Connor, P. W. and Heller, E. J. (1988). Quantum Localization for a Strongly Classically Chaotic System. *Physical Review Letters*, 61(20):2288–2291. 9
- [120] Oganesyan, V. and Huse, D. A. (2007). Localization of interacting fermions at high temperature. *Physical Review B*, 75(15):155111. 43
- [121] Ok, S., Choo, K., Mudry, C., Castelnovo, C., Chamon, C., and Neupert, T. (2019). Topological many-body scar states in dimensions 1, 2, and 3. *arxiv.org*. 101
- [122] Orús, R. (2014). A practical introduction to tensor networks: Matrix product states and projected entangled pair states. *Annals of Physics*, 349:117–158. 71
- [123] Pachos, J. K. (2012). *Introduction to Topological Quantum Computation*. Cambridge University Press. 1, 108
- [124] Page, D. N. (1993). Average entropy of a subsystem. *Physical Review Letters*, 71(9):1291–1294. 21
- [125] Pal, A. and Huse, D. A. (2010). Many-body localization phase transition. *Physical Review B*, 82(17):174411. 14, 16, 17, 42
- [126] Pandey, A. and Ramaswamy, R. (1991). Level spacings for harmonic-oscillator systems. *Physical Review A*, 43(8):4237–4243. 17
- [127] Peschel, I. (2003). Calculation of reduced density matrices from correlation functions. *Journal of Physics A: Mathematical and General*, 36(14):L205–L208. 25, 26
- [128] Petersen, K. E. (1983). *Ergodic Theory*. Cambridge Studies in Advanced Mathematics. Cambridge University Press. 7
- [129] Pohl, T., Demler, E., and Lukin, M. D. (2009). Dynamical Crystallization in the Dipole Blockade of Ultracold Atoms. *arxiv.org*, (4):043002. ix, 33, 34

BIBLIOGRAPHY

- [130] Preskill, J. (2018). Quantum Computing in the NISQ era and beyond. *Quantum*, 2:79. 1
- [131] Rigol, M. (2009a). Breakdown of Thermalization in Finite One-Dimensional Systems. *Physical Review Letters*, 103(10):015101. 14, 46
- [132] Rigol, M. (2009b). Quantum quenches and thermalization in one-dimensional fermionic systems. *Physical Review A*, 80(5):053607. 14, 46
- [133] Rigol, M., Dunjko, V., and Olshanii, M. (2008). Thermalization and its mechanism for generic isolated quantum systems. *Nature*, 452(7189):854–858. 44
- [134] Rigol, M. and Srednicki, M. (2012). Alternatives to Eigenstate Thermalization. *Physical Review Letters*, 108(11):181. 12
- [135] Ritort, F. and Sollich, P. (2003). Glassy dynamics of kinetically constrained models. *Advances in Physics*, 52(4):219–342. 11
- [136] Robinett, R. (2004). Quantum wave packet revivals. *Physics Reports*, 392(1-2):1–119. 38
- [137] Ronnow, T. F., Wang, Z., Job, J., Boixo, S., Isakov, S. V., Wecker, D., Martinis, J. M., Lidar, D. A., and Troyer, M. (2014). Defining and detecting quantum speedup. *Science*, 345(6195):420–424. 2
- [138] Rudnick, Z. and Sarnak, P. (1994). The behaviour of eigenstates of arithmetic hyperbolic manifolds. *Communications in Mathematical Physics*, 161(1):195–213. 9
- [139] Saffman, M. (2016). Quantum computing with atomic qubits and Rydberg interactions: progress and challenges. *Journal of Physics B: Atomic, Molecular and Optical Physics*, 49(20):202001. 32
- [140] Samajdar, R., Choi, S., Pichler, H., Lukin, M. D., and Sachdev, S. (2018). Numerical study of the chiral Z₃ quantum phase transition in one spatial dimension. *Physical Review A*, 98(2):1151. 56
- [141] Santos, L. F., Polkovnikov, A., and Rigol, M. (2012). Weak and strong typicality in quantum systems. *Physical Review E*, 86(1):010102. 21
- [142] Santos, L. F. and Rigol, M. (2010a). Localization and the effects of symmetries in the thermalization properties of one-dimensional quantum systems. *Physical Review E*, 82(3):031130. 16

- [143] Santos, L. F. and Rigol, M. (2010b). Onset of quantum chaos in one-dimensional bosonic and fermionic systems and its relation to thermalization. *Physical Review E*, 81(3):036206. 16
- [144] Sato, J., Aufgebauer, B., Boos, H., Göhmann, F., Klümper, A., Takahashi, M., and Trippe, C. (2011). Computation of Static Heisenberg-Chain Correlators: Control over Length and Temperature Dependence. *Physical Review Letters*, 106(25):593. 21, 49
- [145] Schecter, M. and Iadecola, T. (2018). Many-body spectral reflection symmetry and protected infinite-temperature degeneracy. *Physical Review B*, 98(3):035139. 43, 53
- [146] Schreiber, M., Hodgman, S. S., Bordia, P., Luschen, H. P., Fischer, M. H., Vosk, R., Altman, E., Schneider, U., and Bloch, I. (2015). Observation of many-body localization of interacting fermions in a quasirandom optical lattice. *Science*, 349(6250):842–845. 2
- [147] Schrieffer, J. R. and Wolff, P. A. (1966). Relation between the Anderson and Kondo Hamiltonians. *Physical Review*, 149(2):491–492. 51
- [148] Schultz, T. D., Mattis, D. C., and Lieb, E. H. (1964). Two-Dimensional Ising Model as a Soluble Problem of Many Fermions. *Reviews of Modern Physics*, 36(3):856–871. 26
- [149] Schweizer, C., Grusdt, F., Berngruber, M., Barbiero, L., Demler, E., Goldman, N., Bloch, I., and Aidelsburger, M. (2019). Floquet approach to \mathbf{Z}_2 lattice gauge theories with ultracold atoms in optical lattices. *arxiv.org*. 108
- [150] Serbyn, M., Michailidis, A. A., Abanin, D. A., and Papić, Z. (2016). Power-Law Entanglement Spectrum in Many-Body Localized Phases. *Physical Review Letters*, 117(16):160601. 23
- [151] Serbyn, M., Papić, Z., and Abanin, D. A. (2013). Local Conservation Laws and the Structure of the Many-Body Localized States. *Physical Review Letters*, 111(12):127201. 17, 21
- [152] Shiraishi, N. (2019). Connection between quantum-many-body scars and the AKLT model from the viewpoint of embedded Hamiltonians. *arXiv.org*. 107
- [153] Shiraishi, N. and Mori, T. (2017). Systematic Construction of Counterexamples to the Eigenstate Thermalization Hypothesis. *Physical Review Letters*, 119(3):201. 101, 102, 103, 104, 107

BIBLIOGRAPHY

- [154] Shnirel'man, A. I. (1974). Ergodic properties of eigenfunctions. *Russian Mathematical Surveys*, 29(6):181–182. 9
- [155] Shor, P. W. (1997). Polynomial-Time Algorithms for Prime Factorization and Discrete Logarithms on a Quantum Computer. *SIAM Journal on Computing*, 26(5):1484–1509. 1
- [156] Sinai, Y. G. (1970). Dynamical systems with elastic reflections. *Russian Mathematical Surveys*, 25(2):137–189. 6, 7
- [157] Song, C., Xu, K., Liu, W., Yang, C.-p., Zheng, S.-B., Deng, H., Xie, Q., Huang, K., Guo, Q., Zhang, L., Zhang, P., Xu, D., Zheng, D., Zhu, X., Wang, H., Chen, Y. A., Lu, C. Y., Han, S., and Pan, J.-W. (2017). 10-Qubit Entanglement and Parallel Logic Operations with a Superconducting Circuit. *Physical Review Letters*, 119(18):180511. 2
- [158] Srednicki, M. (1994). Chaos and quantum thermalization. *Physical Review E*, 50(2):888–901. 13
- [159] Srednicki, M. (1996). Thermal fluctuations in quantized chaotic systems. *Journal of Physics A: Mathematical and General*, 29(4):L75–L79. 13, 44
- [160] Srednicki, M. (1999). The approach to thermal equilibrium in quantized chaotic systems. *Journal of Physics A: Mathematical and General*, 32(7):1163–1175. 13
- [161] Srednicki, M. (2012). Overview of Eigenstate Thermalisation Hypothesis. <http://online.kitp.ucsb.edu/online/qdynamics12/srednicki/>. 101
- [162] Stanley, R. P. (2009). A Survey of Alternating Permutations. *arXiv.org*. 79
- [163] Stöckmann, H. J. and Stein, J. (1990). “Quantum” chaos in billiards studied by microwave absorption. *Physical Review Letters*, 64(19):2215–2218. 16
- [164] Sutherland, B. (2004). *Beautiful Models*. 70 Years of Exactly Solved Quantum Many-body Problems. World Scientific. 2, 17
- [165] Turner, A. M., Pollmann, F., and Berg, E. (2011). Topological phases of one-dimensional fermions: An entanglement point of view. *Physical Review B*, 83(7):075102. 23
- [166] Turner, C. J., Meichanetzidis, K., Papić, Z., and Pachos, J. K. (2017). Optimal free descriptions of many-body theories. *Nature Communications*, 8:ncomms14926. 2, 19, 24, 25, 26

- [167] Turner, C. J., Michailidis, A. A., Abanin, D. A., Serbyn, M., and Papić (2018a). Weak ergodicity breaking from quantum many-body scars. *Nature Physics*, 14(7):745–749. 3, 9, 21, 43, 53, 59
- [168] Turner, C. J., Michailidis, A. A., Abanin, D. A., Serbyn, M., and Papić, Z. (2018b). Quantum scarred eigenstates in a Rydberg atom chain: Entanglement, breakdown of thermalization, and stability to perturbations. *Physical Review B*, 98(15):12. 3, 43, 53, 56, 59, 66
- [169] Vasseur, R., Potter, A. C., and Parameswaran, S. A. (2015). Quantum Criticality of Hot Random Spin Chains. *Physical Review Letters*, 114(21):217201. 21
- [170] Vidal, G. (2007). Classical Simulation of Infinite-Size Quantum Lattice Systems in One Spatial Dimension. *Physical Review Letters*, 98(7):070201–4. 49
- [171] Vidal, G., Latorre, J. I., Rico, E., and Kitaev, A. (2003). Entanglement in Quantum Critical Phenomena. *Physical Review Letters*, 90(22):227902. 21, 65
- [172] Vidmar, L. and Rigol, M. (2016). Generalized Gibbs ensemble in integrable lattice models. *Journal of Statistical Mechanics: Theory and Experiment*, 2016(6):064007. 18, 101
- [173] von Neumann, J. (1929). Beweis des Ergodensatzes und des H-Theorems. *Zeitschrift für Physik*, 57:30–70. 12
- [174] Weedbrook, C., Pirandola, S., Garcia-Patron, R., Cerf, N. J., Ralph, T. C., Shapiro, J. H., and Lloyd, S. (2012). Gaussian quantum information. *Reviews of Modern Physics*, 84(2):621–669. 25
- [175] Weimer, H., Müller, M., Lesanovsky, I., Zoller, P., and Büchler, H. P. (2010). A Rydberg quantum simulator. *Nature Physics*, 6(5):382–388. 2, 32
- [176] Wigner, E. P. (1955). Characteristic Vectors of Bordered Matrices With Infinite Dimensions. *The Annals of Mathematics*, 62(3):548. 12, 15
- [177] Wigner, E. P. (1958). On the Distribution of the Roots of Certain Symmetric Matrices. *The Annals of Mathematics*, 67(2):325. 15
- [178] Wilk, T., Gaëtan, A., Evellin, C., Wolters, J., Miroshnychenko, Y., Grangier, P., and Browaeys, A. (2010). Entanglement of Two Individual Neutral Atoms Using Rydberg Blockade. *Physical Review Letters*, 104(1):010503. 32

BIBLIOGRAPHY

- [179] Wolf, M. M. (2006). Violation of the Entropic Area Law for Fermions. *Physical Review Letters*, 96(1):48. 21
- [180] Yang, Z.-C., Chamon, C., Hamma, A., and Mucciolo, E. R. (2015). Two-Component Structure in the Entanglement Spectrum of Highly Excited States. *Physical Review Letters*, 115(26):P09005. 23
- [181] You, Y.-Z., Qi, X.-L., and Xu, C. (2016). Entanglement holographic mapping of many-body localized system by spectrum bifurcation renormalization group. *Physical Review B*, 93(10):104205. 17
- [182] Zelditch, S. (1987). Uniform distribution of eigenfunctions on compact hyperbolic surfaces. *Duke Mathematical Journal*, 55(4):919–941. 9
- [183] Zelditch, S. (2004). Note on quantum unique ergodicity. *Proceedings of the American Mathematical Society*, 132(06):1869–1873. 9, 10
- [184] Zelditch, S. and Zworski, M. (1996). Ergodicity of Eigenfunctions for Ergodic Billiards. *Communications in Mathematical Physics*, 175(3):673–682. 9
- [185] Zhang, J., Pagano, G., Hess, P. W., Kyprianidis, A., Becker, P., Kaplan, H., Gorshkov, A. V., Gong, Z. X., and Monroe, C. (2017). Observation of a many-body dynamical phase transition with a 53-qubit quantum simulator. *Nature*, 551(7):601–604. 2
- [186] Znidaric, M., Prosen, T., and Prelovsek, P. (2008). Many-body localization in the Heisenberg XXZ magnet in a random field. *Physical Review B*, 77(6):064426. ix, 17, 22, 49
- [187] Zworski, M. (2012). *Semiclassical Analysis*. American Mathematical Soc.